UiT
THE ARCTIC
UNIVERSITY
OF NORWAY

Faculty of Science and Technology

Tromsø Geophysical Observatory

Trends and variability of polar mesopause region temperatures attributed to atmospheric dynamics and solar activity

—

Silje Eriksen Holmen

A dissertation for the degree of Philosophiae Doctor – October 2016

UNIVERSITY OF TROMSØ

Front page image:
Airglow and a meteor penetrating Earth's atmosphere, photographed at night over Irkutsk, Russia, from the International Space Station on 13 August 2011.
NASA Earth Observatory, http://earthobservatory.nasa.gov/IOTD/view.php?id=51754

Abstract

The mesopause region can be considered a "boundary region" between the neutral atmosphere, where atmospheric constituents and momentum are transported mainly by winds and turbulent eddies, and the ionosphere, where the main transport mechanism is molecular diffusion. In the mesopause, complex interactions between dynamics and photochemistry occur, and we are far from a complete understanding of these interactions.

This thesis aims to better understand the processes responsible for the large temperature fluctuations we observe in the polar mesopause region, especially the effects of atmospheric circulation and wave activity from lower atmospheric layers. Investigations of trends have also been conducted. To carry out these investigations, we have derived and examined mesopause temperatures from two high-latitude locations: Tromsø (70°N, 19°E) and Longyearbyen (78°N, 16°E), and turbopause height only from Tromsø. A long-term change in turbopause height may be important for understanding processes that are responsible for redistribution of atmospheric constituents.

We examined winter season variations in the hydroxyl (OH*) airglow temperature record from Longyearbyen and identified local temperature maxima in mid-January and mid-February, as well as a minimum in the transition between December and January. We also identified a number of statistically significant periodic oscillations in temperatures derived from the Nippon/Norway Tromsø Meteor Radar, with periods ranging from 9 days to a year. The seasonal variation showed higher temperatures and variability during winter compared to summer. We also found local temperature enhancements just after spring equinox and summer solstice. Temperature variability and seasonal variation may, to a large extent, be explained by the large-scale circulation in the middle atmosphere and corresponding wave activity.

The trends for the Longyearbyen OH* airglow winter temperature series and meteor radar derived temperatures from Tromsø, both annual and summer trends, were estimated to be near-zero or slightly negative. The Tromsø winter trend was negative, $(-11.6 \pm 4.1)\,\mathrm{K\,decade^{-1}}$.

We derived turbopause altitude from turbulent energy dissipation rates obtained from the Tromsø medium-frequency radar and found an increasing height in summer, $(1.6 \pm 0.3)\,\mathrm{km\,decade^{-1}}$, during the time period from 2002 until 2015, while in winter turbopause height did not change significantly. We investigated the response of the change in turbopause height to a change in

temperature, but a changing temperature did not alter trends significantly, irrespective of season.

Preface

This thesis is submitted for the degree of Philosophiae Doctor (PhD) at the University of Tromsø (UiT) - The Arctic University of Norway. The work and research described herein were conducted at the University Centre in Svalbard (UNIS) and funded through their grant from the Norwegian Ministry of Education and Research. The research in this thesis has been conducted as a part of the Birkeland Centre for Space Science (BCSS), a cooperative effort between the University of Bergen, Norwegian University of Science and Technology and UNIS.

The thesis consists of an introductory part and four papers, published in peer-reviewed journals. Below is a list of the papers, including the contributions of authors.

Paper 1
Holmen, S. E., M. E. Dyrland, and F. Sigernes (2013), Mesospheric temperatures derived from three decades of hydroxyl airglow measurements from Longyearbyen, Svalbard (78°N), *Acta Geophysica*, 62 (2), 302–315, doi: 10.2478/s11600-013-0159-4.

S.E.H. performed the data analyses and wrote the paper. M.E.D. and F.S. took part in discussions and contributed with helpful comments.

Paper 2
Holmen, S. E., M. E. Dyrland, and F. Sigernes (2014), Long-term trends and the effect of solar cycle variations on mesospheric winter temperatures over Longyearbyen, Svalbard (78°N), *Journal of Geophysical Research: Atmospheres*, 119, 6596–6608, doi: 10.1002/2013JD021195.

S.E.H. performed the data analyses and wrote most of the paper. M.E.D. and F.S. contributed with comments to the draft and wrote parts of the sections involving calibration, measurement technique and discussion regarding the height of the OH* layer and corresponding implications for temperature.

Paper 3
Hall, C. M., S. E. Holmen, C. E. Meek, A. H. Manson, and S. Nozawa (2016), Change in turbopause altitude at 52 and 70°N, *Atmospheric Chemistry and*

Physics, 16, 2299–2308, doi: 10.5194/acp-16-2299-2016.

C.M.H. did most of the data analyses and wrote the paper. S.E.H. contributed with temperature trend assessment and took part in discussions and gave feedback on the manuscript draft. C.E.M., A.H.M. and S.N. took part in discussions and gave feedback on the draft.

Paper 4
Holmen, S. E., C. M. Hall, and M. Tsutsumi (2016), Neutral atmosphere temperature change at 90 km, 70°N, 19°E, 2003–2014, *Atmospheric Chemistry and Physics*, 16, 7853–7866, doi: 10.5194/acp-16-7853-2016.

S.E.H. did the data analyses and wrote the paper. C.M.H. and M.T. took part in discussions and gave feedback on the draft.

Acknowledgements

As I write this, I am about to make the last adjustments to my thesis and finally submit it. Writing this thesis and working on mesospheric dynamics have been immensely interesting, challenging and engaging, and I can honestly say that I have appreciated every day of it.

Many people deserve to be thanked because they in different ways have contributed to the accomplishment of this thesis. First and foremost, I would like to thank my two supervisors, Professor Fred Sigernes at UNIS and Professor Chris Hall at Tromsø Geophysical Observatory, UiT. Thank you, Chris, for being supportive and encouraging and for answering my countless trivial and non-trivial questions about turbulence and radars at all hours. I have enjoyed your many emails with a mix of English, Bokmål and Northern Norwegian dialect. Thank you, Fred, for sharing your immense knowledge on optics and for giving me the freedom to pursue various projects without objection. I have enjoyed very much working with you both, and I hope I will get the opportunity to work with you in the future.

I wish to thank the co-authors of my papers. I am particularly grateful to Dr. Margit Dyrland, former Post Doc at UNIS, for her kind and valuable help and for taking the time to share her knowledge on airglow and mesopause dynamics when I was new in the research field. My sincere gratitude goes to Dr. Masaki Tsutsumi at the National Institute for Polar Research, Japan, for constructive feedback and fruitful discussions, especially regarding enhancements of ambipolar diffusion coefficients during auroral particle precipitation. I am also grateful to Dr. Chris Meek at the University of Saskatchewan for clarifying matters regarding the configuration of the medium-frequency radar.

I wish to express my appreciation to the NASA EOS Aura MLS team for providing free access to the MLS temperature data. Thank you to NASA Atmospheric Chemistry and Dynamics Laboratory for providing free access to annual meteorological statistics, and to the Solar Influences Data Center, the National Geophysical Data Center and the Active Cavity Radiometer Irradiance Monitor for providing records of measures of solar variability.

I am indebted to the journal editors and to the anonymous referees of the papers I have submitted during my PhD study. The reviewers' time and effort to provide their expert views on the manuscripts have invariably improved them a great deal. I am immensely grateful for that, even though it resulted in many additional hours of work.

I thank my fellow colleagues at the Department of Arctic Geophysics at UNIS for many stimulating and amusing discussions, both scientific and non-scientific, throughout the last four years. Lisa, Xiangcai, Eli Anne, Marius, Eva, Dag, Frank, Ragnheid, Mikko, Pål, Ylva and all the others: I will miss our coffee breaks - but I will not miss the coffee itself :). A special thank you goes to Noora Partamies for many interesting and inspiring discussions on the mysterious OH*. A big thank you to my friends in Longyearbyen, fellow PhD students and other colleagues at UNIS for making the last four years memorable and cheerful: Berit, Pernilla, Miriam, David, Julie, Anatoly, Aleksey, Gøril, Stine, Guro, Malin. A sincere thank you goes to the library services at UNIS - especially Berit Jakobsen, the best and most service-minded librarian on this planet. Thanks to Tim Dunker for his valuable feedback on this thesis. Also, I thank the people at the Birkeland Centre for Space Science, especially Patrick Espy, for answering my questions and sharing his knowledge on OH* chemistry.

Last but not least, I thank my family for their support and encouragement. Thank you, Stefan, for always being there and for believing in me. Thank you, Syver, for reminding me to strive for being the best person I can be, every day.

Silje Eriksen Holmen
October 2016

Contents

1. Introduction

1.1. Earth's atmosphere

Earth's atmosphere can be divided into different layers according to its characteristics at different altitudes. One way of classifying the atmosphere is in terms of temperature, see Figure 1.1. The *troposphere* is the lowest layer of the atmosphere, and most weather phenomena are confined within this layer. Tropospheric air is heated, or on occasion cooled, at the surface and through conduction and convection. Temperature decreases with increasing altitude as pressure decreases, following the adiabatic lapse rate. The stratosphere and mesosphere are commonly referred to as the *middle atmosphere*. The *stratosphere* extends from about 10 km (over polar regions) to about 50 km altitude, and temperature here increases with height due to the absorption of ultraviolet (UV) radiation by ozone. The region from about 50 km to about 100 km is called the *mesosphere*. Here temperature decreases with increasing altitude and follows the adiabatic lapse rate again, due to that heating by UV absorption by ozone falls off. Carbon dioxide has a cooling effect here by radiating heat into space, as opposed to further down in the atmosphere, where it acts as a greenhouse gas by absorbing infrared radiation emitted from Earth's surface. The upper-most part of the mesosphere is the *mesopause*, which is the coldest region of the atmosphere. The *thermosphere* is located directly above the mesopause and is the lowest layer of the upper atmosphere. High-energy X-rays and UV radiation from the Sun are absorbed in this layer, raising its temperature to hundreds or sometimes more than 1000 K, depending on solar activity. The mesosphere and lower thermosphere are often considered a distinct atmospheric region, commonly abbreviated the *MLT region*, because the two share some common dynamic features. Gravity waves generated in the lower atmosphere propagate upwards and break in this region, influencing the mean circulation and thermal structure of the middle atmosphere.

The atmosphere can also be divided into two layers depending on the nature of atmospheric mixing: the homosphere and the heterosphere. The *homosphere* is the part of the atmosphere below about 90 km to 100 km, depending on season, where atmospheric mixing is dominated by turbulence. The *heterosphere* is located above the homosphere. Here, molecular diffusion dominates over eddy mixing so that constituents become separated vertically according to their molecular masses. The demarcation between the two layers is called

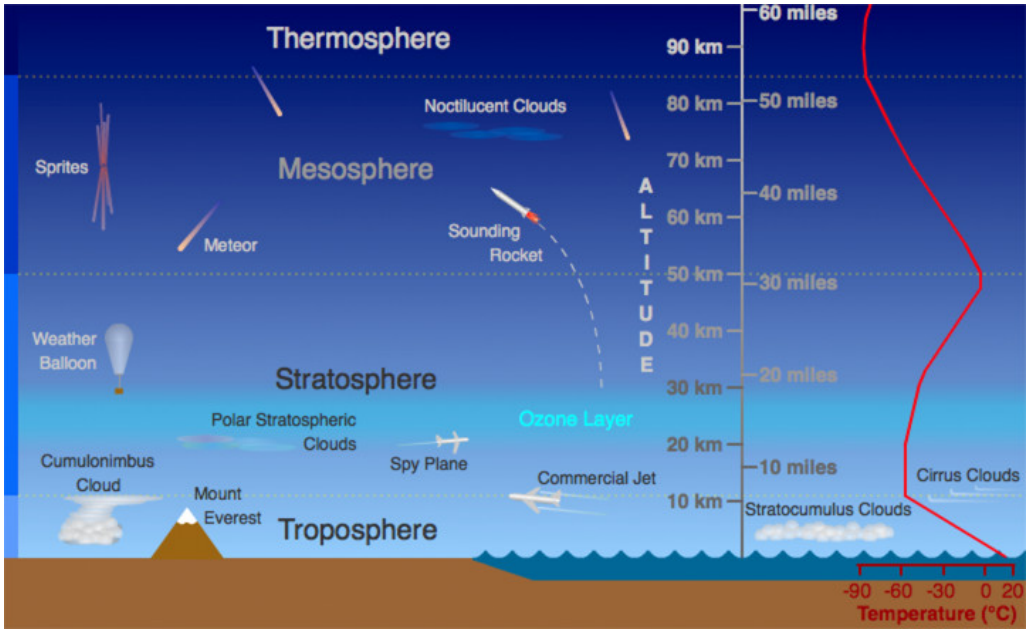

Figure 1.1.: Structure of Earth's atmosphere up to 100 km altitude. Image credit: Randy Russell, UCAR.

the *turbopause* or the *homopause*. The higher the altitude of the turbopause, the greater the downward mixing of products of photochemical processes, and the more effective the upward transport of trace gases out of the underlying regions into the upper atmosphere.

A third way of classifying the atmosphere is in terms of ionisation. The *neutral atmosphere* consists of neutral atoms and molecules, in contrast to the *ionosphere*, where gas molecules are ionised, which means that they carry an electric charge by gaining or losing electrons with the aid of high-energy solar radiation. The ionosphere is not a distinct atmospheric layer, but rather a series of regions located in parts of the mesosphere and thermosphere. The ionospheric regions are called the *D, E and F layers*, or regions, where the D layer is the lowest layer.

1.2. Why and how study the mesopause region?

The atmospheric region of interest in this thesis is the mesopause region. At first glance, one can wonder about the importance of studying the mesopause. It is located far away from where we live, and to our knowledge there are no processes going on there that are threatening human life or life quality, as opposed to ozone layer depletion in the stratosphere or hurricanes in the troposphere. Research involving the mesopause region is therefore to some extent fundamental research. However, it can be applied research as well.

The mesopause can be considered a "boundary region" between the neutral atmosphere and the ionosphere. In the neutral atmosphere, the main transport mechanism is transport by winds and turbulent eddies. In the ionosphere, the main transport mechanism is molecular diffusion, which describes fluxes of atoms and molecules from a region of higher concentration to one of lower concentration. The ionised constituents of the ionosphere are governed by physical laws that differ substantially from the laws governing neutral gases. In the mesopause region, we have complex interactions between dynamics, photochemistry and heating, and we are far from a complete understanding of these interactions.

The mesopause is one of the most poorly understood layers of the atmosphere. This is mainly because it is difficult to make direct measurements of basic atmospheric parameters like temperature and wind velocity here. Weather balloons and aircraft do not reach higher up than the stratosphere, and satellites orbit above the mesopause region and can only give indirect inferences of temperature and wind speed of this region. Sounding rockets make measurements in situ, but they are expensive and only give short, infrequent glimpses of the state of the atmosphere. The processes occurring in the mesopause are therefore not easily measured. However, some interesting phenomena occur in the mesopause, which we can utilise to derive key parameters of the region. Examples of such phenomena are airglow, polar mesospheric clouds/summer echoes and meteor ablation.

Airglow is the collective term for light emissions from excited atoms and molecules located approximately between 80 km and 100 km altitude in the atmosphere. The atoms and molecules are excited by the Sun's extreme ultraviolet (EUV) radiation and recombined to produce light emissions. From intensities of airglow emissions, we are able to determine temperatures in the mesopause region (e.g. French et al., 2000; Mies, 1974; Sigernes et al., 2003). Gravity waves and planetary waves, originating from the troposphere and stratosphere, modulate atmospheric density, temperature and composition, as well as airglow intensity. Thus, airglow emissions can be utilised for observing structures from waves propagating from the lower atmosphere, and hence for investigating atmospheric coupling (e.g. Viereck and Deehr, 1989).

The very low temperatures in the summer mesopause allow ice particles to form and grow. The largest ice particles develop into polar mesospheric clouds (PMC), which are tenuous clouds extending poleward of 50° in both hemispheres during summer. PMC are not visible from the ground poleward of 65° due to the light conditions during the Arctic and Antarctic summers (Olivero and Thomas, 1986). They require low solar elevation illumination from an observer's point of view in order to be detected. The smallest ice particles are associated with strong radar echoes, known as polar mesosphere summer echoes (PMSE). The ice particles are charged by plasma of the D

region of the ionosphere and transported by the turbulent velocity field, leading to small-scale structures in the spatial distribution of the electron number density. The resulting occurrence of irregularities in the radio refractive index is observed by radars on the ground as PMSE (Czechowsky et al., 1988; Ecklund and Balsley, 1981; Hoppe et al., 1988). PMSE give insight to key atmospheric parameters like neutral temperatures, winds, gravity waves and turbulence (Rapp and Lübken, 2004; Röttger et al., 1988). PMSE are not investigated in this PhD project.

Meteoroids frequently enter Earth's atmosphere where they are slowed down by friction with atmospheric atoms and molecules in the MLT region. The kinetic energy of a meteoroid is converted into heat, sufficient to sublime and ionise the surface of the meteoroid and to ionise the atoms and molecules of the surrounding atmosphere. The resulting plasma trail can be utilised to determine neutral temperatures and wind velocities in the region (McKinley, 1961).

In addition to the phenomena described above, we can get inferred mesospheric temperatures and wind speeds from satellite measurements. Even though satellites cannot measure temperature directly, they can measure radiance given off by atmospheric constituents, whose intensities are proportional to air temperature (e.g. Waters et al., 2006). Wind speeds can be derived using interferometry of Doppler-shifted optical spectra (Pierce and Roark, 2012).

1.3. Motivation and structure of this thesis

In the previous section, general motivation for studying the mesopause region was exhibited. The motivation for this PhD project can be divided into two main objectives. The first objective is to gain further knowledge of processes responsible for circulation and other dynamic features in the polar mesopause region, especially the effects of wave activity from lower atmospheric layers on mesopause region temperatures. Temperatures in the mesopause region are highly variable. Sometimes they can vary by 30 K to 50 K within just a few days, as can be seen in Figure 1.2. This figure shows temperatures derived from airglow over Longyearbyen in late January and early February 2012. The mechanisms behind this large variability are not completely understood. Understanding dynamical, radiative and chemical couplings between different atmospheric layers are crucial in order to assess temperature changes in the mesopause region. This thesis aims to better understand the processes responsible for the temperature fluctuations we observe.

The second objective is to investigate trends in polar mesopause region temperature and turbopause height. It has been generally accepted for decades that increasing anthropogenic emissions of greenhouse gases are responsible

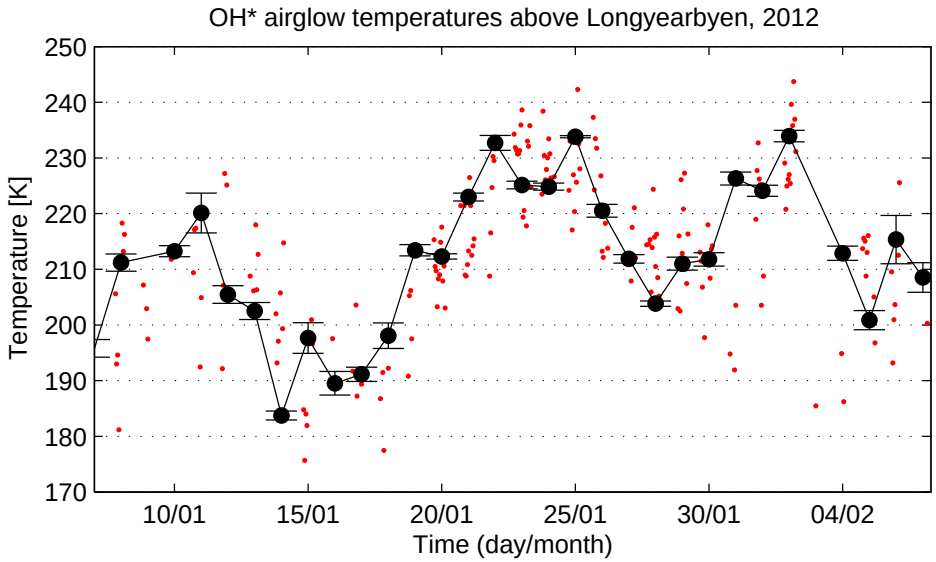

Figure 1.2.: Mesopause temperatures estimated from airglow intensities measured by the 1m Ebert-Fastie spectrometer located at the Kjell Henriksen Observatory in Longyearbyen in 2012. Red dots are hourly temperatures. Black bullets are daily averages. Error bars represent weighted uncertainties of daily temperatures.

for warming of the lower atmosphere (e.g. Manabe and Wetherald, 1975). These emissions are proposed to cause the mesosphere and thermosphere to cool (Akmaev and Fomichev, 2000; Roble and Dickinson, 1989). Akmaev and Fomichev (1998) report, using a middle atmospheric model, that if CO_2 concentrations are doubled, temperature will decrease by about 10 K in the upper mesosphere. Newer and more sophisticated models include important radiative and dynamical processes as well as interactive chemistries, and results from these models show a cooling of 3 K to 5 K in the high-latitude winter mesopause and insignificant or even a slight warming in the high-latitude summer mesopause (e.g. Fomichev et al., 2007; Schmidt et al., 2006). Observational studies on long-term trends of mesopause region temperatures from mid-latitude and high-latitude sites report slightly negative or near-zero trends (e.g. French and Klekociuk, 2011; Offermann et al., 2010). The complexity of temperature trends in the mesopause region and their causes act as motivation for studying this matter further. Investigating a long-term change in turbopause height may give insight to processes that are responsible for redistribution of atmospheric constituents.

To investigate the two main objectives of this thesis, we have utilised temperatures from two high-latitude locations, derived from hydroxyl (OH*) airglow and meteor radar, as well as estimates of turbopause height. Figure A.1 in the Appendix shows the two locations: Tromsø (70°N, 19°E) in Northern

Norway and Longyearbyen (78°N, 16°E) in the Svalbard archipelago.

The structure of this PhD thesis is as follows. Chapter 2 addresses underlying background for the results presented. In Chapter 3, theory behind hydroxyl airglow spectra and the chemistry of the hydroxyl airglow layer are described. The process of retrieving rotational temperatures from airglow intensities is also described. The theory behind retrieval of mesospheric temperatures from meteor radar, together with turbopause height derived from medium-frequency radar are treated in Chapter 4. In Chapter 5, main results are presented and discussed. Concluding remarks are given in Chapter 6, and perspectives for the future are given in Chapter 7. The papers published as a part of this PhD thesis are listed at the end.

2. Processes influencing the middle atmosphere

This chapter aims to cover background theory necessary for understanding the main results obtained in this PhD project. In Section 2.1, observed zonal winds and temperatures in the middle atmosphere are presented, together with general circulation patterns. Section 2.2 briefly describes waves responsible for driving the atmospheric circulation. Section 2.3 treats sudden stratospheric warmings, which are events that are triggered by these waves and that act as a coupling mechanism in the middle atmosphere. Section 2.4 gives a short introduction to some basic characteristics of turbulence necessary for understanding the derivation of turbopause height, which will be presented in Chapter 4. In Section 2.5, effects of solar forcing on mesopause region temperature are presented. Finally, Section 2.6 briefly describes other influences on circulation and chemistry of the middle atmosphere.

2.1. Temperature distribution and circulation

If turbulence is disregarded, the middle atmosphere would be in approximate radiative equilibrium (e.g. Fels, 1985). The temperature distribution would show a strong seasonal dependence with maximum temperature at the stratospheric summer pole and minimum at the mesospheric winter pole, see Figure 2.1. However, reality tells a different story.

Cross sections of observed zonal mean temperature in the atmosphere up to 80 km for January and July are shown in the top left and right panels of Figure 2.2, respectively. In the stratosphere, infrared radiative cooling is balanced primarily by radiative heating due to absorption of solar UV radiation by ozone. We see that mean temperature increases with height until a maximum is reached at the stratopause near 50 km. Above the stratopause, the temperature gradient gradually resumes the adiabatic lapse rate as the ozone concentration falls off with height. Minimum temperature is reached over the summer pole at the mesopause.

If we compare observed temperature with "radiatively" determined temperature for January, we see that the summer polar stratosphere is under strong radiative control, but over the winter stratosphere and mesosphere observed temperature is 60 K to 100 K higher than temperature estimated based only

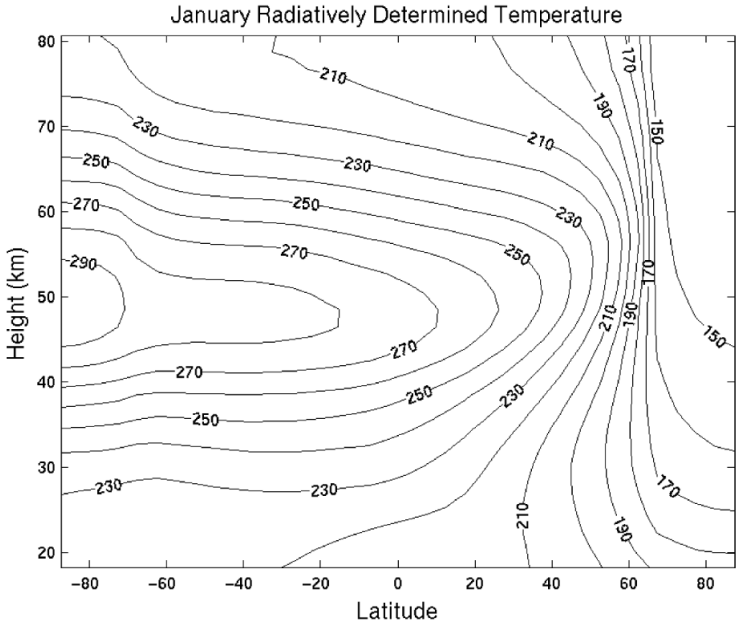

Figure 2.1.: Temperature distribution [K] in the middle atmosphere for Northern winter solstice expected for an atmosphere in radiative equilibrium. From Holton (2004), based on Shine (1987).

on radiative balance. Obviously, temperatures in the middle atmosphere are not determined by radiation alone. Dynamics and transport largely influence both the temperature distribution and the composition of the middle atmosphere (Andrews et al., 1987; Fritts and Alexander, 2003).

The two bottom panels of Figure 2.2 show cross sections of observed monthly zonal wind for January and July. The main features are a westward jet in the summer hemisphere and an eastward jet in the winter hemisphere, with maximum wind speeds reached near 60 km.

The atmosphere is a complex system which allows transport of momentum, heat, particles and compounds from one layer to another. Waves propagating from lower layers of the atmosphere and dissipating momentum into the MLT region drive the mean circulation to a large extent (e.g. Garcia and Solomon, 1985). This residual circulation is shown in Figure 2.3 and is characterised by rising motions above 30 km in the summer hemisphere, with flow from the summer to the winter hemisphere in the upper stratosphere and mesosphere, and descent in the winter hemisphere (Dunkerton, 1978; Murgatroyd and Singleton, 1961). Downwelling of air over the winter pole causes the air to be compressed and adiabatically heated. Conversely, upwelling at the summer pole causes air to expand, leading to a cooling of the summer mesopause. Therefore, the summer mesopause is cooler than the winter mesopause. The lower stratospheric part of the circulation is called the Brewer-Dobson cir-

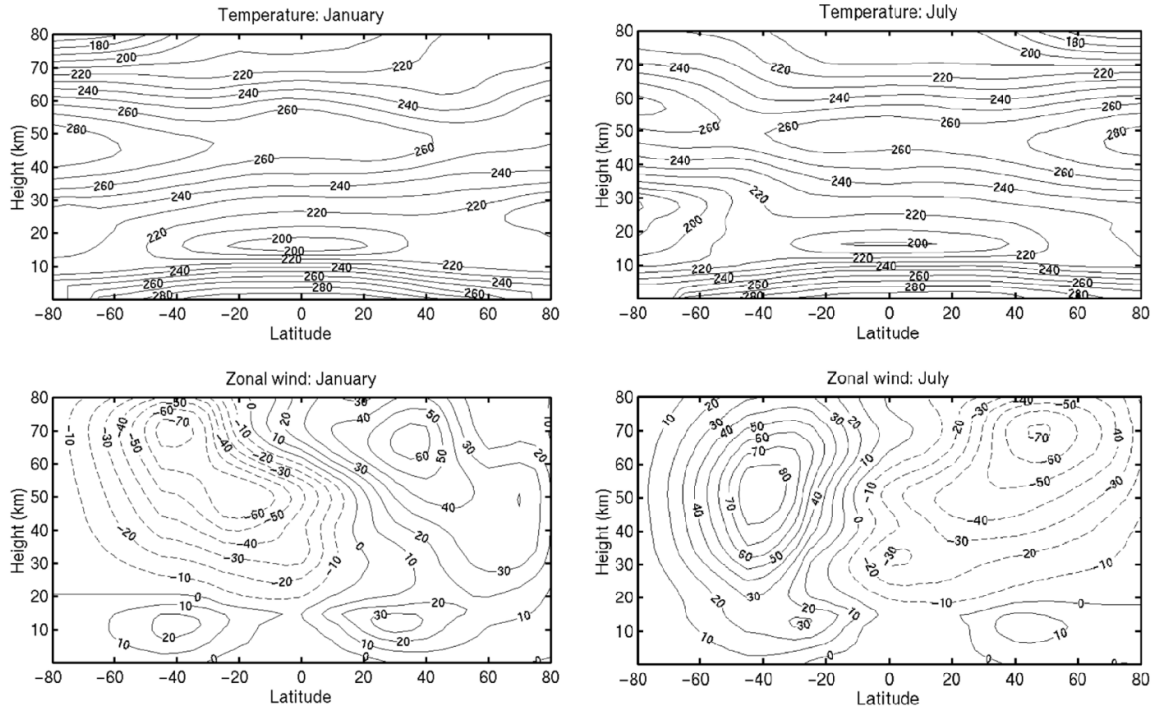

Figure 2.2.: Observed monthly and averaged temperature [K] and zonal wind [m/s] for January (left) and July (right). Negative wind speeds (dotted contours) represent westward (easterly, from east) winds, while positive wind speeds (solid line contours) represent eastward (westerly, from west) winds. From Holton (2004), based on Fleming et al. (1990).

culation and consists of rising motions at low latitudes and descent at high latitudes, approximately symmetric about the equator (Brewer, 1949; Dobson, 1956).

2.2. Planetary waves and gravity waves

Two groups of waves largely responsible for driving the atmospheric circulation are gravity waves (GWs) and planetary waves (PWs). GWs are created in the troposphere, e.g. by thunderstorm updrafts, Kelvin-Helmholtz instability around the jet stream or when winds flow over mountains (orographic forcing). Their restoring force is buoyancy. They can propagate vertically and horizontally, and both eastwards and westwards, but only against the zonal flow, or if they have higher phase speeds than the background flow. During westward zonal flow, westward-propagating GWs are filtered out at a so-called critical layer and vice versa. A critical layer is reached where the phase velocity of the wave is equal to the mean fluid velocity, and momentum

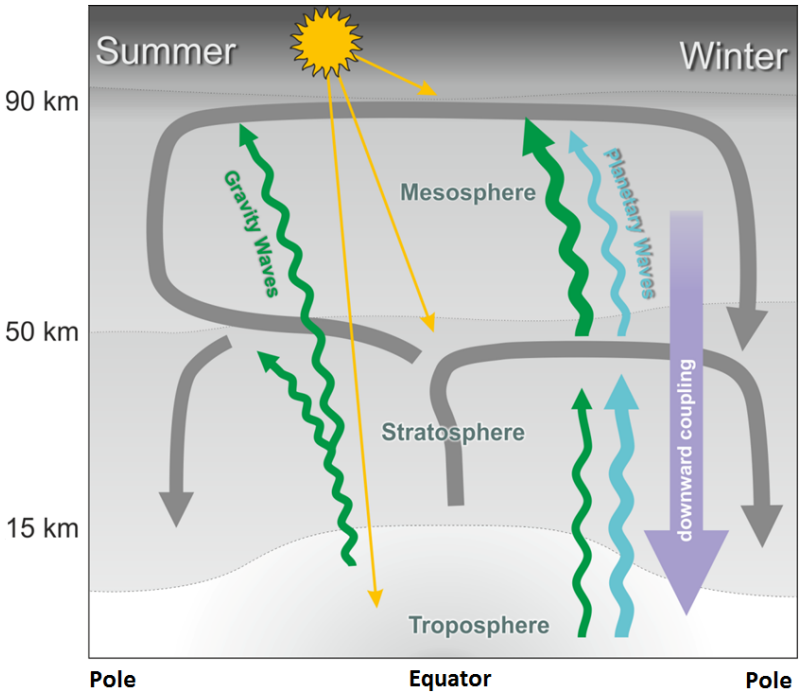

Figure 2.3.: Schematic representation of the residual circulation of the middle atmosphere. The stratospheric part of the circulation is called the Brewer-Dobson circulation. The mesospheric part is commonly referred to as the mesospheric residual circulation. Image credit: Jülich Forschungszentrum.

is transferred to the mean flow (Booker and Bretherton, 1967). During winter, when the mean stratospheric zonal flow is eastward, only GWs with westward phase speeds can propagate vertically. During equinox, stratospheric winds reverse, and the dominant direction of GWs in the mesosphere also reverses. During summer, the mean stratospheric zonal flow is westward, and therefore only GWs with eastward phase speeds can propagate vertically.

GWs in the upper mesosphere typically have vertical wavelengths ranging from 2 km to 30 km, periods of a few minutes to a few hours and horizontal phase speeds of up to $80\,\mathrm{m\,s^{-1}}$ (Andrews et al., 1987; Fritts, 1984; Hines, 1960).

Planetary waves, or Rossby waves, are caused by meridional perturbations of the zonal flow (Rossby, 1939). The waves with the largest amplitudes arise when the atmosphere in motion encounters changing surfaces, e.g. large-scale orography or land-sea contrasts, and is forced to ascend, due to a changing surface topography, and descend, due to gravity. Their restoring force is provided by the latitudinal gradient of the planetary vorticity caused by Earth's rotation. Potential vorticity must be conserved, resulting in that air that is forced to ascend tends to turn to the left, and as it descends again it turns to

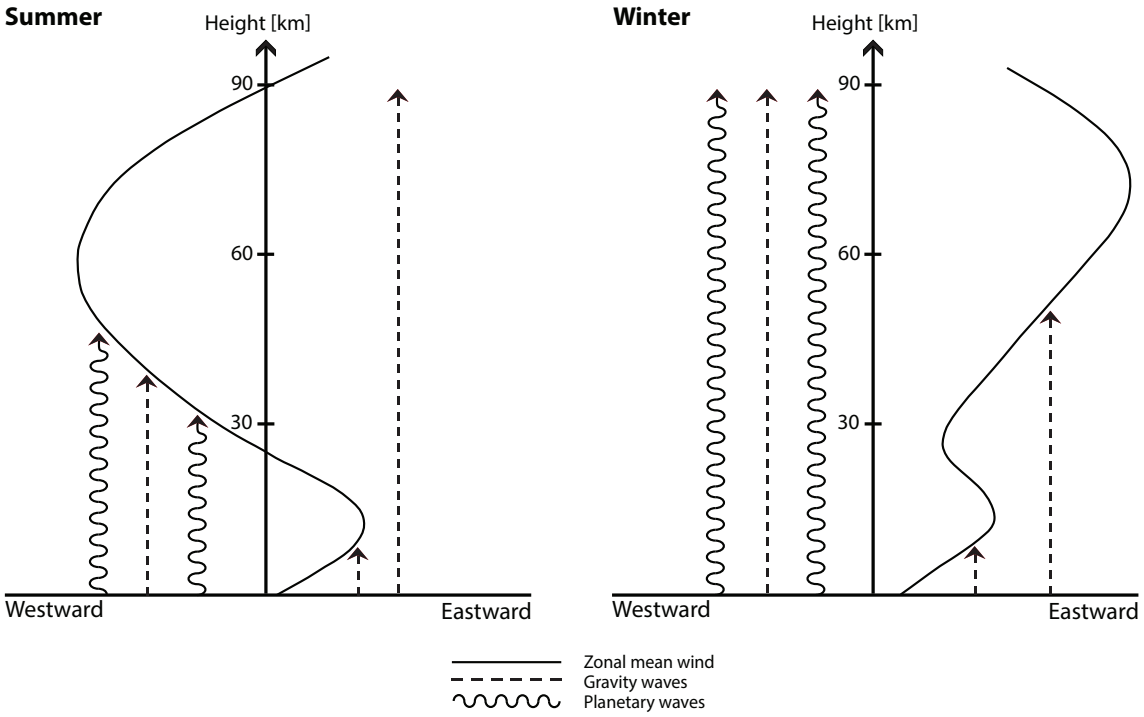

Figure 2.4.: Propagation of gravity waves and planetary waves during Northern Hemisphere summer (left) and winter (right).

the right (Dickinson, 1978).

PWs can only propagate westwards. If the zonal wind is eastward, they propagate upwards into the middle atmosphere with a velocity smaller than a critical value, which is a function of the horizontal wavenumber. This criterion is called the Charney-Drazin criterion (Charney and Drazin, 1961). PWs in the middle atmosphere have typical periods of 2 days to 16 days (Dunkerton, 1991; Salby, 1981a,b) and are assigned zonal wave numbers referring to the number of wave cycles along a given latitude circle.

PWs are most abundant in the Northern Hemisphere winter. The summer stratosphere has a mean westward zonal flow, and PWs cannot propagate during these conditions. The zonal distribution of water and land masses in the Northern Hemisphere are favourable for PW formation. PWs are also produced in the Southern Hemisphere, but they are much weaker, due to fewer mountain ridges and more open water (Shiotani and Hirota, 1985). Figure 2.4 shows the propagation of GWs and PWs during Northern Hemisphere winter and summer.

Amplitudes of both PWs and GWs increase as atmospheric density decreases with height. Eventually, waves break when their amplitudes grow large enough, depositing momentum and heat in the stratosphere and mesosphere (Eliassen and Palm, 1961). Vertically propagating GWs drive the residual circulation in the mesosphere by carrying eastward momentum and impos-

ing a drag that gives an equatorward meridional flow in summer. In winter, GWs carry westward momentum and impose a drag that gives a poleward meridional flow. PWs drive the circulation in the stratosphere by inducing a westward drag on the zonal flow and thus contributing to a meridional flow towards higher latitudes during wintertime: the Brewer-Dobson circulation (Holton, 2004). PWs are also driving forces behind sudden stratospheric warming events.

2.3. Sudden stratospheric warmings

The lack of heating in the polar stratospheric winter, due to little absorption of solar radiation by ozone, leads to the formation of the polar vortex, a core of cold air located above the winter pole, characterised by strong eastward zonal winds. In contrast, during summer, continuous heating of the polar stratosphere takes place, leading to a weaker temperature gradient between the equator and the pole and thus a weakening of the polar vortex (Schoeberl and Hartmann, 1991).

A sudden stratospheric warming (SSW) is the most dramatic event in the winter polar stratosphere. During an SSW, the polar vortex, stretching from the middle troposphere to the stratosphere, undergoes a strong temperature increase, in some cases as much as 50 K to 70 K in just a few days. The vortex is either disturbed and displaced from its typical location or split into two vortices, resulting in that the eastward zonal winds are slowed down or even completely reversed (Labitzke and Naujokat, 2000). According to the World Meteorological Organisation, an SSW is defined as *major* if at 10 hPa or lower altitudes the latitudinal mean temperature increases abruptly poleward from 60° latitude and the eastward zonal-mean winds reverse. If the temperature gradient is reversed, but not the circulation, the SSW is classified as *minor*. The Arctic polar vortex is less stable than the Antarctic because of the distribution of water and land masses, so SSWs are much more common in the Northern Hemisphere. In the Southern Hemisphere, only one major SSW event has ever been observed. This occurred in September 2002 (Dowdy et al., 2004).

PWs are driving forces behind SSW events, where they, by interacting with the mean zonal flow, have the power to weaken and disturb the polar vortex. The development of an SSW starts with the growth of planetary-scale disturbances (zonal wavenumbers 1 and 2) in the troposphere until they reach a large amplitude. PWs propagate into the stratosphere and give rise to a deceleration of the eastward jets and a weakening of the polar vortex. Zonal mean temperatures at high latitudes increase due to the waves. The westward acceleration of the zonal wind increases with increasing height, and at a certain level the winds reverse to westward. This level is called the critical

layer. PWs are absorbed at the critical layer and prevented from propagating further upwards. An intense warming of the polar cap region just below the critical layer is observed, due to Eliassen-Palm flux divergence of forced, upward-propagating PWs, and the westward winds are accelerated, lowering the level of warming and wind reversal (Matsuno, 1971).

SSWs not only impact the stratosphere. Mesospheric cooling and wind reversal are observed during SSW onset (e.g. Hoffmann et al., 2007; Labitzke, 1981). Observations show a downward propagation of circulation disturbances with an earlier onset of zonal wind reversal in the mesosphere compared with the upper stratosphere (Hoffmann et al., 2007). Proposed coupling mechanisms between the stratosphere and mesosphere during SSW events are related to PW and GW activity. Observations show evidence of increased wave number 1 PW and reduced GW activity in the mesosphere during SSW events. The mesospheric cooling is caused primarily by a relaxation of the polar mesosphere towards radiative equilibrium. This occurs as the westward winds induced by the SSW reduce transmission of GWs into the mesosphere (Holton, 1983).

2.4. Turbulence and the turbopause concept

Atmospheric turbulence is small-scale, irregular air motions due to winds that vary in speed and direction. Turbulence provides mixing of constituents, heat and energy in the atmosphere. The main sources are probably GWs and tides, which generate turbulence through non-linear breaking, shear instabilities, convective overturning and critical-level interaction (Hodges, 1967; Lindzen, 1981).

Two essential characteristics of turbulence are turbulent diffusion and turbulent energy dissipation. *Turbulent diffusion* is the transport or spreading of heat, momentum and tracer concentration due to irregular velocity fluctuations. *Turbulent energy dissipation* prevents an unlimited growth of turbulence. It is characterised by turbulent energy being cascaded successively to smaller and smaller eddies. At a very small scale, called the Kolmogorov microscale, the eddies are depleted, or dissipated, by viscous forces in the smallest eddies, and ultimately the energy is converted into heat (Kolmogorov, 1941; Reynolds, 1987). See Figure 2.5 for an illustration.

Atmospheric turbulence is important up to an upper altitude region ranging from 95 km to 110 km, varying on both a daily and a seasonal basis, where viscosity becomes so large that it damps any tendency for turbulence to form. This transition region is referred to as the turbopause (Hocking, 1987).

The turbopause may be defined in several ways, depending on measurement technique (Lehmacher et al., 2011). Blamont (1963) described a sudden transition from turbulent to laminar shapes becoming visible in sodium clouds

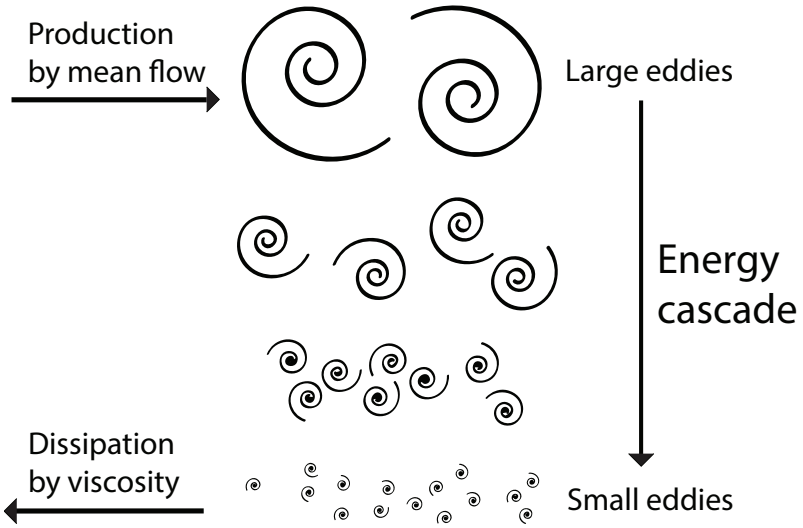

Figure 2.5.: Turbulent energy cascade.

ejected from rockets at an altitude varying between 95 km and 105 km. This can be referred to as the *visual turbopause*. Offermann et al. (2007) suggested the concept of a *wave turbopause*, which is based on the vertical distribution of wave dissipation and derived from standard deviations of vertical profiles of temperature variances. The turbopause may also be defined as the altitude where the eddy diffusion coefficient is equal to the molecular diffusion coefficient. It may be derived from mixing ratio profiles of particular species (Danilov et al., 1979) and is referred to as the *mixing turbopause*. In *Paper 3*, we have utilised the concept of the mixing turbopause and estimated the turbopause level by estimating turbulent energy dissipation rates using medium-frequency radar.

The turbopause may be defined in terms of the Reynolds number, Re, which is defined as the ratio of inertial forces to viscous forces in a fluid flow:

$$Re = \frac{\rho v L}{\mu} = \frac{v L}{\nu} \tag{2.1}$$

where ρ is the density of the fluid, v is mean velocity, L is characteristic length, μ is dynamic viscosity of the fluid and ν is kinematic viscosity (Reynolds, 1894).

The Reynolds number is dimensionless. If Re is large, we have turbulent flow. Contrary, if Re is small, we have laminar flow. Depending on the type of fluid, flow speed and the diameter of the flow, $Re < \sim 2300$ gives a laminar flow (Warhaft, 1997). At the turbopause, turbulent and molecular diffusivities are equal, and Re is unity.

2.5. Solar forcing

The atmosphere is not only affected internally through dynamics, but also by external forcing from above. The variability in the incoming solar shortwave radiation is known to drive changes in the atmosphere on decadal, annual and seasonal scales. The F10.7 cm solar radio flux, measured daily at the Penticton Radio Observatory in British Columbia, Canada, is one commonly used indicator of solar activity and correlates well with the sunspot number, as well as with a number of ultraviolet and visible solar irradiance records. During solar maximum, stronger dissociation of molecular oxygen by Lyman-α radiation takes place, leading to enhanced production of atomic oxygen. Lyman-α is a spectral line of hydrogen, emitted from the full solar disc with an integrated flux equivalent to the total solar emission at all wavelengths less than 150 nm, and thus it is a measure of solar activity (Lean and Skumanich, 1983). Airglow intensity is directly proportional to atomic oxygen concentration and hence correlated with the 11-year solar cycle (Grygalashvyly, 2015). Further details on the chemistry of the airglow layer will be given in Section 3.2.

It has been proposed that mesopause region airglow temperatures respond to solar activity also on shorter time scales. Solar flares and coronal mass ejections on the Sun may lead to energetic particles penetrating the atmosphere all the way down to the upper stratosphere. During solar proton events, high energy protons ionise molecules in the atmosphere, altering concentrations of odd hydrogen, nitrogen and oxygen, which again may deplete ozone in the mesosphere (e.g. Beig et al., 2008; Thomas et al., 1983). Since OH* airglow intensity and concentration in the mesopause are related to ozone concentration, which we will see in Section 3.2, mesopause region airglow may be influenced by short-term variations of solar activity. Scheer and Reisin (2007) investigated this for airglow temperatures mostly from El Leoncito (31.8°S), but they did not find signatures in their data that could convincingly be related to geomagnetic storms. The influence of solar activity on mesopause region temperatures on short time scales is not discussed in this PhD thesis.

2.6. Other influences on circulation and chemistry

The quasi-biennial oscillation (QBO) is a system where zonally symmetric eastward and westward wind regimes in the tropical stratosphere alternate regularly with a period varying from about 24 months to 30 months. Successive regimes propagate downwards from about 30 km at an average rate of 1 km month^{-1} (Lindzen and Holton, 1968). The QBO also influences the

circulation in the polar middle atmosphere (Holton and Tan, 1980). As an example is the frequency of SSWs affected by the phase of the QBO, where the westward phase is more associated with SSWs (Labitzke and Naujokat, 2000). The QBO is driven by vertically-propagating GWs, which are weakened by infrared cooling. Their momentum flux is deposited into the mean flow, leading to an oscillation in the mean flow (Holton and Lindzen, 1972).

Atmospheric tides are daily global-scale oscillations that can cause temperature amplitudes of more than 10 K in the mesosphere. Tides are primarily forced by diurnal variations of the heating due to absorption of solar UV radiation by H_2O and O_3 (Andrews et al., 1987).

In this PhD work, mesopause temperature is mainly evaluated on time scales of months or years. Therefore, atmospheric tides on short time scales are not discussed.

3. Hydroxyl (OH*) airglow

Airglow is the emission of light by atoms and molecules excited through chemical processes and collisions in the middle and upper atmosphere. The emissions are produced when UV light from the Sun dissociates molecular oxygen into individual atoms during daytime (or periods of midnight sun). Atomic oxygen cannot efficiently recombine. Hence, its lifetime in the mesopause region is very long (∼months), providing a "storage" of the chemical energy that powers the airglow during night time (or polar night). Different chemical reaction chains, involving atomic oxygen from the photodissociation of molecular oxygen, are responsible for the production of the excited states of atmospheric species. The excited atoms and molecules cascade to lower energy states by emitting light (photons), resulting in an emission spectrum over a wide wavelength range, from both the ultraviolet, visible and infrared part of the electromagnetic spectrum. The greatest contributions of airglow emissions are from the infrared. These are the brightest emissions in the night sky by far, but are beyond the visible spectrum range that we can see.

Excited atomic oxygen provides green (5577 Å) and red (6300 Å/6364 Å) emissions at 90 km to 100 km altitude and 150 km to 300 km altitude, respectively. Sodium atoms provide yellow light (∼5890 Å) at a layer centred at ∼91 km. Excited molecular oxygen emits blue and near ultraviolet multi-wavelength banded radiation (3100 Å to 5000 Å) at ∼95 km height. Vibrationally and rotationally excited hydroxyl emits visible to infrared radiation at a layer centred at 87 km, where the near-infrared lines are the brightest (Chamberlain, 1961). Figure 3.1 shows layers of airglow enveloping Earth, observed from space.

Airglow can be divided into three groups depending on when it is observed, and the exact processes behind the three vary slightly. Airglow observed at night is called *nightglow*. During the day and at twilight it is referred to as *dayglow* and *twilightglow*, respectively. In this thesis, we have investigated nightglow data and are thus referring to nightglow when we use the term "airglow".

Airglow emissions are useful indicators of dynamical and chemical processes in the mesopause region. From airglow intensities, we can obtain temperatures of the mesopause region. This chapter elaborates on how this is possible, using emissions from the excited hydroxyl (OH*) molecule. Section 3.1.1 gives a short introduction to spectra of diatomic molecules, while Section 3.1.2 treats

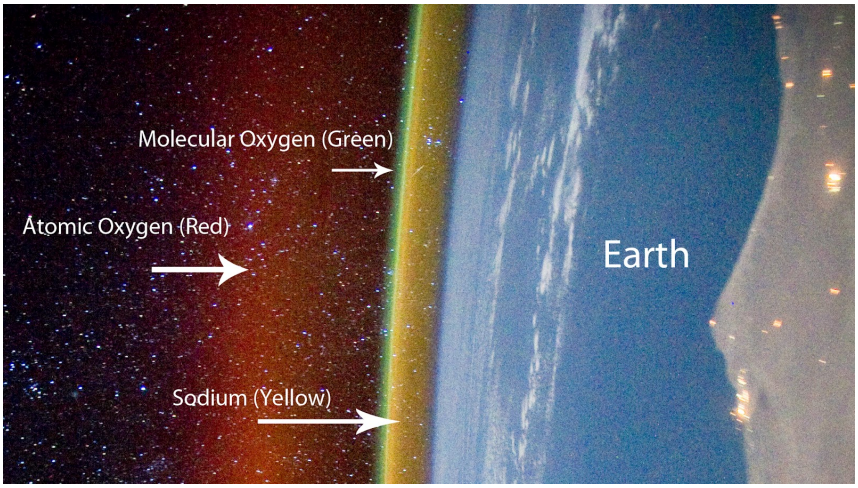

Figure 3.1.: Airglow layers created by light-emitting atoms and molecules in the middle and upper atmosphere. Image credit: NASA, with annotations by Alex Rivest.

OH* spectra in particular. Section 3.2 deals with the chemistry of OH* in the mesopause region. The method used for the retrieval of temperatures from the OH*(6-2) vibrational band is presented in Section 3.3. Finally, the instrumentation and data analysis are described in Section 3.4.

3.1. Molecular structure and spectra

3.1.1. Diatomic molecules

The theory behind the formation of emission spectra of diatomic molecules, which are molecules with two atoms, is described in detail in Herzberg (1950) and will briefly be repeated here. The total energy of a diatomic molecule is the sum of the electronic, vibrational and rotational energies:

$$E_{tot} = E_e + E_v + E_r \tag{3.1}$$

An atom or a molecule can only exist in energy states with certain discrete values.

A molecule can be in different *electronic states*, depending on the orbitals in which its electrons are. The state where all electrons have their lowest possible energies is referred to as the *ground state*. The electronic states of molecules are labelled and identified by their angular momentum and symmetry properties. The ground state is denoted X, while the excited states are denoted A, B, C, ...

A molecule's electrons have *orbital angular momentum*, $\mathbf{L}$, associated with their orbit motion, and *spin angular momentum*, $\mathbf{S}$, associated with the rota-

tion about their own axes. The total electronic angular momentum, $\mathbf{\Omega}$, is the vector sum of the two. In a diatomic molecule, the symmetry of the field in which the electrons move is reduced. There is only axial symmetry about the internuclear axis. The component of $\mathbf{L}$ along the internuclear axis is denoted Λ, and the constant component of the precession of $\mathbf{S}$ is denoted Σ. The total electronic angular momentum about the internuclear axis is defined as:

$$\Omega = \mid \Lambda + \Sigma \mid \tag{3.2}$$

Λ takes on discrete, positive values $0, 1, 2, ..., L$. The corresponding molecular state is represented by Greek letters Σ, Π, Δ, ... respectively, and is preceded by a symbol referring to the electronic state; *X*, *A*, *B*... See Eq. 3.8 for an example. Σ takes on values $S, S-1, S-2, ..., -S$, where S is non-negative integers or half integers, depending on whether the total number of electrons in the molecule is even or odd, respectively. Thus, Σ can, in contrast to Λ, be positive and negative and either integer or half integer.

Different values of $\Lambda + \Sigma$ correspond to different energies of the resulting molecular state. If $\Lambda \neq 0$ (that is, for Π, Δ, ... states), the electronic energy level splits into a so-called *multiplet* of $2S+1$ components. Molecules with an even number of electrons have odd multiplicities (singlets, triplets, ...), since S is integer. Conversely, molecules with an odd number of electrons have even multiplicities (doublets, quartets, ...), since S is half integer.

The electronic energy of the state, E_e, is given by the minimum value of the potential energy function of a given stable electronic state

$$E^{el} + V_n \tag{3.3}$$

where E^{el} is the electronic energy of the nuclei and V_n is the Coloumb potential, which is dependent on the nuclear charges and internuclear distance.

A diatomic molecule has two modes for motion. It can *rotate* about an axis passing through the centre of gravity, perpendicular to the line joining the nuclei. Also, the two atoms can *vibrate* relative to each other along the internuclear axis.

The simplest assumption of vibrational motion is that the diatomic molecule is a harmonic oscillator. This means that each atom moves towards or away from the other in simple harmonic motion. The displacement from equilibrium is a sine function of time. The vibrational energy of the harmonic oscillator is:

$$E_v = h\nu_{osc}\left(v + \frac{1}{2}\right) \qquad v = 0, 1, 2, ... \tag{3.4}$$

where h is Planck's constant and ν_{osc} is the vibrational frequency of the oscillator. v is the *vibrational quantum number*, which can take only values $\in \mathbb{N}_0$.

v describes vibrational energy levels, or energy states, of a molecule. Upper and lower vibrational quantum levels are denoted v' and v'', respectively. The energy for the harmonic oscillator is not zero in the state of lowest energy. Even in the lowest vibrational state, vibrational energy is present.

The simplest model of a rotating molecule is the so-called dumbbell model, where we consider two point masses, m_1 and m_2, fastened at a fixed distance r apart. The two masses rotate around the centre of gravity with a rotational frequency. The rotational energy of such a system is given by:

$$E_r = \frac{h^2 J(J+1)}{8\pi^2 I} \qquad J = 0, 1, 2, ... \tag{3.5}$$

where I is the moment of inertia of the system and J is the *rotational quantum number*, which can take only values $\in \mathbb{N}_0$. J represents rotational angular momentum, and in the absence of external electric or magnetic fields, the energy level depends only on the molecule's change in angular momentum. Thus, we have a series of discrete energy levels whose energy increases quadratically with increasing J.

A diatomic molecule can undergo transitions from one rotational energy level to another through absorption or emission of a photon. This results in spectral lines which can be detected by a spectrometer. J' and J'' denote the upper and lower rotational quantum levels, respectively, and ΔJ is the difference between them. Not all rotational transitions are allowed. Quantum mechanical selection rules determine that:

$$\Delta J = J' - J'' = \begin{cases} -1 \\ 0 \\ 1 \end{cases} \tag{3.6}$$

Different variations of ΔJ correspond to different *branches of lines*. $\Delta J = -1$ corresponds to the so-called P branch of the lines, $\Delta J = 0$ corresponds to the Q branch, and $\Delta J = 1$ corresponds to the R branch.

The above descriptions of simple models for rotating and vibrating diatomic molecules are idealised and represent observed spectra to a good approximation. However, sometimes large deviations from these idealised models are observed, due to that rotation, vibration and electronic motion take place simultaneously, and that these motions influence each other. This matter will not be further elaborated on here.

The emission wavelength, λ, of a diatomic molecule is determined by the energy difference of a transition between an upper and a lower molecular state:

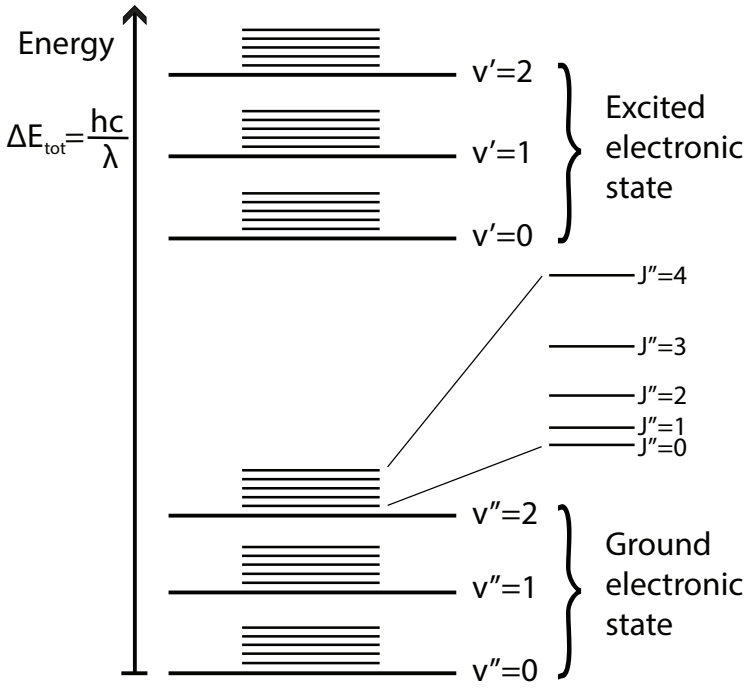

Figure 3.2.: Schematic of energy levels of a diatomic molecule. The electronic energy levels are widely separated compared to the vibrational levels. The rotational levels are even more closely situated than the vibratonal levels. For legibility, only the lowest levels are presented. Figure is not drawn to scale.

$$\begin{aligned}\lambda &= hc/(E_{v'} - E_{v''} + E_{J'} - E_{J''}) \\ &= (G(v') - G(v'') + F(v', J') - F(v'', J''))^{-1}\end{aligned} \tag{3.7}$$

where c is the speed of light and E is energy of the states. *G(v)* is the vibrational term in vibrational state v and *F(v,J)* is the rotational term in vibrational state v and rotational state *J*. ' and " denote upper and lower states, respectively.

Electronic energy is by far the largest contributor to the total energy. The vibrational energy states give a fine structure to the electronic states, while the rotational energy states give a fine structure to the vibrational states, see Figure 3.2.

The upper and lower states can differ in electronic, vibrational and rotational states. Molecules undergoing transitions from a higher vibrational and rotational state to a lower state results in the formation of *molecular spectra* composed of *vibrational bands*, which again consist of *rotational lines*. Figure 3.4 shows the nightsky spectrum between 1200 Å and 9000 Å.

3.1.2. OH*

In this PhD thesis, we denote the hydroxyl emissions *OH** to emphasise that we refer to the vibrationally and rotationally excited hydroxyl airglow. OH* airglow emission bands were first described in detail by Meinel (1950a,b). OH* in the mesopause is in its electronic ground state designated by

$$X^2\Pi_{\frac{3}{2}} \quad and \quad X^2\Pi_{\frac{1}{2}} \tag{3.8}$$

The splitting into two states is due to that OH* is in a doublet state, and this is annotated by the left superscript to Π (the number 2). The annotation Π corresponds to that Λ equals 1. The right subscripts to Π, $\frac{3}{2}$ and $\frac{1}{2}$, correspond to total electronic angular momentum, Ω, and from Eq. 3.2 it follows that Σ can be either $-\frac{1}{2}$ or $+\frac{1}{2}$. This is due to that the electron spin can be either up or down, which is an effect of the odd number of electrons, as described in the previous section.

The $X^2\Pi_{\frac{3}{2}}$ state gives rise to the so-called P_1, Q_1 and R_1 branches, while the $X^2\Pi_{\frac{1}{2}}$ state gives rise to P_2, Q_2 and R_2. The $X^2\Pi_{\frac{1}{2}}$ state lies higher than the $X^2\Pi_{\frac{3}{2}}$ state, which makes the P_2, Q_2 and R_2 line intensities weaker than P_1, Q_1 and R_1 in the lower, more populated state. Consequently, there is an alternation in intensity between P_1 and P_2 lines.

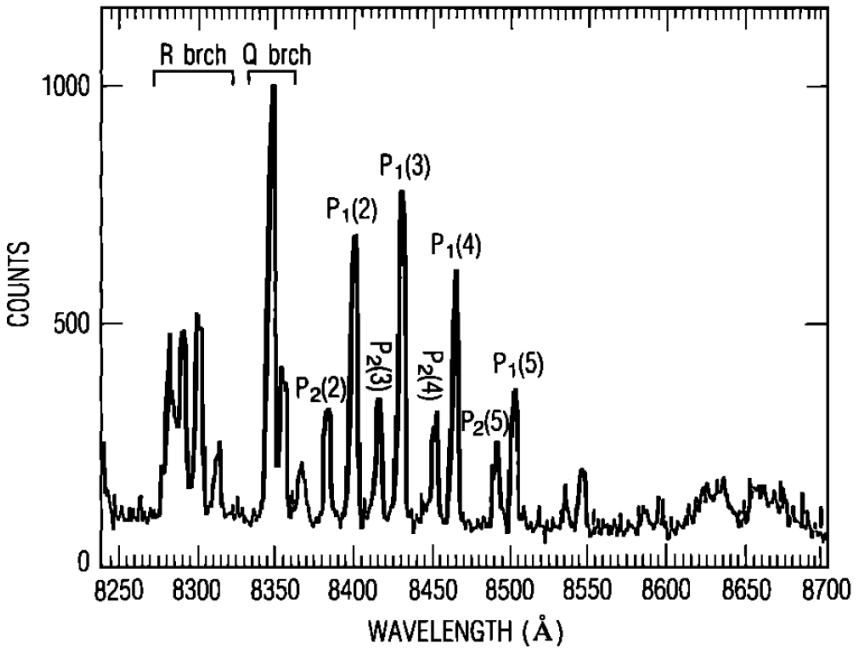

Figure 3.3.: Spectrum of the OH*(6-2) vibrational band, averaged over a half-hour period, recorded with a $\frac{1}{2}$ m Ebert-Fastie spectrometer in Longyearbyen. From Sivjee and Hamwey (1987).

In this PhD project, we have used spectra from the OH*(6-2) vibrational band to calculate rotational temperatures, meaning the OH* band with the transition from $v' = 6$ to $v'' = 2$. The emission wavelengths of OH*(6-2) are $\sim$8400 Å. Figure 3.3 shows the P, Q and R branches of OH*(6-2).

According to Eq. 3.7 in the previous section, the emission wavelength of a diatomic molecule can be determined if the energies of the upper and lower molecular states are known. The energy levels can be deduced if the vibrational and rotational terms are known. The vibrational term for OH*(6-2) is:

$$G(v) = \omega_e\left(v+\frac{1}{2}\right) - \omega_e x_e\left(v+\frac{1}{2}\right)^2 + \omega_e y_e\left(v+\frac{1}{2}\right)^3 - \omega_e z_e\left(v+\frac{1}{2}\right)^4 + ... \quad (3.9)$$

where ω_e, $\omega_e x_e$, ... are vibrational constants taken from Chamberlain and Roesler (1955) and listed in Table 3.1.

The two rotational terms of OH*(6-2), corresponding to the two states $X^2\Pi_{\frac{3}{2}}$ and $X^2\Pi_{\frac{1}{2}}$, are determined by the formulae of Hill and Van Vleck (1928):

$$F_1(v,J) = B_v\left[\left(J+\frac{1}{2}\right)^2 - 1 + \frac{1}{2}\sqrt{4\left(J+\frac{1}{2}\right)^2 + Y_v\left(Y_v-4\right)}\right] - D_v J^4 \quad (3.10)$$

$$F_2(v,J) = B_v\left[\left(J+\frac{1}{2}\right)^2 - 1 - \frac{1}{2}\sqrt{4\left(J+\frac{1}{2}\right)^2 + Y_v\left(Y_v-4\right)}\right] - D_v J^4 \quad (3.11)$$

where B_v, D_v and Y_v are rotational constants calculated by Krassovsky et al. (1962) and listed in Table 3.1. Figure 3.5 shows vibrational structure, as well as rotational structure of vibrational levels of the OH* $X^2\Pi$ ground state.

3.2. Chemistry of the OH* layer

3.2.1. Production and loss of OH* in the polar mesopause region

Excited hydroxyl in the polar mesopause region is produced mainly by these reactions:

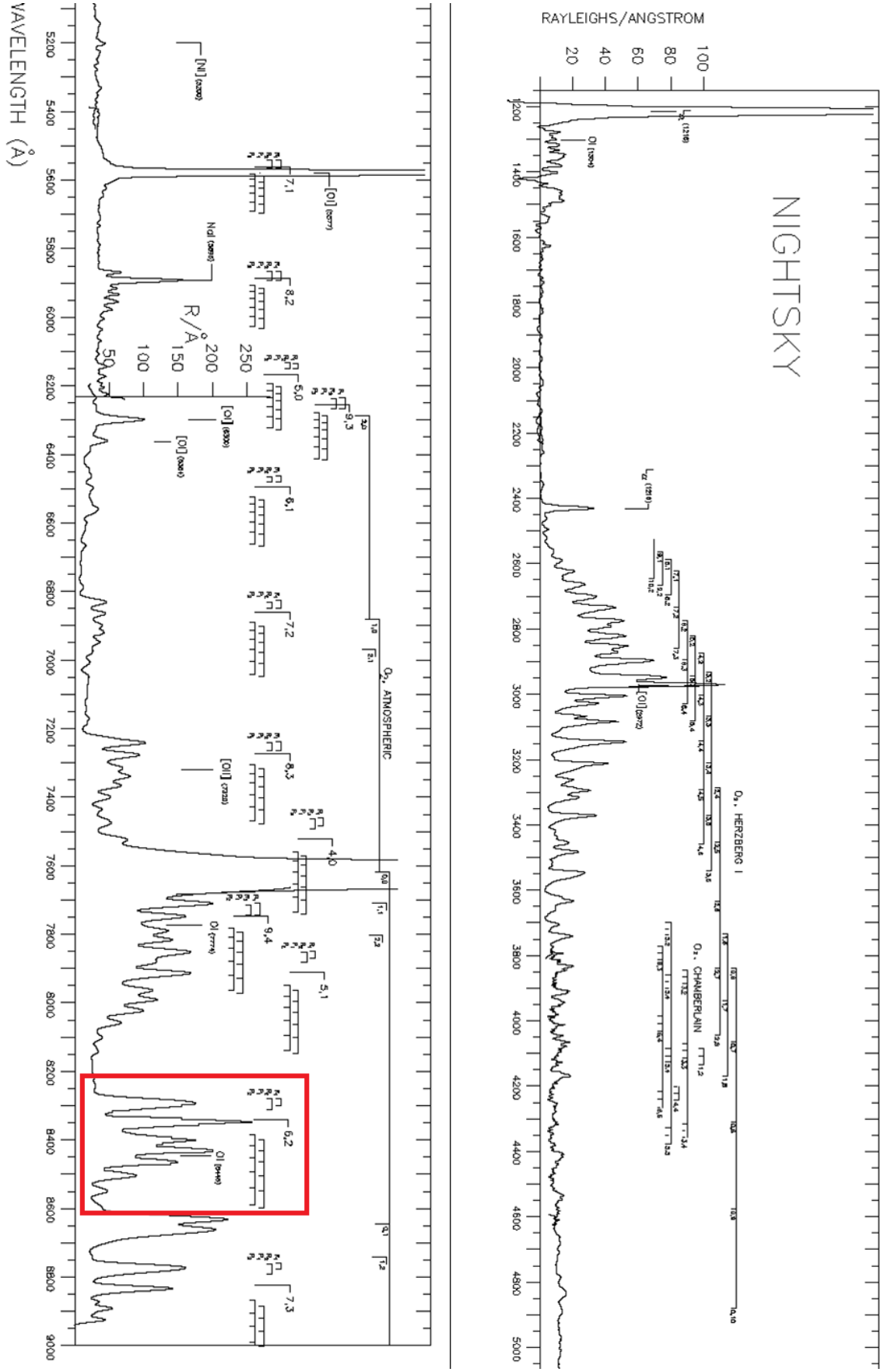

Figure 3.4.: Nightsky spectrum between 1200 Å and 9000 Å, recorded in December 1992 by Ultraviolet Spectroscopy and Imaging Group, University of Arizona. The OH*(6-2) vibrational band is highlighted.

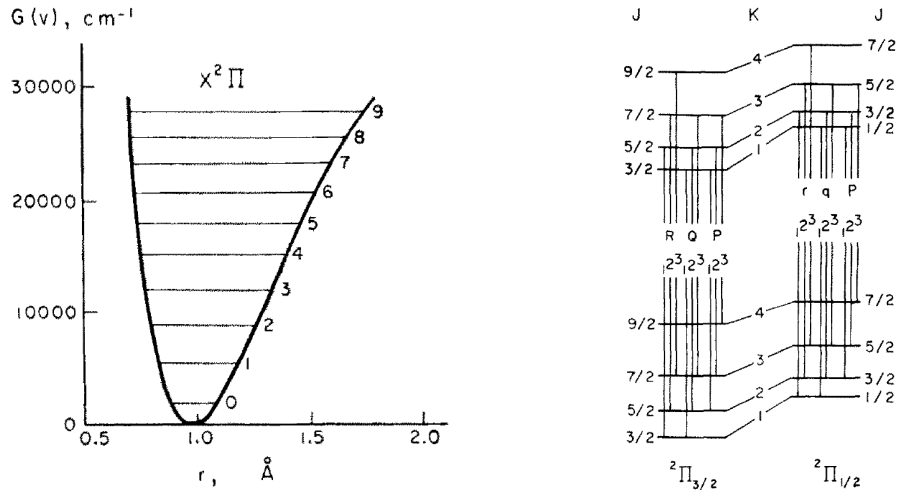

a) b)

Figure 3.5.: a) Potential curve of the OH* $X^2\Pi$ ground state, showing vibrational structure. b) Rotational structure of vibrational levels. From Krassovsky et al. (1962).

$$O_3 + H \longrightarrow OH^*(v' \leq 9) + O_2 + 3.3eV \tag{3.12}$$

$$HO_2 + O \longrightarrow OH^*(v' \leq 6) + O_2 + 2.3eV \tag{3.13}$$

The ozone-hydrogen mechanism (Eq. 3.12) is considered the dominant source of OH* on a global basis (Bates and Nicolet, 1950), but the perhydroxyl-oxygen mechanism (Eq. 3.13) is the source of up to half of the OH*(v' $\leq$ 6) observed in the winter mesopause over Svalbard, due to the absence of photodissociation of HO_2 (Sivjee and Hamwey, 1987). The lower vibrational levels of OH*(v') are, in addition to the reactions above, believed to be pop-

Table 3.1.: Vibrational and rotational constants for OH*(6-2), taken from Chamberlain and Roesler (1955) and Krassovsky et al. (1962). Units are cm^{-1} for all constants except Y_v, which is dimensionless.

Vibrational constants		Rotational constants	v=6	v=2
ω_e	3737.90	B_v	14.349	17.108
$\omega_e x_e$	84.965	D_v	0.0018	0.0018
$\omega_e y_e$	0.5398	Y_v	-9.795	-8.214
$\omega_e z_e$	0.01674			
$\omega_e q_e$	-0.001637			

ulated as a result of either radiative cascade from the higher levels (Eq. 3.14) or stepwise collisional deactivation processes by atomic oxygen and molecular nitrogen and oxygen (Eq. 3.15) (Grygalashvyly, 2015; McDade, 1991):

$$OH^*(v) \longrightarrow OH^*(v') + hv \tag{3.14}$$
$$OH^*(v) + M \longrightarrow OH^*(v-1) + M \tag{3.15}$$

where v and v' denote the upper and lower vibrational levels, respectively. M is a non-reactive body, in this case O, O_2 and N_2. hv denotes the energy of the photon emitted.

Loss mechanisms for OH*(v') in the mesopause are quenching by atomic oxygen, molecular nitrogen and molecular oxygen (Eq. 3.16), chemical removal by atomic oxygen (Eq. 3.17) and radiative cascade to lower levels (Eq. 3.18) (Grygalashvyly, 2015):

$$OH^*(v') + M \longrightarrow OH^*(v'-1) + M \tag{3.16}$$
$$OH^*(v') + O \longrightarrow H + O_2 \tag{3.17}$$
$$OH^*(v') \longrightarrow OH^*(v'') + hv \tag{3.18}$$

where M is O, O_2 and N_2. v' and v" denote the upper and lower vibrational levels, respectively. Quenching by molecular oxygen is considered the main loss mechanism (Adler-Golden, 1997).

3.2.2. Distribution and variation of OH*

Height distribution

The OH* emissions are centred at around 87 km altitude with a mean thickness of 8 km, according to rocket measurements (Baker and Stair, 1988). The balance between the rapid fall-off in ozone concentration with height and the more frequently occurring collisional quenching by atmospheric constituents at lower atmospheric levels is the reason why the OH* airglow layer is centred near 87 km height.

Different vibrational states of OH* have different emission peak altitudes. Bands originating from higher vibrational levels have higher emission peak altitudes than bands originating from lower levels. This is, according to the study by von Savigny et al. (2012), associated mainly with quenching by atomic oxygen. von Savigny et al. used a collisional cascade model to determine the effect of atomic and molecular oxygen on the dependence of observed vibrational levels. They found that the greatest contribution came from quenching by atomic oxygen. They explained this by the strong increase

of atomic oxygen concentration with increasing altitude. Hence, at higher altitudes, the lower vibrational levels are more strongly quenched by atomic oxygen relative to at lower altitudes, leading to decreasing populations of the lower vibrational states here.

Diurnal variation of OH*

The concentration of OH* in the mesopause varies according to the concentration of other atmospheric species. When the sun is up, it dissociates O_3 and O_2 according to these reactions:

$$O_3 \longrightarrow O_2 + O \qquad O_2 \longrightarrow 2O \tag{3.19}$$

Thus, during daytime (or periods of midnight sun) we have high concentrations of O compared to O_2 and O_3, and hence, from Eq. 3.12, low concentrations of OH*. When the sun sets, rapid recombination of O back into O_2 and O_3 starts, according to, amongst others, these reactions:

$$2O \longrightarrow O_2 \qquad O + O_2 + M \longrightarrow O_3 + M \tag{3.20}$$

where M is a non-reactive body (Chapman, 1931). Since O is abundant during daytime, O_3 rapidly starts forming when the sun sets. Hence, the OH* concentration and intensity increase rapidly from about 5 degrees solar depression angle, which corresponds to sunset at 90 km height. At some point, the O_3 production slows as O concentration decreases. As a result, the OH* concentration and intensity decrease. Hence, OH* intensity and temperature tend to experience a small increase just after sunset, followed by a decrease (Patrick Espy, pers. comm., 2016). The diurnal variation of OH* has not been investigated in this PhD thesis.

Annual variation of OH*

The number density and peak height of the OH* layer at nighttime at high latitudes are directly proportional to atomic oxygen concentration (Grygalashvyly, 2015). The highest number densities and lowest altitudes of the OH* layer are found in winter. This corresponds to downwelling of air associated with the annual variation of the mesospheric residual circulation and thus downward mixing of atomic oxygen from the ionosphere into the polar mesopause region. Conversely, upwelling of air during summer decreases atomic oxygen concentration and hence OH* density (Liu et al., 2008).

3.2.3. Effects of energetic particle precipitation on OH* airglow

As mentioned in Section 2.5, there is an ongoing investigation whether energetic particle precipitation (EPP) may affect OH* intensity and temperature. EPP creates odd nitrogen (NO_x = NO, NO_2) in the middle atmosphere, which affects ozone chemistry (Newnham et al., 2013, and references therein). Hence, EPP may affect the OH*. EPP produces odd nitrogen in the 80 km to 90 km region, which reacts with atmospheric species according to these reactions (Brasseur and Nicolet, 1973):

$$NO + O_3 \longrightarrow NO_2 + O_2 \tag{3.21}$$

$$NO_2 + O \longrightarrow NO + O_2 \tag{3.22}$$

$$Net \qquad O_3 + O \longrightarrow 2O_2$$

Hence, in theory, one way EPP may affect the OH* is by reducing the amount of O_3 available in the mesopause region. Reaction 3.21 must compete with reaction 3.12 in order to remove O_3 and in this way reduce the OH* production. However, reaction 3.21 is slower than reaction 3.12. This could, in theory, be compensated by a higher NO production, but there is never enough NO present in the airglow region for reaction 3.21 to equal reaction 3.12, not even during heavy geomagnetic storms.

A way EPP can affect OH* concentration is through altering concentrations of O, following reaction 3.22. The equilibrium of the reactions above shifts according to the amount of O present in the 80 km to 90 km height region. The more O available, the greater tendency of equilibrium towards NO, since reaction 3.22 then occurs frequently. The less O available, the greater tendency of equilibrium towards NO_2, since reaction 3.22 occurs not so frequently. To conclude, we have less O available to form O_3 and hence OH* in the mesopause with NO present, produced by EPP (Patrick Espy, pers. comm., 2016).

3.3. Retrieval of OH*(6-2) temperatures

OH* rotational temperature can be derived from the intensities of rotational lines, and the intensity of each rotational line can be expressed as:

$$I_{v',J' \to v'',J''} = N_{v',J'} A_{v'J' \to v'',J''} \tag{3.23}$$

where $N_{v',J'}$ is the total concentration of OH* molecules in the highest rotational level and $A_{v'J' \to v'',J''}$ is the transition probability, or the total rate at

which radiative transitions occur between *v'* and *v"* (Mies, 1974). *A* is also called Einstein coefficient. In *Paper 1* and *Paper 2*, we have used Einstein coefficients from Mies (1974).

When deriving temperatures from the rotational distribution of OH*, we assume that the OH* molecules in the mesopause are following a Boltzmann distribution. A Boltzmann distribution gives the probability that a system will be in a certain state as a function of that state's energy and the temperature of the system, and assumes thermodynamical equilibrium (Gibbs, 1902). Reaction 3.12 produces OH* in highly excited rotational states, such that the initial rotational distribution is non-Boltzmann for energy states with very short radiative lifetimes. OH* (v' > 2) undergo on the average at least 10 collisions before emitting photons and thus have relatively long radiative lifetime, which indicates local thermodynamical equilibrium (Sivjee, 1992). Further discussion on this matter can be found in *Paper 2*. The assumption of a Boltzmann distribution of the rotational levels in a certain vibrational state allows us to express the total concentration of molecules in the highest rotational level as:

$$N_{v',J'} = N_{v'} \frac{2(2J'+1)}{Q_r} e^{\frac{-F(J')hc}{kT_{rot}}} \tag{3.24}$$

where Q_r, the electronic-rotational partition function for the *v'* levels, is defined as:

$$Q_r = \sum_{J'} 2(2J'+1) e^{\frac{-F(J')hc}{kT_{rot}}} \tag{3.25}$$

$F(J')$ is the upper rotational term, $N_{v'}$ is the total number of molecules in the system, k is the Boltzmann constant and T_{rot} is rotational temperature (Mies, 1974). Q_r can also be expressed as:

$$Q_r = 1 + 3e^{\frac{-2B_v hc}{kT_{rot}}} + 5e^{\frac{-6B_v hc}{kT_{rot}}} + ... \approx \frac{kT_{rot}}{B_v hc} \tag{3.26}$$

The approximation in Eq. 3.26 holds for sufficiently large T or small B_v and is valid for OH* in the mesopause (Herzberg, 1950). Combining Eqs. 3.23, 3.24 and 3.26 yields:

$$I_{v',J' \to v'',J''} = N_{v'} A_{v',J' \to v'',J''} \frac{2(2J'+1)hcB_v}{kT_{rot}} e^{\frac{-F(J')hc}{kT_{rot}}} \tag{3.27}$$

In Eq. 3.27, both $N_{v'}$ and T_{rot} are unknowns. Therefore, it is only possible to calculate the relative line strengths, making it necessary to have at least two lines in a rotational-vibrational band to obtain a temperature. Taking the logarithm of Eq. 3.27 gives:

Figure 3.6.: The Kjell Henriksen Observatory.

$$ln\left(\frac{I_{v',J'\rightarrow v'',J''}}{2(2J'+1)A_{v',J'\rightarrow v'',J''}}\right) = ln\left(\frac{N_{v'}hcB_v}{kT_{rot}}\right) - \frac{F(J')hc}{kT_{rot}} \tag{3.28}$$

Plotting $ln(\frac{I}{2(2J'+1)A})$ against the rotational term F(J') should yield a straight line when the system is in thermodynamical equilibrium and is referred to as a Boltzmann plot. Rotational temperatures can be derived from the slope of a linear fit to the Boltzmann plot.

3.4. Experimental

The Ebert-Fastie spectrometer, that has been providing OH* airglow spectra in this study, is located in Longyearbyen, Svalbard. From 1983 to 2007, the measurements were conducted at the Auroral Station in Adventdalen (78.20°N, 15.82°E), about 4 km away from town. In 2007, the spectrometer was moved to the Kjell Henriksen Observatory (KHO) (78.15°N, 16.04°E), see Figure 3.6. An increasing demand for more space at the Auroral Station led to the construction of a new and modern observatory. KHO is located at 520 m altitude, at the mountain Breinosa, approximately 15 km from the centre of Longyearbyen. Figure A.2 in the Appendix shows the locations of the old station relative to the KHO. For most of the year, the road to the KHO is partly covered with snow and is only accessible with track-laying vehicle, which makes the location remote and favourable with respect to artificial light pollution from town, cars and snowmobiles.

In Longyearbyen, the Sun remains below the horizon for nearly four months during winter. This allows for uninterrupted diurnal measurements of OH* airglow around winter solstice.

3.4.1. 1 m Ebert-Fastie spectrometer

The 1 m focal length Ebert-Fastie spectrometer scans the wavelength region between 8240 Å and 8705 Å in first order, enveloping the P branch of the OH*(6-2) vibrational band. Instrumental bandpass is 5 Å. The instrument scans one spectrum every 25 s. Field of view is approximately 5 degrees in the zenith direction. The cone angle is slightly larger in the direction parallel to the entrance slit, which results in an area of measurement of ∼9 km × 12 km at 90 km altitude. A photo of the spectrometer together with experimental setup are shown in Figure 3.7. Further details on the spectrometer can be found in Sigernes et al. (2003).

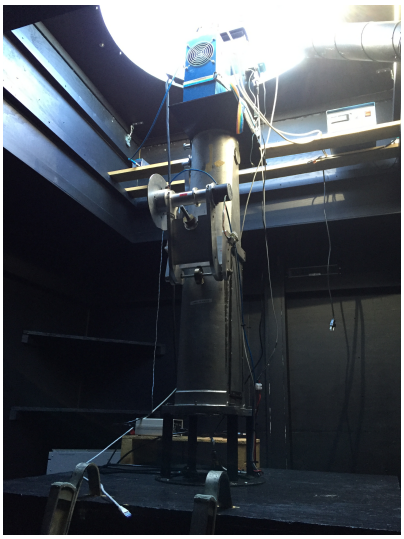

a)

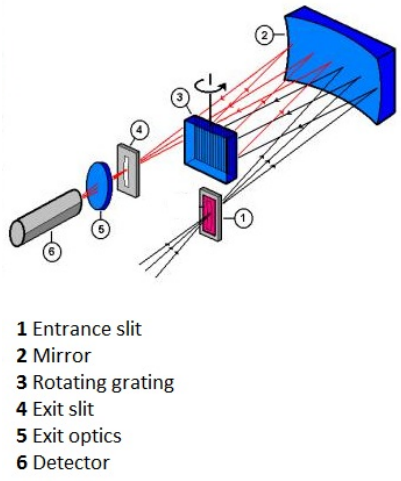

b)

Figure 3.7.: Photo (a) and experimental setup (b) of the Ebert-Fastie spectrometer located at the KHO, Longyearbyen. Experimental setup sketch courtesy of Fred Sigernes, UNIS.

Measurements of OH* airglow intensities in Longyearbyen using Ebert-Fastie spectrometers date back to the late 1970s. From 1983, intensity measurements of the OH*(6-2) band have been conducted on a regular basis. Measurements are conducted from November through February, when the Sun is 10° or more below the horizon.

A number of papers on OH* airglow rotational temperatures obtained from Ebert-Fastie spectromenters in Longyearbyen have been published in the last three decades. The focus of research during the 1980s was mainly on seasonal and diurnal variations, gravity wave interactions and sudden stratospheric warming events (Myrabø, 1984; Myrabø et al., 1984; Sivjee et al., 1987; Viereck and Deehr, 1989; Walterscheid et al., 1986). The last decade, the focus has been mostly on trends, coupling mechanisms and methods for

inferring OH* peak layer heights (Dyrland et al., 2010; Dyrland and Sigernes, 2007; Mulligan et al., 2009; Sigernes et al., 2003).

3.4.2. Data analysis

As described in Section 3.3, there are two unknowns in the equation we have for solving the rotational temperature, T_{rot}, and it is therefore only possible to calculate the relative strengths of the rotational lines. In this PhD project, we have derived rotational temperatures from measured spectra with the aid of synthetic spectra. The technique used is described as follows.

First, we made hourly averages of the measured airglow spectra. After calculating a linear background, synthetic spectra were iterated to fit the measured spectra. The background was found by linearly fitting an offset value to data points at the background level in between the specific emission lines. Furthermore, all hourly spectra were passed through a procedure for classifying them as "good" or "poor". The selection criteria for "good" spectra were based on experience and consistency for the whole dataset and are listed in *Paper 2*. Spectra were classified as "poor" e.g. when the background level was high, due to scattering of moonlight or artificial light from clouds, or when we had contamination by the auroral line OI 8446 Å, which is located close to the $P_2(4)$ line. We derived temperatures from the slope of a linear fit to a Boltzmann plot using $P_1(2)$, $P_1(3)$, $P_1(4)$ and $P_1(5)$ rotational line intensities of the OH*(6-2) vibrational band. These particular P_1 lines were chosen since rotational lines originating from states higher than J'=5 may not be in local thermodynamical equilibrium (Pendleton et al., 1993). The corresponding P_2 lines ($P_2(3)$, $P_2(4)$ and $P_2(5)$) were ensured to follow the same fit, even though they were not used for the temperature retrieval. If the P_2 fit is not close to the P_1 fit, the local thermal equilibrium assumption fails. We performed the sorting of data and calculation of rotational temperatures using the IDL program Spekkis and the Delphi program SyntheticOH (Sigernes et al., 2003). Figure 3.8 shows an hourly averaged spectrum of OH*(6-2) with a corresponding Boltzmann plot, handled in SyntheticOH. Further explanations on the temperature retrieval method can be found in *Paper 1* and *Paper 2*.

3.4.3. Uncertainties and limitations of OH* rotational temperature measurements

It is important to have in mind that a change in derived OH* temperature may be due to either a temperature change within the height distribution of OH*(6-2), a change in the height distribution itself, or a combination of both. We have discussed this matter in *Paper 2*, but the discussion will be repeated here. Ground-based instruments like the Ebert-Fastie spectrometer

measure the column-integrated emission rate contributed from the whole layer and lack height information. The fundamental study by Baker and Stair (1988) revealed that the mean altitude for the OH* emission layer peak height is around 87 km and that the mean emission layer thickness is about 8 km. However, several studies have addressed that the peak height of OH* emissions appears to vary with both season, local time, dynamical conditions and solar forcing (Dyrland et al., 2010; Liu and Shepherd, 2006; Shepherd et al., 2005; Yee et al., 1997). Also, OH* emissions originating from different vibrational bands peak at slightly different altitudes (von Savigny et al., 2012).

One option is to model the peak emission altitude, using OH* band intensities (integrated emission rates) measured by spectrometer and altitude profiles of OH* emission rates retrieved from satellite, as proposed by Mulligan et al. (2009). Mulligan et al. investigated peak emission altitude of the OH* layer over Svalbard using data from SABER (Sounding of the Atmosphere using Broadband Emission Radiometry) on board the TIMED (Thermosphere Ionosphere Mesosphere Energetics and Dynamics) satellite for parts of the 2003/2004 winter season. They found an inverse relationship between OH* peak altitude and emission rate, and provided a method for inferring peak altitude of the OH* emission layer using OH* integrated emission rates measured by spectrometer.

Thus, in theory, it is possible to acquire information about the altitude of the OH* layer and OH* temperatures simultaneously. However, TIMED was launched in December 2001, almost two decades after the beginning of the Longyearbyen OH* airglow temperature record. Also, SABER is in its southward-looking mode from mid-November to mid-January. In this period, which coincides with a large part of the OH* airglow measuring season, it is not covering the latitude at which Longyearbyen is located. We have not used Mulligan et al.'s method for modelling the peak emission altitude of the OH* layer in this PhD project.

Studies have shown that absolute values of derived OH* airglow temperatures may vary, depending on the choice of rotational transition probabilities and on the vibrational level of the transition's upper state (Cosby and Slanger, 2007; Noll et al., 2015; Turnbull and Lowe, 1989). However, studying OH* airglow temperatures on a long time scale, for instance by assessing long-term trends, and by looking at only one vibrational band, as is done in *Paper 2*, these matters are of less concern and have not been further elaborated in this PhD thesis.

Another limitation of the OH* airglow measurements is that the measurements are only conducted during night time/polar night. Also, spectra can be contaminated by aurora and scattering of moonlight or artificial light by clouds.

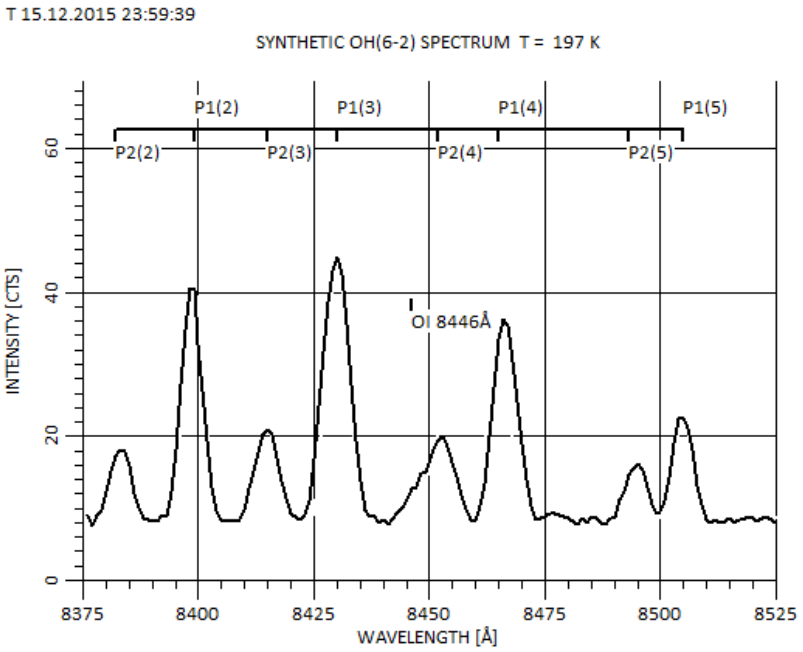

a) Spectrum of OH*(6-2), obtained by the 1 m Ebert-Fastie spectrometer on 15 December 2015 over Longyearbyen. Rotational lines from the P branch are denoted, as well as the OI 8446 Å auroral line, which contaminates the spectrum.

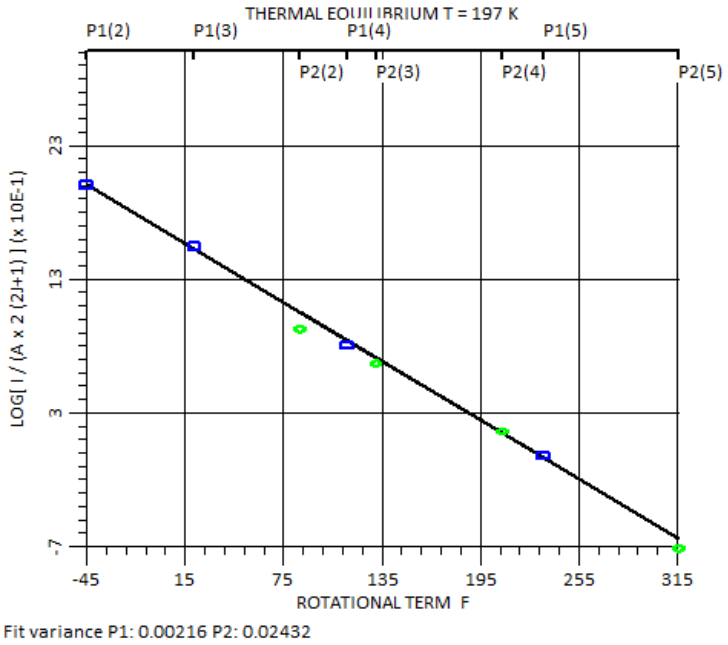

b) Boltzmann plot corresponding to the spectrum in a). Blue squares denote P_1 line intensities, while green triangles denote P_2.

Figure 3.8.

4. Atmospheric measurements using radar

While Chapter 3 described how we can retrieve temperatures from hydroxyl airglow, this chapter treats methods for retrieving atmospheric parameters using radar. In Section 4.1, the theory behind deriving temperature using meteor radar is presented, as well as a description of the instrumentation. The theory behind the derivation of turbopause height from turbulent energy dissipation rates using medium-frequency radar is presented in Section 4.2.

4.1. Mesopause temperatures derived from meteor echo fading times

4.1.1. From meteoroid to meteor echoes

A *meteoroid* is a small solid object (10 µm to 1 m) which travels in outer space (Rubin and Grossman, 2010). Some meteoroids enter Earth's atmosphere, where they are slowed down by friction with atmospheric gas molecules. The object is now called a *meteor*. The kinetic energy is converted into heat, and, entering the MLT region, this heat is sufficient to sublime and ionise the atoms and molecules at the surface of the meteor. The loss of mass from the surface of the meteor by sublimation is called *ablation*. The surrounding atmospheric gas is ionised as well. Most meteors are destroyed in the MLT region, due to ablation and to fragmentation because of the increasing aerodynamic pressure.

Meteor ablation results in a plasma trail that expands radially. This is due to *ambipolar diffusion*, which will be explained in the following section. Radio waves, sent from radars located at the ground, are scattered by the plasma trail. The scattering is divided into two categories, depending on whether the number of electrons produced per meter of path length is smaller or greater than a certain critical value. This corresponds to the plasma frequency being smaller or larger than the radar frequency. If smaller, the meteor trail is *underdense*, which means that the radio wave penetrates the plasma column freely, and each electron acts as an individual scattering source. If greater, the meteor trail is *overdense*, which means that the radio wave is reflected from the surface layer of the trail. It is the underdense echoes that are used

when deriving temperatures from meteor radars. If the trail is underdense, the echo received by the radar decays exponentially with a time constant, determined by the ambipolar diffusion coefficient and the wavelength of the radio wave (McKinley, 1961).

4.1.2. Ambipolar diffusion

Derivation of temperatures from meteor radar is based on the principle of ambipolar diffusion. The effect of ambipolar diffusion occurs in as ionised gas consisting of electrons and ions, as they move out in an electrically neutral cloud (McKinley, 1961). A meteor trail is an example of such an ionised gas. In a meteor plasma trail, electrons and ions move outwards with their respective thermal velocities. Due to their high temperature and low mass, the electrons' thermal velocities are higher than those of the ions. As the electrons move, they will leave behind the slower ions and a positive charge density, and an electric field will appear. The electric field will act on the charged species, slowing the more mobile electrons and accelerating the less mobile ions. When the diffusion flux of the positive charges equals that of the negative charges, the electrical current is zero, and we have ambipolar diffusion. The ambipolar diffusion coefficient is a measure of how fast the diffusion process is.

4.1.3. Retrieval of neutral temperatures from meteor radar

Assuming that ambipolar diffusion is the sole agent responsible for the decrease of electron density in a meteor trail, the backscattered radio wave amplitude from an underdense trail decreases exponentially with time, t, as

$$A(t) = A_0 e^{\frac{-t}{\tau}} \tag{4.1}$$

where A_0 is the wave amplitude at $t = 0$, typically at the time when exponential decay begins. τ is the measured echo decay time, which is the time it takes for the amplitude to fall to e^{-1} of its maximum value, expressed as:

$$\tau = \frac{\lambda^2}{16\pi^2 D_a} \tag{4.2}$$

where λ is the radar wavelength and D_a is the ambipolar diffusion coefficient (Jones, 1975). The assumption that ambipolar diffusion alone determines the rate of decay of echoes is valid for the altitude range 85 km to 95 km, as shown by e.g. Jones (1975), Hall et al. (2005), Ballinger et al. (2008) and discussed in *Paper 4*.

The Einstein diffusion relation states that for a collection of ions in a neutral gas, diffusion is related to ambient temperature and mobility of the ions:

$$D_i = \frac{k_B T_i K}{e} \tag{4.3}$$

where D_i is the ionic diffusion coefficient, k_B is Boltzmann constant, T_i is ion temperature and e is elementary charge. K is the zero-field mobility factor of the ions, which is the ions' ability to move through the gas in response to an electric field. We may write the ion mobility in terms of a "reduced mobility", K_0, by correcting K to standard gas density. K_0 at standard temperature and pressure is defined by the equation (Cervera and Reid, 2000; McDaniel and Mason, 1973):

$$K = \frac{1.013 \times 10^5}{p} \frac{T}{273.16} K_0 \tag{4.4}$$

Usually, a value for K_0 between $1.9 \times 10^{-4}\,\mathrm{m^2\,s^{-1}\,V^{-1}}$ and $2.9 \times 10^{-4}\,\mathrm{m^2\,s^{-1}\,V^{-1}}$ is chosen, depending on what ion one assumes to be the main ion of the trail (Hocking et al., 1997).

The ambipolar diffusion coefficient is, in the case of a negligible magnetic field, expressed as:

$$D_a \simeq D_i \left(1 + \frac{T_e}{T_i}\right) = 2 D_i \tag{4.5}$$

where T_e is electron temperature (Kaiser, 1953). Eq. 4.5 is valid for electrons and ions in thermal equilibrium in a meteor trail. Combining Eqs. 4.3, 4.4 and 4.5 gives the following relation between D_a, T and P:

$$D_a = 6.39 \times 10^{-2} \frac{T^2}{p} K_0 \tag{4.6}$$

Solving for T gives:

$$T = \sqrt{\frac{D_a p}{6.39 \times 10^{-2} K_0}} \tag{4.7}$$

The temperature estimate thus depends on D_a, which we obtain from the meteor decay time, τ (Eq. 4.2), pressure p and mobility factor K_0. Measurements of atmospheric pressure are difficult to obtain at 90 km height. In this PhD work, pressure values have been derived from atmospheric densities obtained from falling sphere measurements appropriate for 70°N, combining those of Lübken and von Zahn (1991) and Lübken (1999). In *Paper 4*, a value of $2.4 \times 10^{-4}\,\mathrm{m^2\,s^{-1}\,V^{-1}}$ was chosen for K_0, following Cervera and Reid (2000) and Holdsworth et al. (2006). Variations of K_0 have been further elaborated in *Paper 4*.

4.1.4. Nippon/Norway Tromsø Meteor Radar

The Nippon/Norway Tromsø Meteor Radar (NTMR) is located at Ramfjordmoen research station (69.58°N, 19.22°E), approximately 13 km from Tromsø, Norway. Figure A.3 in the Appendix shows the location of Ramfjordmoen relative to Tromsø. Most ground-based observations of the upper atmosphere from mainland Norway are conducted here. The NTMR was installed in November 2003 and is jointly operated by Tromsø Geophysical Observatory, which is a part of The University of Tromsø - The Arctic University of Norway, and National Institute for Polar Research, Japan. The meteor radar is operating at 30.25 MHz, and transmitting power is 7.5 kW (peak). It consists of one transmitter and five receiver antennas. All antennas are 3-element crossed Yagis. Field of view is approximately 70° off zenith. Figure 4.1 shows an image of one of the antennas, as well as the configuration of the antennas.

The NTMR detects decay times of echoes from ionised meteor trails in the MLT region. The decay times can be used to derive ambipolar diffusion coefficients, D_a, using Eq. 4.2, which again can be used to arrive at neutral temperatures in the height region ∼85 km to ∼95 km, using Eq. 4.7. Echoes are detected from a region within a radius of approximately 100 km (horizontal space), and around 10000 echoes are typically detected per day. The height and range resolution are both 1 km when looking at altitudes around the peak occurrence height of 90 km.

Publications of data retrieved from the NTMR during the last decade have treated temperatures and diffusivities (e.g. Hall et al., 2006, 2005b), winds (e.g. Hall et al., 2005a), as well as dynamics and dynamic changes in the MLT region (Hall and Tsutsumi, 2013; Kurihara et al., 2010).

4.1.5. Limitations and advantages of using a meteor radar for acquiring mesopause temperatures

A great advantage of the NTMR is that it is operated 24 hours a day, all year round, and that it conducts measurements regardless of cloud cover. The radar detects 200–600 echoes per hour at the peak occurrence height (90 km). The total number of detected meteor echoes results in sufficiently good statistics to allow for a 30 min temporal resolution. Another advantage is that the operational frequency of the radar is such that a simple time of flight estimation can be utilised to obtain the altitude of the meteor trails. From this we get the distance between the meteor echo and the radar, and hence we obtain the altitude of the meteor trails. This is contrary to e.g. airglow measurements, which yield temperature from the entire vertical column of the emitting airglow layer.

Using the NTMR for obtaining mesopause temperatures is advantageous,

a) One of the six identical antennas which constitute the Nippon/Norway Tromsø Meteor Radar. Image credit: Chris Hall.

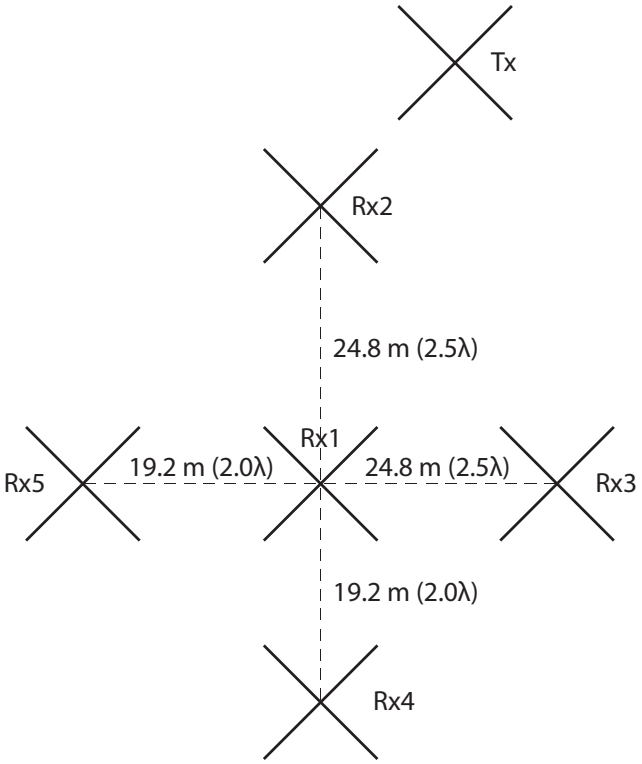

b) Sketch of the antenna configuration. Tx denotes the transmitting antenna, Rx1–5 denote the receiving antennas.

Figure 4.1.

due to that the detected meteor echoes are more evenly distributed, both spatially and temporally, compared to echoes detected at a low-latitude station. Meteor and planetary orbits are roughly coplanar, which means that they are on the same geometric plane. This results in that at high latitudes, many meteors traverse the field of view, contrary to at low latitudes, where there is a tendency of dawn head-on arrival of meteors.

We have thoroughly discussed the limitations of the meteor radar in *Paper 4*. In summary, the drawbacks for retrieving neutral temperatures are mostly associated with uncertainties in values chosen for pressure and the mobility factor. Using ambipolar diffusion coefficients derived from meteor radar measurements to calculate neutral atmospheric temperatures requires pressure values from the corresponding altitude. Measurements of pressure are rare at 90 km height, and often one has to rely on pressure values from models.

There is a possibility that D_a derived from the NTMR can be affected by modified electron mobility during auroral particle precipitation. In *Paper 4*, unrealistic enhancements of D_a due to particle precipitation were briefly investigated. Investigations concluded that approximately 5 % of hourly D_a values were unrealistic and hence rejected from further analysis.

The meteor radar is suitable for estimating neutral temperatures at around 90 km altitude. Above ∼95 km, gradient-drift Farley-Buneman instability may cause measured fading times higher than expected from ambipolar diffusion alone, leading to an underestimation of derived ambipolar diffusion coefficients (Ballinger et al., 2008; Dyrud et al., 2001; Kovalev et al., 2008). Below ∼85 km, higher diffusivity than expected according to theory may be encountered, due to reasons not fully understood (Hall et al., 2005b). Younger et al. (2014) attribute the higher diffusivity in the lower parts of the meteor region to chemically-induced neutralisation of underdense meteor plasma, initiated by three-body attachment of positive meteoric ions to neutral atmospheric molecules.

4.2. Turbopause height derived from turbulent energy dissipation rates

4.2.1. Turbulent energy dissipation rates

Measurements of turbopause altitude are difficult to conduct, mainly because direct measurements of small-scale fluctuations in neutral density, temperature and motion at around 100 km height are virtually impossible (Hall et al., 2008). One way of locating the turbopause is by estimating turbulent energy dissipation rates, ϵ, which are rates at which turbulent kinetic energy is converted into thermal internal energy, as explained in Section 2.4. ϵ is derived

from the conservation equation for turbulent kinetic energy.

From the fading times, or decay times, of backscattered signals received by a medium-frequency (MF) radar, we can obtain a measure of the intensity of turbulence (Hocking, 1983). The turbulent kinetic energy of the air may be represented by v'^2, which is the variance of wind velocity fluctuations, v', relative to the background wind, v. The relation between v' and radar echo fading times can be expressed as:

$$v' = \frac{\lambda\sqrt{ln2}}{4\pi\tau_c} \tag{4.8}$$

where λ is the radar wavelength and τ_c is the characteristic fading time of the signal (Briggs, 1980). The rate of dissipation of the turbulent kinetic energy is obtained by dividing by a characteristic time scale, since

velocity variance $\approx$ kinetic energy per unit mass
energy dissipation rate $\approx$ (kinetic energy per unit mass) per unit time

The Brunt-Väisälä period, $T_B = 2\pi/\omega_B$, where ω_B is the Brunt-Väisälä frequency, is proposed as a characteristic time scale. Since non-turbulent dynamics also can affect the signal fading times (will be further elaborated in Section 4.2.3), the estimates of turbulent energy dissipation rates obtained from radar measurements must be regarded as maximum values, or upper limits for turbulent energy dissipation present in the atmosphere (Hall, 2001). We therefore designate the estimates of turbulent energy dissipation rates obtained from radar ϵ_{max}. ϵ_{max} may be expressed as:

$$\epsilon_{max} = \frac{0.8v'^2\omega_B}{2\pi} \tag{4.9}$$

The factor 0.8 comes from an average of gravity waves over all directions in three dimensions (Weinstock, 1978).

The minimum energy dissipation rate, ϵ_{min}, present in the atmosphere, due to viscosity, is given by:

$$\epsilon_{min} = \frac{\omega_B^2\nu}{\beta} \tag{4.10}$$

where ν is kinematic viscosity and $\beta \equiv R_f/(1 - R_f)$ is the mixing or flux coefficient, related to the flux Richardson number, R_f. β lies between 0.2 and 1 (Hocking, 1987) and varies according to the assumed dominant turbulence scale. A large β is proposed for very large eddies. In *Paper 3*, a value of 0.3 has been chosen for β. This is in accordance with e.g. Fukao et al. (1994), who assume that the dominant turbulence scale is slightly smaller than the buoyancy scale.

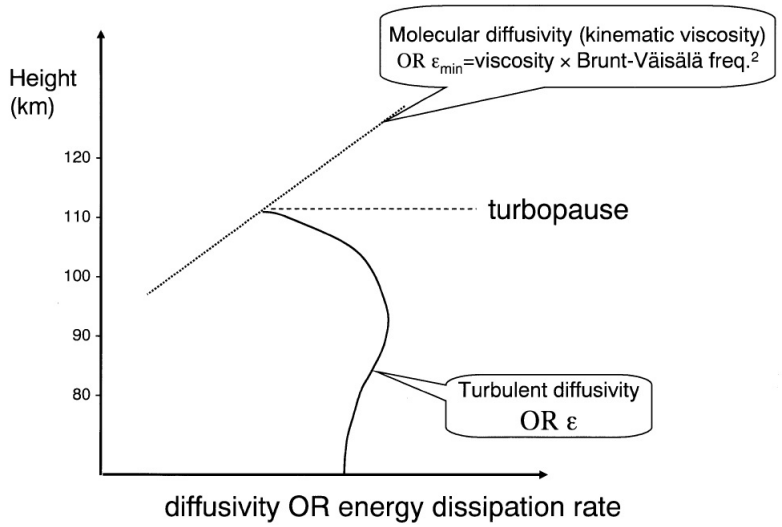

Figure 4.2.: Schematic presentation of the definition of the turbopause used in this PhD work. From: Hall (2001).

ϵ_{max} includes energy dissipation from all processes. In order to isolate those not related to viscosity, we end up with this expression for the turbulent energy dissipation rate, ϵ:

$$\epsilon = \epsilon_{max} - \epsilon_{min} \tag{4.11}$$

The height of the turbopause is identified as the altitude where $\epsilon = \epsilon_{min}$, which is where the energy dissipation rate corresponds to only molecular diffusion. See Figure 4.2 for an illustration.

4.2.2. Medium-frequency (MF) radar

The MF radar system at Ramfjordmoen became operational in 1975, as the first instrument of the research station. The radar is a collaboration between The University of Tromsø - The Arctic University of Norway, Nagoya University (Japan) and University of Saskatchewan (Canada). The purpose of the radar is to monitor winds and turbulence between 60 km and 120 km height. The radar is operating at 2.78 MHz, and transmitter power is 50 kW (peak). Transmission is performed through a 4 × 4 crossed dipole array, while reception is performed on three inverted V antennas arranged in an equilateral triangle. Height and time resolutions are 3 km and 5 min, respectively. Figure 4.3 shows an image of parts of the antenna system and the configuration of the antennas. Further details on the radar can be found in Hall (2001) and in *Paper 3*.

The principle behind the radar is that it illuminates irregularities in electron

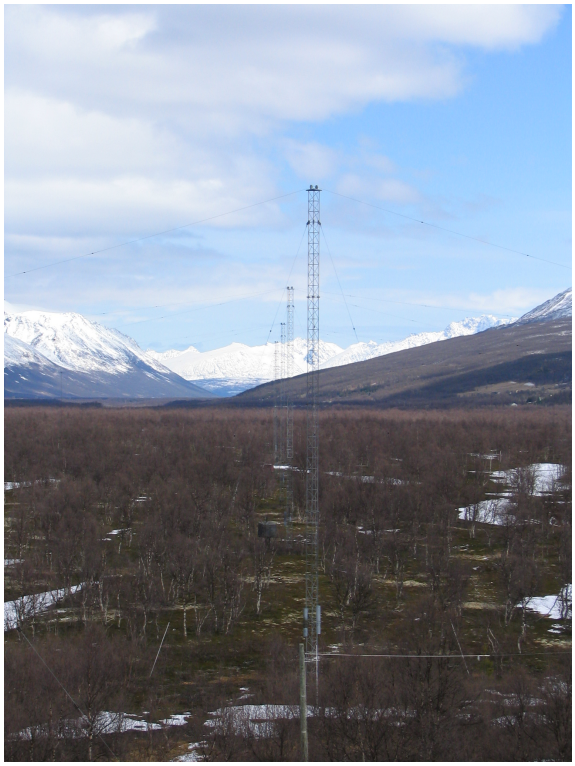

a) Parts of the MF antenna system located at Ramfjordmoen research station, Tromsø. Image credit: Tromsø Geophysical Observatory.

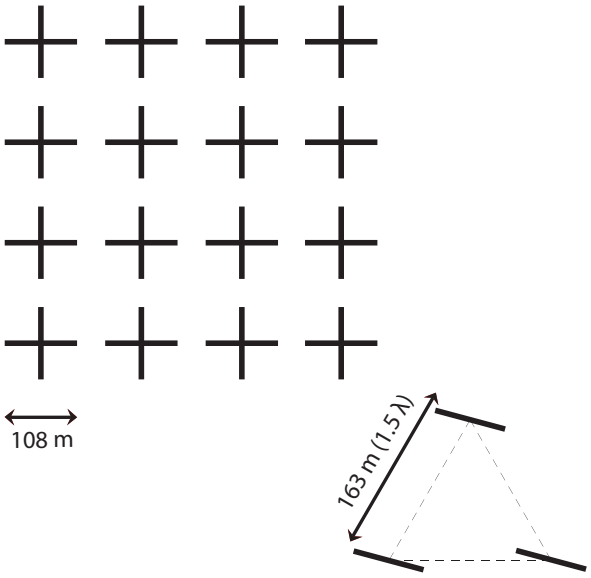

b) Configuration of the antennas. Transmission is performed through a 4 × 4 crossed dipole array, while reception is performed on three inverted V antennas.

Figure 4.3.

density, and backscatter from these structures forms a moving diffraction pattern at the ground, which is recorded by spaced antennas. The radar beam propagates vertically, surviving repeated partial reflections until being totally reflected by the high electron densities in the E region of the ionosphere. The reflected structures are moved by the background wind and perturbed by shorter timescale dynamics. Cross-correlations between signals received at the different antennas yield horizontal wind vector, typically between 50 km and 100 km height. Autocorrelations yield characteristic fading times of the echoes, which can be interpreted as turbulent intensity (Hall et al., 2008).

From the echo fading times, we may derive wind velocity fluctuations of the air, v' (Eq. 4.8). Furthermore, we get estimates of ϵ_{max} and therefore ϵ from v'^2 (Eqs. 4.9 and 4.11). Neutral atmosphere temperature (in the calculation of the Brunt-Väisälä frequency) and density (in the calculation of kinematic viscosity) are obtained from the NRLMSISE-00 Atmosphere Model (Picone et al., 2002).

Results from measurements obtained from the Tromsø MF radar have been widely published over a period of four decades. During the 1970s and early 1980s, research was mostly focused on investigations of electron density (e.g. Brekke et al., 1985; Hargreaves and Brekke, 1981), while investigations of winds were initialised in the early 1990s (e.g. Manson and Meek, 1991; Manson et al., 1992; Singer et al., 1994). Dynamical features like tides, GWs and PWs were investigated during the 1990s and 2000s (e.g. Forbes et al., 1994; Luo et al., 2002; Manson et al., 1999, 1990a,b). Eddy velocities estimated from characteristic fading times were estimated as early as 1978 (Schlegel et al., 1978), but it was not until the late 1990s that the estimation of turbulent intensities was continued and turbopause height was investigated (e.g. Hall et al., 2007, 1998a,b, 2008).

4.2.3. Instrument limitations and advantages

The Tromsø MF radar offers a height resolution of 3 km, meaning that it cannot be used to obtain detailed information about turbulent structure. The advantage of the radar is that it is able to examine gross features of turbulence in an altitude region which is inaccessible to other, higher-resolution techniques. Field of view is 15° off zenith, which means that the MF radar covers a smaller volume compared to e.g. the meteor radar, which estimates wind over a larger area. A smaller field of view indicates less interference of horizontal motions, e.g. GWs, which can shorten fading times (Hocking, 1983, 1985).

A drawback of using an MF radar to estimate turbulent energy dissipation rates is that the derived rates seem to be estimates of the upper limit for where turbulent kinetic energy is dissipated, due to an overestimation of fading

rates (Hocking, 1983). A radio wave is refracted slightly when it encounters small changes in the atmospheric conditions, e.g. changes in temperature, pressure, humidity or electron density irregularities. The radio wave will be more delayed the higher up into the ionosphere it goes, as electron density increases through the D region and lower E region, especially during heavy particle precipitation events. Thus, on occasion, we assume that the echo comes from a higher altitude than it actually does. As a consequence of this, the turbopause height estimated from turbulent energy dissipation rates from MF radar may be underestimated.

5. Main results

This chapter contains the main findings from *Papers 1–4*. Results from research conducted in this PhD work can be divided into two main categories: *seasonal variability* of mesopause region temperatures and *trends* of temperatures and turbopause height. In the following sections, we discuss and compare the results from the two locations – Tromsø and Longyearbyen – with results from other locations. Finally, we reflect briefly on the limitations of the work done in this PhD thesis.

5.1. Seasonal variability of polar mesopause region temperatures

5.1.1. OH*(6-2) airglow temperatures from Longyearbyen

We examined winter season variations of temperatures derived from OH*(6-2) airglow above Longyearbyen by performing a superposed epoch analysis of the temperatures (*Paper 1*). A superposed epoch analysis involves sorting all daily temperatures by day of year and then computing the means of all days of the year. In this way, a climatology is obtained. A 5-day running mean was applied in order to arrive at a winter climatology for the Longyearbyen OH*(6-2) dataset (Figure 4, *Paper 1*). We identified local temperature maxima in mid-January and mid-February, as well as a minimum in the transition between December and January.

5.1.2. Meteor radar temperatures from 90 km height over Tromsø

We applied Lomb-Scargle periodogram analysis to the daily temperatures from 90 km height obtained from the NTMR to identify periodic oscillations in the dataset (*Paper 4*). A Lomb-Scargle periodogram analysis is a method used for estimating a frequency spectrum based on a least-squares fit of sinusoids to a dataset and is a powerful way to find periodic signals. It is a modified discrete Fourier transform algorithm, and, contrary to discrete Fourier transform, suitable for unevenly spaced data (Lomb, 1976; Scargle, 1982). We found a number of statistically significant (>95 %) oscillations

with time scales ranging from 9 days to a year. The annual, semi-annual, ter-annual and quatra-annual oscillations were particularly pronounced.

We superposed daily temperatures by day of year and applied a least-squares fit, using periodic components found in the Lomb-Scargle analysis (see Figure 7, *Paper 4*). The seasonal variation showed higher temperatures and variability during winter compared to summer. We also found local temperature enhancements, or reduction of the strong seasonal negative gradient, just after spring equinox and summer solstice.

Temperature variability and seasonal variation may, to a large extent, be explained by the large-scale circulation in the middle atmosphere and corresponding wave activity. Higher temperature variability in winter is due to the presence of upward-propagating PWs during this season, in contrast to summer, when westward winds are blocking vertical propagation of long-period PWs into the MLT region. The particularly high variability in January and February is probably related to the occurrence of SSW events, which are more abundant at that time of year. Temperature increase after spring equinox, as seen in the seasonal variation, is related to the final breakdown of the polar vortex, as suggested by Shepherd et al. (2002). The local temperature increase during summer is most likely due to a combined effect of upward-propagating GWs and interhemispheric propagation of PWs, as found by e.g. Stray et al. (2014) and Hoffmann et al. (2010). The seasonal variation also showed a local temperature minimum around day 340, which we at this point lack physical explanations for.

5.1.3. Similarities/differences between Longyearbyen and Tromsø and comparison with other locations

The two datasets are not directly comparable, since the temperature retrieval methods are different. Also, the Longyearbyen time series contains only temperatures from November through February, while the Tromsø record is from all year round. As a consequence of this, we will not perform a thorough comparison between the two datasets. Nevertheless, a brief comparison of temperature variation during winter reveals some differences between the two datasets. While the Longyearbyen dataset shows a temperature minimum in the transition between December and January, the Tromsø dataset shows a local minimum around day number 340, corresponding to the beginning of December. Also, the pattern of higher variability in January and February in Tromsø temperatures is not apparent in the Longyearbyen dataset. The Longyearbyen dataset displays high variability throughout the winter.

The periodic components found in the NTMR temperature dataset have also been identified in datasets from other mid-latitude and high-latitude sites, e.g. Espy and Stegman (2002) (OH*(3-1) temperatures from Stock-

holm, 59.5°N), French and Burns (2004) (OH*(6-2) temperatures from Davis, Antarctica, 68.6°S) and Bittner et al. (2000) (OH*(3-1) temperatures from Wuppertal, 51°N). Bittner et al. (2000) and French and Burns (2004) also found additional sub-annual periodic oscillations, as well as other shorter-period components, in their datasets.

The local temperature minumum around day 340, found in the NTMR dataset, is found neither in the Stockholm nor the Davis temperatures. The Stockholm temperatures experience a minimum during the first days of the year (Figure 3, Espy and Stegman (2002)), more similar to the Longyearbyen OH*(6-2) dataset. Temperatures from Davis show a local decrease in July–August, corresponding to Northern Hemisphere January–February, which is completely different behaviour compared to our results.

It is difficult to conclude on what the reasons for different seasonal variability between the datasets are. The datasets may experience different seasonal variation due to that the locations may be influenced by different orographic and meteorological conditions, which again may influence the forcing from waves propagating from below.

5.2. Polar mesopause trends

5.2.1. OH*(6-2) airglow temperatures from Longyearbyen

We updated the OH* airglow temperature record from Longyearbyen with data from the winter seasons 2005/2006 to 2012/2013 (*Paper 1, Paper 2*) using the approach described in Section 3.4.

We subtracted the winter climatology, described in *Paper 1* and summarised in Section 5.1.1, from daily OH* temperatures to obtain residual temperatures. A multivariate regression fit was applied to the residuals to detect a long-term trend coupled with solar response. Solar response was investigated by looking into three different measures of solar variation: the F10.7 cm solar radio flux, the sunspot number and total solar irradiance. The highest correlation was achieved between OH* temperatures and total solar irradiance, but only slightly higher than for the other two. Due to that the F10.7 cm solar radio flux is the most commonly used measure of solar variability and the result therefore is easier to compare with other studies, the solar response coefficient was estimated using F10.7. We estimated the solar response coefficient, from the regression, to be $(3.6 \pm 4.0)\,\mathrm{K}/100$ SFU, and the trend from 1983 to 2013 was estimated to $(-0.2 \pm 0.5)\,\mathrm{K\,decade^{-1}}$ (*Paper 2*). The magnitude of the solar response coefficient is on the same level as results obtained from other mid-latitude and high-latitude sites (French and Klekociuk, 2011; Offermann et al., 2010; She and Krueger, 2004).

Also, we investigated monthly trends (*Paper 2*). All winter months showed

a positive trend, except for December. However, uncertainties are high, implying that the results from the monthly trend analysis are difficult to interpret.

5.2.2. Meteor radar temperatures from 90 km height over Tromsø

Before estimating a trend, we calibrated NTMR daily temperatures with respect to temperatures measured by the Microwave Limb Sounder on board the EOS (Earth Observing System) Aura spacecraft (*Paper 4*). This was necessary due to that ambipolar diffusion coefficients derived from meteor radar depend on both ambient atmospheric temperature and pressure. Due to lack of pressure measurements, we used pressure estimates obtained from falling spheres during the 1990s, appropriate for 70°N (Lübken, 1999; Lübken and von Zahn, 1991) in the temperature calculation.

We estimated the NTMR temperature trend from the approximation to the least-squares, composite fit of the sinusoids corresponding to periodic oscillations identified in the dataset. Temperature response to solar variability was not analysed, due to that the length of the time series was shorter than the corresponding solar cycle. We estimated an overall trend of $(-2.2 \pm 1.0)\,\mathrm{K\,decade^{-1}}$ from 2003 to 2014, while summer and winter trends were estimated to $(-0.3 \pm 3.1)\,\mathrm{K\,decade^{-1}}$ and $(-11.6 \pm 4.1)\,\mathrm{K\,decade^{-1}}$, respectively (*Paper 4*). Only the winter trend was considered significantly non-zero and detectable, following criteria in Weatherhead et al. (1998) and Tiao et al. (1990).

The most accepted theory behind a cooling of the middle atmosphere involves increased greenhouse gas emissions, but this matter still remains unsolved. The lack of response in the mesopause region compared to e.g. the stratosphere is, according to Schmidt et al. (2006), explained by changes in dynamics. Some dynamical processes contribute to a warming which counteracts the cooling expected from greenhouse gas emissions.

A less cooling trend in summer compared to winter may be explained by an increase in CO_2 radiative forcing, leading to a larger heat exchange from underlying layers, as the summer mesopause is considerably colder than the relatively warm layers below. Thus, we get a stronger equator-to-pole temperature gradient and stronger mid-latitude tropospheric westerlies. The result is a weakening of the GW drag on the MLT region and decreased adiabatic cooling (Fomichev et al., 2007; Schmidt et al., 2006). The net effect is a stronger cooling of the middle atmosphere in winter compared to summer, consistent with our results.

5.2.3. Similarities/differences between Longyearbyen and Tromsø and comparison with other locations

Due to that airglow intensities over Longyearbyen are only measured during winter, we can only compare winter trends from the two locations. The winter temperature trend for Tromsø is considerably more negative than the Longyearbyen trend. Other studies on long-term mesopause temperature trends from mid-latitude and high-latitude sites report mostly negative or near-zero trends (e.g. French and Klekociuk, 2011; Offermann et al., 2010). This is in line with the Longyearbyen OH*(6-2) winter trend, and the summer and overall trend of the Tromsø temperatures.

Beig (2011) states that there has been a shift in long-term trend assessments during the last decade from near-zero trends to negative trends. The author emphasises that a trend analysis is a snapshot of the time period covered, and that one of the reasons why different trend results vary is that the measurement periods differ. Hence, the different time spans may be one reason why the Tromsø winter temperature trend is significantly more negative than the Longyearbyen trend.

Other reasons for the deviating results can be that we compare temperatures obtained using different methods. The NTMR temperatures are obtained from 90 km geometric altitude, while the spectrometer, providing the OH*(6-2) temperatures, measures the column-integrated emission rate contributed from the whole airglow layer. Also, we used slightly different definitions of "winter" in the two trend assessments.

5.2.4. Turbopause height over Tromsø and comparison with other locations

We derived turbopause altitude estimates from turbulent energy dissipation rates obtained from the MF radar in Tromsø and investigated trend in altitudes. The height of the turbopause is located roughly around 100 km during summer and around 105 km in winter. We found an increasing height during the time period from 2001 until 2015 in summer, $(1.6 \pm 0.3)\,\mathrm{km\,decade^{-1}}$, while in winter turbopause height did not change significantly (*Paper 3*). We investigated the response of the change in turbopause heights to changing temperature (*Paper 4*), but changing temperature did not alter trends significantly, irrespective of season.

Paper 3 also treats turbopause height over Saskatoon, Canada (52°N, 107°W). Results show that turbopause height over Saskatoon does not change significantly over the time period from 1999 to 2014, regardless of season. We will not discuss the results from Saskatoon further in this PhD thesis. Other turbopause height trend studies that cover the same time period are few.

Oliver et al. (2014) analyse incoherent scatter radar measurements of ionospheric temperature and density above Millstone Hill (42.6°N, 71.5°W) over the years 1976 to 2013. They find a long-term atomic oxygen density increase at 120 km height and suggest that a descent in turbopause height can explain the increase. By visual examination (Oliver et al., 2014, Figure 6, bottom panel), a *decrease* in atomic oxygen density is evident from 2001 onwards. Following the suggestion of Oliver at al., this corresponds with an increase of turbopause height, which is in accordance with our results.

The exact mechanisms behind an increasing turbopause height during summer are not fully agreed upon, but possible explanations may include changes in dynamics. Hoffmann et al. (2011) found an increasing trend of mesospheric GWs at a midlatitude station during summer over the last two decades. One theory is that a trend in GW activity may influence the turbopause height trend.

5.3. Critical assessment of own work

5.3.1. Paper 1

In addition to the results summarised in Section 5.1.1, we presented daily temperatures retrieved from OH*(6-2) together with 10 hPa stratospheric reanalysis temperatures provided through the Modern-Era Retrospective-analysis for Research and Applications (MERRA) project (Rienecker et al., 2011) (see Figure 2, *Paper 1*). The original idea of including MERRA temperatures in the plot was to investigate the hypothesis of whether SSWs are preceded by a decrease in OH* temperatures, as reported in literature (e.g. Hoffmann et al., 2007; Walterscheid et al., 2000). However, by looking at measurements from only one station, at one height, we do not get the whole picture. From the plot it is hard to find clear signatures of mesospheric cooling preceding SSWs. This is, however, not equivalent to that the polar mesosphere did not cool. The cooling could have been confined to a region further down in the mesosphere. Also, SSWs may affect the mesospheric circulation with a longitudinal and latitudinal dependence (e.g. Hoffmann et al., 2007). Longyearbyen may have been located outside of the affected sector for some of the SSW events. In *Paper 1*, we did not elaborate further on this topic. The reason for this is that in order to investigate this particular hypothesis, it is necessary to look at more data than we did, e.g. temperature and wind measurements from additional stations and at different heights.

For some reason, no attempts were made to explain the seasonal variation found in the dataset, other than stating that the temperature minimum, noticeable in the transition between December and January, is consistent with previous investigations of the dataset (Myrabø, 1986). Myrabø (1986) ex-

plained the temperature minimum in terms of changes in the GW activity and in the circulation, temperature and transport in the underlying atmosphere. Myrabø analysed four seasons of hydroxyl airglow temperatures from Longyearbyen and observed the temperature minimum regardless of SSW occurrence.

5.3.2. Paper 2

The uncertainties of the results obtained are large, for both the solar response coefficient and the trend. In *Paper 4*, we applied criteria from Weatherhead et al. (1998) and Tiao et al. (1990) in order to determine if the trend we found could be considered detectable and significantly non-zero. We did not perform the same procedure in *Paper 2*. Following the criteria, the Longyearbyen OH*(6-2) airglow temperature trend cannot be considered neither significantly non-zero nor detectable. In fact, according to the formulation (Weatherhead et al., 1998, Eq. 3) the number of years required for a detectable trend is 180. The small magnitude of the trend and the large standard deviation of the time series explain why this number is so large.

Weatherhead et al. (1998) stress the importance of accounting for level shifts in the data, caused when e.g. instrument location changes, or when an instrument is modified. The Ebert-Fastie spectrometer was moved from the Auroral Station in Adventdalen to the Kjell Henriksen Observatory in 2007, and it has gone through upgrades including changing counter cards, high voltage supplies, pulse amplifier/discriminator, photomultiplier tube and cooler. Even though upgrades are inevitable for a spectrometer operating over a time period of more than 30 years, such operations will affect the performance of the instrument. Ignoring them can result in artificial trends in the data not representative for the actual temperature change. Often one does not know the magnitude of such level shifts, but knowing the time for the occurring level shifts enables us to account for them. Level shifts result in increased variance, and hence a lengthening of the time required for a detectable trend. Level shifts were not accounted for in *Paper 2*, and we do not know the effects of level shifts on the trend.

The number of observing days, which are days where we have minimum three hours of "good" data, varies a lot from one season to another. One anonymous referee suggested to perform a so-called bootstrap analysis, using randomised data points. The principle behind a bootstrap analysis is to select the same number of data points from each season, repeat the randomisation many times and then plot the distribution of the means or medians per season. We did not perform this procedure in the trend analysis. However, it would be useful to do this and check if it would change the statistics and conclusions significantly.

Using temperatures obtained from airglow intensities results in a masking of certain atmospheric conditions. For instance will spectra obtained during periods of strong aurora or thick tropospheric cloud cover be classified as "poor" and filtered out of the dataset. Avoiding this is not possible when using airglow temperatures, but one option is to compare the airglow temperatures with e.g. temperatures obtained from the Nippon/Norway Svalbard Meteor Radar located in Adventdalen.

5.3.3. Paper 3

The increasing turbopause height during summer is commensurate with decreasing atomic oxygen concentrations, as proposed by Oliver et al. (2014). A suggestion for making a more direct geographic comparison would be to e.g. analyse the trend in atomic oxygen retrieved from the SCIAMACHY instrument on board the Envisat satellite. SCIAMACHY provided atomic oxygen concentration profiles from the MLT region from 50°S to 75°N from 2002 to 2012, covering a large part of the turbopause height dataset.

5.3.4. Paper 4

The meteor radar temperature dataset does not cover a complete solar cycle, and hence it is not long enough for including the solar response in the trend. We had to go through many steps to calibrate the temperatures with respect to Aura MLS temperatures, which are associated with considerable uncertainties at mesopause heights.

We proposed explanations for the seasonal variation of temperatures, involving GW and PW activity affecting atmospheric circulation. However, we did not include any actual analysis of GWs or PWs from observations. It is possible to extract PW activity from meridional wind anomalies using SuperDARN radars, as conducted by Stray et al. (2014). It is not possible to extract GW momentum flux with the instrumentation we have available in Tromsø.

6. Concluding remarks

In this thesis, we have worked towards a better understanding of processes responsible for temperature variability in the polar mesopause region. We have also investigated trends in temperature obtained from this region and in turbopause height. In order to investigate these main objectives, we have utilised data from two high-latitude stations: Tromsø (70°N, 19°E) and Longyearbyen (78°N, 16°E). A 1 m Ebert-Fastie spectrometer located at the Kjell Henriksen Observatory in Longyearbyen has been providing hydroxyl airglow temperatures for more than 30 years, making the Longyearbyen OH*(6-2) temperature record one of the longest time series of hydroxyl airglow winter temperatures in the world. Most of the ground-based measurements of the upper atmosphere from mainland Norway are conducted from Ramfjordmoen research station near Tromsø. Ramfjordmoen houses, amongst others, a medium-frequency radar and a meteor radar. The Nippon/Norway Tromsø Meteor Radar has been providing neutral temperatures from the mesopause region since 2003 by measuring decay times of echoes from ionised meteor trails. The great advantage of the meteor radar is its ability to conduct measurements of meteor echo decay times 24 hours a day, all year round, and the temperature record has very few data gaps. The medium-frequency radar has been operational for more than 40 years and has provided turbulent energy dissipation rates, which can be used to derive turbopause height, since 2000.

Seasonal variability of polar mesopause region temperatures obtained from the Ebert-Fastie spectrometer and the NTMR radar was investigated, and we found that the two datasets experience different seasonal variability. The Longyearbyen dataset experience local temperature maxima in mid-January and mid-February, as well as a minimum in the transition between December and January. In the NTMR dataset we identified periodic variations with periods ranging from 9 days to a year and local temperature enhancements after spring equinox and summer solstice. Even though solar variability and energetic particles precipitating in this region may have an effect on the temperature variability, the largest contributors are dynamic processes. Seasonal variation of temperature, and variability within this variation, correspond well to characteristic behaviour of the large-scale circulation in the middle atmosphere and corresponding wave activity. The fact that the winter climatology differs between Longyearbyen and Tromsø suggests that differences in local orographic forcing may play a large role.

The OH*(6-2) airglow winter temperature trend and the annual and summer NTMR temperature trends were estimated to be near-zero or slightly negative. The estimated NTMR winter trend was negative, $(-11.6 \pm 4.1)\,\mathrm{K\,decade^{-1}}$. The temperature trends obtained in this PhD project are in line with results from other studies on MLT temperatures at mid- and high-latitudes, as well as model studies (e.g. Beig, 2011; French and Klekociuk, 2011; Offermann et al., 2010; Schmidt et al., 2006), indicating zero or slightly negative trends. Increasing greenhouse gas emissions, which may lead to changes in dynamics, is proposed as the main driver behind a cooling of the middle atmosphere (e.g. Akmaev and Fomichev, 2000). The stronger cooling trend found in winter for the NTMR dataset is also found in other studies. This has in other studies been explained by effects associated with CO_2 radiative forcing (Fomichev et al., 2007; Schmidt et al., 2006).

The response on mesopause region temperatures to solar variability was investigated for the Longyearbyen OH*(6-2) airglow temperatures, but not for the NTMR temperatures, due to that the time series was shorter than the corresponding solar cycle. The solar response coefficient, decoupled from the multivariate regression analysis performed on the OH* temperatures, was $(3.6 \pm 4.0)\,\mathrm{K/100\ SFU}$. The magnitude of the solar response coefficient is on the same level as results obtained from other mid-latitude and high-latitude sites (French and Klekociuk, 2011; Offermann et al., 2010; She and Krueger, 2004).

The large temperature variability, in both OH* airglow temperatures from Longyearbyen and meteor radar temperatures from Tromsø, makes trend assessments challenging. The variability strongly influences the precision of trend estimates, which again determines the number of years required to detect a trend of a given magnitude. Level shifts in the data, which are present in the Longyearbyen OH* airglow dataset, further lengthen the time required for a detectable trend. Neither the winter trend in OH* airglow temperatures from Longyearbyen nor the overall trend in Tromsø meteor radar temperatures is detectable. The negative NTMR winter trend is significantly non-zero and detectable, according to criteria in Tiao et al. (1990) and Weatherhead et al. (1998).

An increase in turbopause height of $(1.6 \pm 0.3)\,\mathrm{km\,decade^{-1}}$ over Tromsø is evident from 1999 to 2015 for summer, whereas for winter the turbopause height has not changed significantly. Increasing turbopause height during summer is commensurate with decreasing atomic oxygen concentrations over the same time period, as shown by Oliver et al. (2014). An increasing trend in GW activity during summer, found by e.g. Hoffmann et al. (2011), is a possible explanation for our findings.

The location of the turbopause is important for transport of atmospheric constituents, both upwards and downwards. Constituents produced in the

lower atmosphere are transported upwards due to turbulence, and the higher the turbopause, the higher up into the middle atmosphere the constituents are transported. Atomic oxygen is an example of an atmospheric component whose downward transport into the mesosphere is affected by turbopause height. Atomic oxygen is produced by dissociation of molecular oxygen in the ionosphere. When the turbopause is located at a low level, e.g. during summer, it may be below the lower limit of atomic oxygen production, and thus downward transport to the mesosphere does not occur. Transport of atomic oxygen into this region is important for ozone chemistry and hence hydroxyl airglow chemistry.

Whether or not the change in turbopause height over Tromsø affects the transport of atomic oxygen necessary for influencing airglow chemistry is difficult to investigate further. Airglow measurements have not been conducted from Tromsø during the same time period as turbulent energy dissipation rates have been measured by the MF radar. Hydroxyl airglow temperatures have been measured during winter at Arctic Lidar Observatory for Middle Atmosphere Research (ALOMAR) in Andøya (69°N, 16°E) since 2010. Since it is during summer that we have found a change in the turbopause height, it is difficult to investigate the effects of this on Arctic airglow measurements, due to the light conditions during Arctic summer.

7. Future perspectives

The work done in this PhD thesis opens up possibilities for new projects. As previously mentioned, airglow intensity is directly proportional to atomic oxygen concentration. Atomic oxygen concentration is measured by e.g. SCIAMACHY (between 50°S and 75°N) and could give important insights into both the evolution of turbopause height and its influence on airglow dynamics at high latitudes. A useful approach would be to examine the trend in atomic oxygen concentration measured by SCIAMACHY and compare with the trend in turbopause height, as well as results obtained by Oliver et al. (2014).

Regarding airglow variability over Longyearbyen, a lot is still undone. Topics that need further attention are related to the variability of the OH* layer altitude and number density with the diurnal cycle and in the context of e.g. GWs and SSWs, as well as long-term changes in the layer. Using ground-based measurements of OH* airglow temperatures from Longyearbyen in combination with satellite measurements of peak altitudes of the OH* layer, derived from integrated volume emission rates, would be valuable in this context. The new SuperDARN radar in Longyearbyen, operative since 2015, may also be used for studying gravity waves.

Also, identifying periodic oscillations in the OH* airglow dataset, as well as temperatures derived from the Nippon/Norway Svalbard Meteor Radar in Longyearbyen, would shed light on dynamics affecting the airglow layer over Svalbard. The results should be compared with the results obtained in *Paper 4*.

Other future projects could involve monitoring effects of energetic particle precipitation on mesopause temperatures obtained at high latitudes, using e.g. geomagnetic indices or particle fluxes measured by POES satellites.

Bibliography

Adler-Golden, S. (1997). "Kinetic parameters for OH nightglow modeling consistent with recent laboratory measurements". In: *Journal of Geophysical Research: Space Physics* 102.A9, pp. 19969–19976. DOI: 10.1029/97JA01622.

Akmaev, R. A. and V. I. Fomichev (1998). "Cooling of the mesosphere and lower thermosphere due to doubling of CO_2". In: *Annales Geophysicae* 16.11, pp. 1501–1512. DOI: 10.1007/s00585-998-1501-z.

Akmaev, R. A. and V. I. Fomichev (2000). "A model estimate of cooling in the mesosphere and lower thermosphere due to the CO_2 increase over the last 3–4 decades". In: *Geophysical Research Letters* 27.14, pp. 2113–2116. DOI: 10.1029/1999GL011333.

Andrews, D. G., J. R. Holton, and C. B. Leovy (1987). *Middle atmosphere dynamics*. International geophysics series 40. Academic press.

Baker, D. J. and A. T. Stair (1988). "Rocket measurements of the altitude distributions of the hydroxyl airglow". In: *Physica Scripta* 37, pp. 611–622. DOI: 10.1088/0031-8949/37/4/021.

Ballinger, A. P., P. B. Chilson, R. D. Palmer, and N. J. Mitchell (2008). "On the validity of the ambipolar diffusion assumption in the polar mesopause region". In: *Annales Geophysicae* 26.11, pp. 3439–3443. DOI: 10.5194/angeo-26-3439-2008.

Bates, D. R. and M. Nicolet (1950). "The photochemistry of atmospheric water vapor". In: *Journal of Geophysical Research* 55.3, pp. 301–327. DOI: 10.1029/JZ055i003p00301.

Beig, G. (2011). "Long-term trends in the temperature of the mesosphere/lower thermosphere region: 1. Anthropogenic influences". In: *Journal of Geophysical Research: Space Physics* 116.A2. DOI: 10.1029/2011JA016646.

Beig, G., J. Scheer, M. G. Mlynczak, and P. Keckhut (2008). "Overview of the temperature response in the mesosphere and lower thermosphere to solar activity". In: *Reviews of Geophysics* 46.3. DOI: 10.1029/2007RG000236.

Bittner, M., D. Offermann, and H. H. Graef (2000). "Mesopause temperature variability above a midlatitude station in Europe". In: *Journal of Geophysical Research: Atmospheres* 105.D2, pp. 2045–2058. DOI: 10.1029/1999JD900307.

Blamont, J.-E. (1963). "Turbulence in atmospheric motions between 90 and 130 km of altitude". In: *Planetary and Space Science* 10, pp. 89–101. DOI: 10.1016/0032-0633(63)90010-2.

Booker, J. R. and F. P. Bretherton (1967). "The critical layer for internal gravity waves in a shear flow". In: *Journal of Fluid Mechanics* 27.03, pp. 513–539. DOI: 10.1017/S0022112067000515.

Brasseur, G. and M. Nicolet (1973). "Chemospheric processes of nitric oxide in the mesosphere and stratosphere". In: *Planetary and Space Science* 21.6, pp. 939–961. DOI: 10.1016/0032-0633(73)90141-4.

Brekke, A., O. Holt, P. H. G. Dickinson, M. Friedrich, T. Hansen, P. Stauning, and E. V. Thrane (1985). "Development of D-region electron and ion densities under various auroral conditions during the Energy Budget Campaign (EBC)". In: *Journal of Atmospheric and Terrestrial Physics* 47.1, pp. 101–121. DOI: 10.1016/0021-9169(85)90127-8.

Brewer, A. W. (1949). "Evidence for a world circulation provided by the measurements of helium and water vapour distribution in the stratosphere". In: *Quarterly Journal of the Royal Meteorological Society* 75.326, pp. 351–363. DOI: 10.1002/qj.49707532603.

Briggs, B. H. (1980). "Radar observations of atmospheric winds and turbulence: A comparison of techniques". In: *Journal of Atmospheric and Terrestrial Physics* 42.9, pp. 823–833. DOI: 10.1016/0021-9169(80)90086-0.

Cervera, M. A. and I. M. Reid (2000). "Comparison of atmospheric parameters derived from meteor observations with CIRA". In: *Radio Science* 35.3, pp. 833–843. DOI: 10.1029/1999RS002226.

Chamberlain, J. W. (1961). *Physics of the Aurora and Airglow*. Academic press, New York.

Chamberlain, J. W. and F. L. Roesler (1955). "The OH Bands in the Infrared Airglow". In: *The Astrophysical Journal* 121, p. 541. DOI: 10.1086/146015.

Chapman, S. (1931). "Bakerian Lecture. Some phenomena of the upper atmosphere". In: *Proceedings of the Royal Society of London. Series A, Containing Papers of a Mathematical and Physical Character* 132.820, pp. 353–374.

Charney, J. G. and P. G. Drazin (1961). "Propagation of planetary-scale disturbances from the lower into the upper atmosphere". In: *Journal of Geophysical Research* 66.1, pp. 83–109. DOI: 10.1029/JZ066i001p00083.

Cosby, P. C. and T. G. Slanger (2007). "OH spectroscopy and chemistry investigated with astronomical sky spectra". In: *Canadian Journal of Physics* 85.2, pp. 77–99. DOI: 10.1139/p06-088.

Czechowsky, P., I. M. Reid, and R. Rüster (1988). "VHF radar measurements of the aspect sensitivity of the summer polar mesopause echoes over

Andenes (69°N,16°E), Norway". In: *Geophysical Research Letters* 15.11, pp. 1259–1262. DOI: 10.1029/GL015i011p01259.

Danilov, A. D., U. A. Kalgin, and A. A. Pokhunkov (1979). "Variation of the turbopause level in the polar regions". In: *Space Research XIX* 173.

Dickinson, R. E. (1978). "Rossby waves–long-period oscillations of oceans and atmospheres". In: *Annual Review of Fluid Mechanics* 10.1, pp. 159–195. DOI: 10.1146/annurev.fl.10.010178.001111.

Dobson, G. M. B. (1956). "Origin and distribution of the polyatomic molecules in the atmosphere". In: *Proceedings of the Royal Society of London. Series A, Mathematical and Physical Sciences* 236.1205, pp. 187–193.

Dowdy, A. J., R. A. Vincent, D. J. Murphy, M. Tsutsumi, D. M. Riggin, and M. J. Jarvis (2004). "The large-scale dynamics of the mesosphere–lower thermosphere during the Southern Hemisphere stratospheric warming of 2002". In: *Geophysical Research Letters* 31.14. DOI: 10.1029/2004GL020282.

Dunkerton, T. (1978). "On the mean meridional mass motions of the stratosphere and mesosphere". In: *Journal of the Atmospheric Sciences* 35.12, pp. 2325–2333. DOI: 10.1175/1520-0469(1978)035<2325:OTMMMM>2.0.CO;2.

Dunkerton, T. J. (1991). "LIMS (Limb Infrared Monitor of the Stratosphere) observation of traveling planetary waves and potential vorticity advection in the stratosphere and mesosphere". In: *Journal of Geophysical Research: Atmospheres* 96.D2, pp. 2813–2834. DOI: 10.1029/90JD02340.

Dyrland, M. E., F. J. Mulligan, C. M. Hall, F. Sigernes, M. Tsutsumi, and C. S. Deehr (2010). "Response of OH airglow temperatures to neutral air dynamics at 78°N, 16°E during the anomalous 2003–2004 winter". In: *Journal of Geophysical Research* 115 (D07103). DOI: 10.1029/2009JD012726.

Dyrland, M. E. and F. Sigernes (2007). "An update on the hydroxyl airglow temperature record from the Auroral Station in Adventdalen, Svalbard (1980–2005)". In: *Canadian Journal of Physics* 85.2, pp. 143–151. DOI: 10.1139/p07-040.

Dyrud, L. P., M. M. Oppenheim, and A. F. vom Endt (2001). "The anomalous diffusion of meteor trails". In: *Geophysical Research Letters* 28.14, pp. 2775–2778. DOI: 10.1029/2000GL012749.

Ecklund, W. L. and B. B. Balsley (1981). "Long-term observations of the Arctic mesosphere with the MST radar at Poker Flat, Alaska". In: *Journal of Geophysical Research: Space Physics* 86.A9, pp. 7775–7780. DOI: 10.1029/JA086iA09p07775.

Eliassen, A. and E. Palm (1961). "On the transfer of energy in stationary mountain waves". In: *Geofysiske Publikasjoner* 22, pp. 1–23.

Espy, P. J. and J. Stegman (2002). "Trends and variability of mesospheric temperature at high-latitudes". In: *Physics and Chemistry of the Earth, Parts A/B/C* 27.6, pp. 543–553. DOI: 10.1016/S1474-7065(02)00036-0.

Fels, S. B. (1985). "Radiative-dynamical interactions in the middle atmosphere". In: *Advances in Geophysics* 28, pp. 277–300. DOI: 10.1016/S0065-2687(08)60227-7.

Fleming, E. L., S. Chandra, J. J. Barnett, and M. Corney (1990). "Zonal mean temperature, pressure, zonal wind and geopotential height as functions of latitude". In: *Advances in Space Research* 10.12, pp. 11–59. DOI: 10.1016/0273-1177(90)90386-E.

Fomichev, V. I., A. I. Jonsson, J. De Grandpre, S. R. Beagley, C. McLandress, K. Semeniuk, and T. G. Shepherd (2007). "Response of the middle atmosphere to CO_2 doubling: Results from the Canadian Middle Atmosphere Model". In: *Journal of Climate* 20.7, pp. 1121–1144. DOI: 10.1175/JCLI4030.1.

Forbes, J. M., A. H. Manson, R. A. Vincent, G. J. Fraser, F. Vial, R. Wand, S. K. Avery, R. R. Clark, R. Johnson, R. Roper, R. Schminder, T. Tsuda, and E. S. Kazimirovsky (1994). "Semidiurnal tide in the 80–150 km region: an assimilative data analysis". In: *Journal of Atmospheric and Terrestrial Physics* 56.10, pp. 1237–1249. DOI: 10.1016/0021-9169(94)90062-0.

French, W. J. R. and G. B. Burns (2004). "The influence of large-scale oscillations on long-term trend assessment in hydroxyl temperatures over Davis, Antarctica". In: *Journal of Atmospheric and Solar-Terrestrial Physics* 66.6, pp. 493–506. DOI: 10.1016/j.jastp.2004.01.027.

French, W. J. R., G. B. Burns, K. Finlayson, P. A. Greet, R. P. Lowe, and P. F. B. Williams (2000). "Hydroxyl (6-2) airglow emission intensity ratios for rotational temperature determination". In: *Annales Geophysicae* 18.10, pp. 1293–1303. DOI: 10.1007/s00585-000-1293-2.

French, W. J. R. and A. R. Klekociuk (2011). "Long-term trends in Antarctic winter hydroxyl temperatures". In: *Journal of Geophysical Research: Atmospheres* 116.D4. DOI: 10.1029/2011JD015731.

Fritts, D. C. (1984). "Gravity wave saturation in the middle atmosphere: A review of theory and observations". In: *Reviews of Geophysics* 22.3, pp. 275–308. DOI: 10.1029/RG022i003p00275.

Fritts, D. C. and M. J. Alexander (2003). "Gravity wave dynamics and effects in the middle atmosphere". In: *Reviews of Geophysics* 41.1. DOI: 10.1029/2001RG000106.

Fukao, S., M. D. Yamanaka, N. Ao, W. K. Hocking, T. Sato, M. Yamamoto, T. Nakamura, T. Tsuda, and S. Kato (1994). "Seasonal variability of vertical eddy diffusivity in the middle atmosphere: 1. Three-year observations by the middle and upper atmosphere radar". In: *Journal of Geophysical Research: Atmospheres* 99.D9, pp. 18973–18987. DOI: 10.1029/94JD00911.

Garcia, R. R. and S. Solomon (1985). "The effect of breaking gravity waves on the dynamics and chemical composition of the mesosphere and lower thermosphere". In: *Journal of Geophysical Research: Atmospheres* 90.D2, pp. 3850–3868. DOI: 10.1029/JD090iD02p03850.

Gibbs, J. W. (1902). *Elementary principles in statistical mechanics*. Scribner's sons, New York.

Grygalashvyly, Mykhaylo (2015). "Several notes on the OH* layer". In: *Annales Geophysicae* 33, pp. 923–930. DOI: 10.5194/angeo-33-923-2015.

Hall, C. (2001). "The Ramfjordmoen MF radar (69°N, 19°E): application development 1990–2000". In: *Journal of Atmospheric and Solar-Terrestrial Physics* 63.2, pp. 171–179. DOI: 10.1016/S1364-6826(00)00144-9.

Hall, C. M., T. Aso, M. Tsutsumi, J. Höffner, F. Sigernes, and D. A. Holdsworth (2006). "Neutral air temperatures at 90 km and 70°N and 78°N". In: *Journal of Geophysical Research: Atmospheres* 111.D14105. DOI: 10.1029/2005JD006794.

Hall, C. M., T. Aso, M. Tsutsumi, S. Nozawa, A. H. Manson, and C. E. Meek (2005a). "A comparison of mesosphere and lower thermosphere neutral winds as determined by meteor and medium-frequency radar at 70°N". In: *Radio Science* 40.4. DOI: 10.1029/2004RS003102.

Hall, C. M., T. Aso, M. Tsutsumi, S. Nozawa, A. H. Manson, and C. E. Meek (2005b). "Letter to the Editor: Testing the hypothesis of the influence of neutral turbulence on the deduction of ambipolar diffusivities from meteor trail expansion". In: *Annales Geophysicae* 23, pp. 1071–1073. DOI: 10.5194/angeo-23-1071-2005.

Hall, C. M., A. Brekke, A. H. Manson, C. E. Meek, and S. Nozawa (2007). "Trends in mesospheric turbulence at 70°N". In: *Atmospheric Science Letters* 8.3, pp. 80–84. DOI: 10.1002/asl.156.

Hall, C. M., A. H. Manson, and C. E. Meek (1998a). "Seasonal variation of the turbopause: One year of turbulence investigation at 69°N by the joint University of Tromsø/University of Saskatchewan MF radar". In: *Journal of Geophysical Research: Atmospheres* 103.D22, pp. 28769–28773. DOI: 10.1029/1998JD200002.

Hall, C. M., C. E. Meek, and A. H. Manson (1998b). "Turbulent energy dissipation rates from the University of Tromsø/University of Saskatchewan MF radar". In: *Journal of Atmospheric and Solar-Terrestrial Physics* 60.4, pp. 437–440. DOI: 10.1016/S1364-6826(97)00124-7.

Hall, C. M., C. E. Meek, A. H. Manson, and S. Nozawa (2008). "Turbopause determination, climatology, and climatic trends using medium frequency radars at 52°N and 70°N". In: *Journal of Geophysical Research: Atmospheres* 113.D13. DOI: 10.1029/2008JD009938.

Hall, C. M. and M. Tsutsumi (2013). "Changes in mesospheric dynamics at 78°N, 16°E and 70°N, 19°E: 2001–2012". In: *Journal of Geophysical Research: Atmospheres* 118.7, pp. 2689–2701. DOI: 10.1002/jgrd.50268.

Hargreaves, J. K. and A. Brekke (1981). "Application of the Ramfjordmoen partial reflection experiment to the study of auroral precipitation events". In: *Journal of Atmospheric and Terrestrial Physics* 43.10, pp. 1093–1106. DOI: 10.1016/0021-9169(81)90024-6.

Herzberg, G. (1950). *Molecular spectra and molecular structure. Vol 1: Spectra of diatomic molecules*. Second edition. Van Nostrand Reinhold, New York.

Hill, E. and J. H. Van Vleck (1928). "On the quantum mechanics of the rotational distortion of multiplets in molecular spectra". In: *Physical Review* 32 (2), pp. 250–272. DOI: 10.1103/PhysRev.32.250.

Hines, C. O. (1960). "Internal atmospheric gravity waves at ionospheric heights". In: *Canadian Journal of Physics* 38.11, pp. 1441–1481. DOI: 10.1139/p60-150.

Hocking, W. K. (1983). "On the extraction of atmospheric turbulence parameters from radar backscatter Doppler spectra—I. Theory". In: *Journal of Atmospheric and Terrestrial Physics* 45.2-3, pp. 89–102. DOI: 10.1016/S0021-9169(83)80013-0.

Hocking, W. K. (1985). "Measurement of turbulent energy dissipation rates in the middle atmosphere by radar techniques: A review". In: *Radio Science* 20.6, pp. 1403–1422. DOI: 10.1029/RS020i006p01403.

Hocking, W. K. (1987). "Turbulence in the region 80–120 km". In: *Advances in Space Research* 7.10, pp. 10171–10181. DOI: 10.1016/0273-1177(87)90090-1.

Hocking, W. K., T. Thayaparan, and J. Jones (1997). "Meteor decay times and their use in determining a diagnostic mesospheric temperature-pressure parameter: Methodology and one year of data". In: *Geophysical Research Letters* 24.23, pp. 2977–2980. DOI: 10.1029/97GL03048.

Hodges, R. R. (1967). "Generation of turbulence in the upper atmosphere by internal gravity waves". In: *Journal of Geophysical Research* 72.13, pp. 3455–3458. DOI: 10.1029/JZ072i013p03455.

Hoffmann, P., E. Becker, W. Singer, and M. Placke (2010). "Seasonal variation of mesospheric waves at northern middle and high latitudes". In: *Journal of Atmospheric and Solar-Terrestrial Physics* 72.14, pp. 1068–1079. DOI: 10.1016/j.jastp.2010.07.002.

Hoffmann, P., M. Rapp, W. Singer, and D. Keuer (2011). "Trends of mesospheric gravity waves at northern middle latitudes during summer". In: *Journal of Geophysical Research: Atmospheres* 116.D4. DOI: 10.1029/2011JD015717.

Hoffmann, P., W. Singer, D. Keuer, W. K. Hocking, M. Kunze, and Y. Murayama (2007). "Latitudinal and longitudinal variability of mesospheric

winds and temperatures during stratospheric warming events". In: *Journal of Atmospheric and Solar-Terrestrial Physics* 69.17, pp. 2355–2366. DOI: 10.1016/j.jastp.2007.06.010.

Holdsworth, D. A., R. J. Morris, D. J. Murphy, I. M. Reid, G. B. Burns, and W. J. R. French (2006). "Antarctic mesospheric temperature estimation using the Davis mesosphere-stratosphere-troposphere radar". In: *Journal of Geophysical Research: Atmospheres* 111.D5. DOI: 10.1029/2005JD006589.

Holton, J. R. (1983). "The influence of gravity wave breaking on the general circulation of the middle atmosphere". In: *Journal of the Atmospheric Sciences* 40.10, pp. 2497–2507. DOI: 10.1175/1520-0469(1983)040<2497:TIOGWB>2.0.CO;2.

Holton, J. R. (2004). *An introduction to dynamic meteorology*. Fourth edition. International geophysics series Vol. 1. Elsevier Academic press. ISBN: 9780123540157.

Holton, J. R. and R. S. Lindzen (1972). "An updated theory for the quasi-biennial cycle of the tropical stratosphere". In: *Journal of the Atmospheric Sciences* 29.6, pp. 1076–1080. DOI: 10.1175/1520-0469(1972)029<1076:AUTFTQ>2.0.CO;2.

Holton, J. R. and H.-C. Tan (1980). "The influence of the equatorial quasi-biennial oscillation on the global circulation at 50 mb". In: *Journal of the Atmospheric Sciences* 37.10, pp. 2200–2208. DOI: 10.1175/1520-0469(1980)037<2200:TIOTEQ>2.0.CO;2.

Hoppe, U.-P., C. Hall, and J. Röttger (1988). "First observations of summer polar mesospheric backscatter with a 224 MHz radar". In: *Geophysical Research letters* 15.1, pp. 28–31. DOI: 10.1029/GL015i001p00028.

Jones, J. (1975). "On the decay of underdense radio meteor echoes". In: *Monthly Notices of the Royal Astronomical Society* 173.3, pp. 637–647. DOI: 10.1093/mnras/173.3.637.

Kaiser, T. R. (1953). "Radio echo studies of meteor ionization". In: *Advances in Physics* 2.8, pp. 495–544. DOI: 10.1080/00018735300101282.

Kolmogorov, A. N. (1941). "The local structure of turbulence in incompressible viscous fluid for very large Reynolds numbers". In: *Doklady Akademiia Nauk SSSR* 30, pp. 299–303.

Kovalev, D. V., A. P. Smirnov, and Y. S. Dimant (2008). "Annales Geophysicae". In: 26.9, pp. 2853–2870. DOI: 10.5194/angeo-26-2853-2008.

Krassovsky, V. I., N. N. Shefov, and V. I. Yarin (1962). "Atlas of the airglow spectrum 3000–12400 Å". In: *Planetary and Space Science* 9.12, pp. 883–915. DOI: 10.1016/0032-0633(62)90008-9.

Kurihara, J., Y. Ogawa, S. Oyama, S. Nozawa, M. Tsutsumi, C. M. Hall, Y. Tomikawa, and R. Fujii (2010). "Links between a stratospheric sudden warming and thermal structures and dynamics in the high-latitude meso-

sphere, lower thermosphere, and ionosphere". In: *Geophysical Research Letters* 37.13. DOI: 10.1029/2010GL043643.

Labitzke, K. (1981). "Stratospheric-mesospheric midwinter disturbances: A summary of observed characteristics". In: *Journal of Geophysical Research: Oceans* 86.C10, pp. 9665–9678. DOI: 10.1029/JC086iC10p09665.

Labitzke, K. and B. Naujokat (2000). "The lower Arctic stratosphere in winter since 1952". In: *Sparc Newsletter* 15, pp. 11–14.

Lean, J. L. and A. Skumanich (1983). "Variability of the Lyman alpha flux with solar activity". In: *Journal of Geophysical Research: Space Physics* 88.A7, pp. 5751–5759. DOI: 10.1029/JA088iA07p05751.

Lehmacher, G. A., T. D. Scott, M. F. Larsen, S. G. Bilén, C. L. Croskey, J. D. Mitchell, M. Rapp, F.-J. Lübken, and R. L. Collins (2011). "The Turbopause experiment: atmospheric stability and turbulent structure spanning the turbopause altitude". In: *Annales Geophysicae* 29, pp. 2327–2339. DOI: 10.5194/angeo-29-2327-2011.

Lindzen, R. S. (1981). "Turbulence and stress owing to gravity wave and tidal breakdown". In: *Journal of Geophysical Research: Oceans* 86.C10, pp. 9707–9714. DOI: 10.1029/JC086iC10p09707.

Lindzen, R. S. and J. R. Holton (1968). "A theory of the quasi-biennial oscillation". In: *Journal of the Atmospheric Sciences* 25.6, pp. 1095–1107. DOI: 10.1175/1520-0469(1968)025<1095:ATOTQB>2.0.CO;2.

Liu, G. and G. G. Shepherd (2006). "An empirical model for the altitude of the OH nightglow emission". In: *Geophysical Research Letters* 33 (L09805). DOI: 10.1029/2005GL025297.

Liu, G., G. G. Shepherd, and R. G. Roble (2008). "Seasonal variations of the nighttime O(^{1}S) and OH airglow emission rates at mid-to-high latitudes in the context of the large-scale circulation". In: *Journal of Geophysical Research: Space Physics* 113.A06302. DOI: 10.1029/2007JA012854.

Lomb, N. R. (1976). "Least-squares frequency analysis of unequally spaced data". In: *Astrophysics and Space Science* 39.2, pp. 447–462. DOI: 10.1007/BF00648343.

Lübken, F.-J. (1999). "Thermal structure of the Arctic summer mesosphere". In: *Journal of Geophysical Research: Atmospheres* 104.D8, pp. 9135–9149. DOI: 10.1029/1999JD900076.

Lübken, F.-J. and U. von Zahn (1991). "Thermal structure of the mesopause region at polar latitudes". In: *Journal of Geophysical Research: Atmospheres* 96.D11, pp. 20841–20857. DOI: 10.1029/91JD02018.

Luo, Y., A. H. Manson, C. E. Meek, C. K. Meyer, M. D. Burrage, D. C. Fritts, C. M. Hall, W. K. Hocking, J. MacDougall, D. M. Riggin, and R. A. Vincent (2002). "The 16-day planetary waves: multi-MF radar observations from the arctic to equator and comparisons with the HRDI measurements

and the GSWM modelling results". In: *Annales Geophysicae* 20.5, pp. 691–709. DOI: 10.5194/angeo-20-691-2002.

Manabe, S. and R. T. Wetherald (1975). "The effect of doubling the CO_2 concentration on the climate of a general circulation model". In: *Journal of Atmospheric Sciences* 32.1, pp. 3–15. DOI: 10.1175/1520-0469(1975)032<0003:TEODTC>2.0.CO;2.

Manson, A. H. and C. E. Meek (1991). "Climatologies of mean winds and tides observed by medium frequency radars at Tromsö (70°N) and Saskatoon (52°N) during 1987–1989". In: *Canadian Journal of Physics* 69.8-9, pp. 966–975. DOI: 10.1139/p91-152.

Manson, A. H., C. E. Meek, A. Brekke, and J. Moen (1992). "Mesosphere and lower thermosphere (80–120 km) winds and tides from near Troms0 (70°N, 19°E): Comparisons between radars (MF, EISCAT, VHF) and rockets". In: *Journal of Atmospheric and Terrestrial Physics* 54.7, pp. 927–950. DOI: 10.1016/0021-9169(92)90059-T.

Manson, A. H., C. E. Meek, C. Hall, W. K. Hocking, J. MacDougall, S. Franke, K. Igarashi, D. Riggin, D. C. Fritts, and R. A. Vincent (1999). "Gravity wave spectra, directions and wave interactions: Global MLT-MFR network". In: *Earth, Planets and Space* 51.7–8, pp. 543–562. DOI: 10.1186/BF03353214.

Manson, A. H., C. E. Meek, T. L. Hansen, and T. Trondsen (1990a). "Dynamics of the upper middle atmosphere (80–110 km) at Tromsø (70°N) and Saskatoon (52°N), June–December 1987, using the Tromsø and Saskatoon MF radars". In: *Journal of Atmospheric and Terrestrial Physics* 52.10-11, pp. 971–980. DOI: 10.1016/0021-9169(90)90028-L.

Manson, A. H., C. E. Meek, R. Schminder, D. Kürschner, R. R. Clark, H. G. Müller, R. A. Vincent, A. Phillips, G. J. Fraser, W. Singer, and E. S. Kazimirovsky (1990b). "Tidal winds from the MLT global radar network during the first LTCS campaign—September 1987". In: *Journal of Atmospheric and Terrestrial Physics* 52.3, pp. 175–183. DOI: 10.1016/0021-9169(90)90121-3.

Matsuno, T. (1971). "A dynamical model of the stratospheric sudden warming". In: *Journal of the Atmospheric Sciences* 28.8, pp. 1479–1494. DOI: 10.1175/1520-0469(1971)028<1479:ADMOTS>2.0.CO;2.

McDade, I. C. (1991). "The altitude dependence of the OH ($X^2\,\Pi$) vibrational distribution in the nightglow: Some model expectations". In: *Planetary and Space Science* 39.7, pp. 1049–1057. DOI: 10.1016/0032-0633(91)90112-N.

McDaniel, E. W. and E. A. Mason (1973). *The mobility and diffusion of ions in gases*. John Wiley & Sons, Inc.

McKinley, D. W. R. (1961). *Meteor science and engineering*. McGraw-Hill, New York.

Meinel, A. B. (1950a). "OH emission bands in the spectrum of the night sky. I". In: *The Astrophysical Journal* 111, pp. 555–564. DOI: 10.1086/145296.

Meinel, A. B. (1950b). "OH emission bands in the spectrum of the night sky. II". In: *The Astrophysical Journal* 112, pp. 120–130. DOI: 10.1086/145321.

Mies, F. H. (1974). "Calculated vibrational transition probabilities of OH (X^2 Π)". In: *Journal of Molecular Spectroscopy* 53.2, pp. 150–188. DOI: 10.1016/0022-2852(74)90125-8.

Mulligan, F. J., M. E. Dyrland, F. Sigernes, and C. S. Deehr (2009). "Inferring hydroxyl layer peak heights from ground-based measurements of OH(6-2) band integrated emission rate at Longyearbyen (78°N, 16°E)". In: *Annales Geophysicae* 27.11, pp. 4197–4205. DOI: 10.5194/angeo-27-4197-2009.

Murgatroyd, R. J. and F. Singleton (1961). "Possible meridional circulations in the stratosphere and mesosphere". In: *Quarterly Journal of the Royal Meteorological Society* 87.372, pp. 125–135. DOI: 10.1002/qj.49708737202.

Myrabø, H. K. (1984). "Temperature variation at mesopause levels during winter solstice at 78°N". In: *Planetary and Space Science* 32.2, pp. 249–255. DOI: 10.1016/0032-0633(84)90159-4.

Myrabø, H. K. (1986). "Winter-season mesopause and lower thermosphere temperatures in the northern polar region". In: *Planetary and Space Science* 34.11, pp. 1023–1029. DOI: 10.1016/0032-0633(86)90012-7.

Myrabø, H. K., C. S. Deehr, and B. Lybekk (1984). "Polar cap OH airglow rotational temperatures at the mesopause during a stratospheric warming event". In: *Planetary and Space Science* 32.7, pp. 853–856. DOI: 10.1016/0032-0633(84)90009-6.

Newnham, D. A., P. J. Espy, M. A. Clilverd, C. J. Rodger, A. Seppälä, D. J. Maxfield, P. Hartogh, C. Straub, K. Holmén, and R. B. Horne (2013). "Observations of nitric oxide in the Antarctic middle atmosphere during recurrent geomagnetic storms". In: *Journal of Geophysical Research: Space Physics* 118.12, pp. 7874–7885. DOI: 10.1002/2013JA019056.

Noll, S., W. Kausch, S. Kimeswenger, S. Unterguggenberger, and A. M. Jones (2015). "OH populations and temperatures from simultaneous spectroscopic observations of 25 bands". In: *Atmospheric Chemistry and Physics* 15.7, pp. 3647–3669. DOI: 10.5194/acp-15-3647-2015.

Offermann, D., P. Hoffmann, P. Knieling, R. Koppmann, J. Oberheide, and W. Steinbrecht (2010). "Long-term trends and solar cycle variations of mesospheric temperature and dynamics". In: *Journal of Geophysical Research: Atmospheres* 115.D18. DOI: 10.1029/2009JD013363.

Offermann, D., M. Jarisch, H. Schmidt, J. Oberheide, K. U. Grossmann, O. Gusev, J. M. Russell III, and M. G. Mlynczak (2007). "The "wave

turbopause"". In: *Journal of Atmospheric and Solar-Terrestrial Physics* 69.17, pp. 2139–2158. DOI: 10.1016/j.jastp.2007.05.012.

Oliver, W. L., J. M. Holt, S.-R. Zhang, and L. P. Goncharenko (2014). "Long-term trends in thermospheric neutral temperature and density above Millstone Hill". In: *Journal of Geophysical Research: Space Physics* 119.9, pp. 7940–7946. DOI: 10.1002/2014JA020311.

Olivero, J. J. and G. E. Thomas (1986). "Climatology of polar mesospheric clouds". In: *Journal of the Atmospheric Sciences* 43.12, pp. 1263–1274. DOI: 10.1175/1520-0469(1986)043<1263:COPMC>2.0.CO;2.

Pendleton, W. R., P. J. Espy, and M. R. Hammond (1993). "Evidence for non-local-thermodynamic-equilibrium rotation in the OH nightglow". In: *Journal of Geophysical Research: Space Physics* 98.A7, pp. 11567–11579. DOI: 10.1029/93JA00740.

Picone, J. M., A. E. Hedin, D. P. Drob, and A. C. Aikin (2002). "NRLMSISE-00 empirical model of the atmosphere: Statistical comparisons and scientific issues". In: *Journal of Geophysical Research: Space Physics* 107.A12, SIA 15-1–SIA 15-16. DOI: 10.1029/2002JA009430.

Pierce, R. M. and S. E. Roark (2012). "Wind speed measurements of Doppler-shifted absorption lines using two-beam interferometry". In: *Applied Optics* 51.12, pp. 1853–1864. DOI: 10.1364/AO.51.001853.

Rapp, M. and F.-J. Lübken (2004). "Polar mesosphere summer echoes (PMSE): Review of observations and current understanding". In: *Atmospheric Chemistry and Physics* 4.11/12, pp. 2601–2633. DOI: 10.5194/acp-4-2601-2004.

Reynolds, O. (1894). "On the dynamical theory of incompressible viscous fluids and the determination of the criterion". In: *Proceedings of the Royal Society of London* 56, pp. 40–45. DOI: 10.1098/rspl.1894.0075.

Reynolds, W. C. (1987). "Fundamentals of turbulence for turbulence modeling and simulation". In: *Modern Theoretical and Experimental Approaches to Turbulent Flow Structure and its Modelling*.

Rienecker, M. M., M. J. Suarez, R. Gelaro, R. Todling, J. Bacmeister, E. Liu, M. G. Bosilovich, S. D. Schubert, L. Takacs, G.-K. Kim, S. Bloom, J. Chen, D. Collins, A. Conaty, A. Da Silva, W. Gu, J. Joiner, R. D. Koster, R. Lucchesi, A. Molod, T. Owens, S. Pawson, P. Pegion, C. R. Redder, R. Reichle, F. R. Robertson, A. G. Ruddick, M. Sienkiewicz, and J. Woollen (2011). "MERRA: NASA's modern-era retrospective analysis for research and applications". In: *Journal of Climate* 24.14, pp. 3624–3648. DOI: 10.1175/JCLI-D-11-00015.1.

Roble, R. G. and R. E. Dickinson (1989). "How will changes in carbon dioxide and methane modify the mean structure of the mesosphere and thermosphere?" In: *Geophysical Research Letters* 16.12, pp. 1441–1444. DOI: 10.1029/GL016i012p01441.

Rossby, C.-G. and collaborators (1939). "Relation between variations in the intensity of the zonal circulation of the atmosphere and the displacements of the semi-permanent centers of action". In: *Journal of Marine Research* 2.1, pp. 38–55.

Röttger, J., C. La Hoz, M. C. Kelley, U.-P. Hoppe, and C. Hall (1988). "The structure and dynamics of polar mesosphere summer echoes observed with the EISCAT 224 MHz radar". In: *Geophysical Research Letters* 15.12, pp. 1353–1356. DOI: 10.1029/GL015i012p01353.

Rubin, A. E. and J. N. Grossman (2010). "Meteorite and meteoroid: New comprehensive definitions". In: *Meteoritics & Planetary Science* 45.1, pp. 114–122. DOI: 10.1111/j.1945-5100.2009.01009.x.

Salby, M. L. (1981a). "Rossby normal modes in nonuniform background configurations. Part I: Simple fields". In: *Journal of the Atmospheric Sciences* 38.9, pp. 1803–1826. DOI: 10.1175/1520-0469(1981)038<1803:RNMINB>2.0.CO;2.

Salby, M. L. (1981b). "Rossby normal modes in nonuniform background configurations. Part II: Equinox and solstice conditions". In: *Journal of the Atmospheric Sciences* 38.9, pp. 1827–1840. DOI: 10.1175/1520-0469(1981)038<1827:RNMINB>2.0.CO;2.

Scargle, J. D. (1982). "Studies in astronomical time series analysis. II. Statistical aspects of spectral analysis of unevenly spaced data". In: *The Astrophysical Journal* 263, pp. 835–853. DOI: 10.1086/160554.

Scheer, J. and E. R. Reisin (2007). "Is there an influence of short-term solar activity variations on mesopause region airglow?" In: *Advances in Space Research* 39.8, pp. 1248–1255. DOI: 10.1016/j.asr.2007.01.002.

Schlegel, K., A. Brekke, and A. Haug (1978). "Some characteristics of the quiet polar D-region and mesosphere obtained with the partial reflection method". In: *Journal of Atmospheric and Terrestrial Physics* 40.2, pp. 205–213. DOI: 10.1016/0021-9169(78)90025-9.

Schmidt, H., G. P. Brasseur, M. Charron, E. Manzini, M. A. Giorgetta, T. Diehl, V. I. Fomichev, D. Kinnison, D. Marsh, and S. Walters (2006). "The HAMMONIA chemistry climate model: Sensitivity of the mesopause region to the 11-year solar cycle and CO_2 doubling". In: *Journal of Climate* 19.16, pp. 3903–3931. DOI: 10.1175/JCLI3829.1.

Schoeberl, M. R. and D. L. Hartmann (1991). "The dynamics of the stratospheric polar vortex and its relation to springtime ozone depletions". In: *Science* 251, pp. 46–52. DOI: 10.1126/science.251.4989.46.

She, C. Y. and D. A. Krueger (2004). "Impact of natural variability in the 11-year mesopause region temperature observation over Fort Collins, CO (41°N, 105°W)". In: *Advances in Space Research* 34.2, pp. 330–336. DOI: 10.1016/j.asr.2003.02.047.

Shepherd, G. G., G. Liu, and R. G. Roble (2005). "Large-scale circulation of atomic oxygen in the upper mesosphere and lower thermosphere". In: *Advances in Space Research* 35, pp. 1945–1950. DOI: 10.1016/j.asr.2004.12.036.

Shepherd, M. G., P. J. Espy, C. Y. She, W. Hocking, P. Keckhut, G. Gavrilyeva, G. G. Shepherd, and B. Naujokat (2002). "Springtime transition in upper mesospheric temperature in the northern hemisphere". In: *Journal of Atmospheric and Solar-Terrestrial Physics* 64.8, pp. 1183–1199. DOI: 10.1016/S1364-6826(02)00068-8.

Shine, K. P. (1987). "The middle atmosphere in the absence of dynamical heat fluxes". In: *Quarterly Journal of the Royal Meteorological Society* 113.476, pp. 603–633. DOI: 10.1002/qj.49711347610.

Shiotani, M. and I. Hirota (1985). "Planetary wave-mean flow interaction in the stratosphere: A comparison between northern and southern hemispheres". In: *Quarterly Journal of the Royal Meteorological Society* 111.468, pp. 309–334. DOI: 10.1002/qj.49711146804.

Sigernes, F., N. Shumilov, C. S. Deehr, K. P. Nielsen, T. Svenøe, and O. Havnes (2003). "Hydroxyl rotational temperature record from the auroral station in Adventdalen, Svalbard 78°N, 15°E)". In: *Journal of Geophysical Research: Space Physics* 108.A9. DOI: 10.1029/2001JA009023.

Singer, W., P. Hoffmann, A. H. Manson, C. E. Meek, R. Schminder, D. Kürschner, G. A. Kokin, A. K. Knyazev, Y. I. Portnyagin, N. A. Makarov, A. N. Fakhrutdinova, V. V. Sidorov, G. Cevolani, H. G. Muller, E. S. Kazimirovsky, V. A. Gaidukov, R. R. Clark, R. P. Chebotarev, and Y. Karadjaev (1994). "The wind regime of the mesosphere and lower thermosphere during the DYANA campaign—I. Prevailing winds". In: *Journal of Atmospheric and Terrestrial Physics* 56.13-14, pp. 1717–1729. DOI: 10.1016/0021-9169(94)90006-X.

Sivjee, G. G. (1992). "Airglow hydroxyl emissions". In: *Planetary and Space Science* 40.2-3, pp. 235–242. DOI: 10.1016/0032-0633(92)90061-R.

Sivjee, G. G. and R. M. Hamwey (1987). "Temperature and chemistry of the polar mesopause OH". In: *Journal of Geophysical Research: Space Physics* 92.A5, pp. 4663–4672. DOI: 10.1029/JA092iA05p04663.

Sivjee, G. G., R. L. Walterscheid, J. H. Hecht, R. M. Hamwey, G. Schubert, and A. B. Christensen (1987). "Effects of atmospheric disturbances on polar mesopause airglow OH emissions". In: *Journal of Geophysical Research: Space Physics* 92.A7, pp. 7651–7656. DOI: 10.1029/JA092iA07p07651.

Stray, N. H., R. J. de Wit, P. J. Espy, and R. E. Hibbins (2014). "Observational evidence for temporary planetary wave forcing of the MLT during fall equinox". In: *Geophysical Research Letters* 41.17, pp. 6281–6288. DOI: 10.1002/2014GL061119.

Thomas, R. J., C. A. Barth, G. J. Rottman, D. W. Rusch, G. H. Mount, G. M. Lawrence, R. W. Sanders, G. E. Thomas, and L. E. Clemens (1983). "Mesospheric ozone depletion during the solar proton event of July 13, 1982. Part I Measurement". In: *Geophysical Research Letters* 10.4, pp. 253–255. DOI: 10.1029/GL010i004p00253.

Tiao, G. C., G. C. Reinsel, D. Xu, J. H. Pedrick, X. Zhu, A. J. Miller, J. J. DeLuisi, C. L. Mateer, and D. J. Wuebbles (1990). "Effects of autocorrelation and temporal sampling schemes on estimates of trend and spatial correlation". In: *Journal of Geophysical Research: Atmospheres* 95.D12, pp. 20507–20517. DOI: 10.1029/JD095iD12p20507.

Turnbull, D. N. and R. P. Lowe (1989). "New hydroxyl transition probabilities and their importance in airglow studies". In: *Planetary and Space Science* 37.6, pp. 723–738. DOI: 10.1016/0032-0633(89)90042-1.

Viereck, R. A. and C. S. Deehr (1989). "On the interaction between gravity waves and the OH Meinel (6-2) and the O_2 atmospheric (0-1) bands in the polar night airglow". In: *Journal of Geophysical Research: Space Physics* 94.A5, pp. 5397–5404. DOI: 10.1029/JA094iA05p05397.

Von Savigny, C., I. C. McDade, K.-U. Eichmann, and J. P. Burrows (2012). "On the dependence of the OH* Meinel emission altitude on vibrational level: SCIAMACHY observations and model simulations". In: *Atmospheric Chemistry and Physics* 12.18, pp. 8813–8828. DOI: 10.5194/acp-12-8813-2012.

Walterscheid, R. L., G. G. Sivjee, and R. G. Roble (2000). "Mesospheric and lower thermospheric manifestations of a stratospheric warming event over Eureka, Canada (80°N)". In: *Geophysical Research Letters* 27.18, pp. 2897–2900. DOI: 10.1029/2000GL003768.

Walterscheid, R. L., G. G. Sivjee, G. Schubert, and R. M. Hamwey (1986). "Large-amplitude semidiurnal temperature variations in the polar mesopause: evidence of a pseudotide". In: *Nature* 324.6095, pp. 347–349. DOI: 10.1038/324347a0.

Warhaft, Zellman (1997). *An introduction to thermal-fluid engineering: The engine and the atmosphere*. Cambridge University Press.

Waters, J. W., L. Froidevaux, R. S. Harwood, R. F. Jarnot, H. M. Pickett, W. G. Read, P. H. Siegel, R. E. Cofield, M. J. Filipiak, D. A. Flower, et al. (2006). "The earth observing system microwave limb sounder (EOS MLS) on the Aura satellite". In: *IEEE Transactions on Geoscience and Remote Sensing* 44.5, pp. 1075–1092. DOI: 10.1109/TGRS.2006.873771.

Weatherhead, E. C., G. C. Reinsel, G. C. Tiao, X.-L. Meng, D. Choi, W.-K. Cheang, T. Keller, J. DeLuisi, D. J. Wuebbles, J. B. Kerr, A. J. Miller, S. J. Oltmans, and J. E. Frederick (1998). "Factors affecting the detection of trends: Statistical considerations and applications to environmental data".

In: *Journal of Geophysical Research* 103.D14, pp. 17–149. DOI: 10.1029/98JD00995.

Weinstock, J. (1978). "Vertical turbulent diffusion in a stably stratified fluid". In: *Journal of the Atmospheric Sciences* 35.6, pp. 1022–1027. DOI: 10.1175/1520-0469(1978)035<1022:VTDIAS>2.0.CO;2.

Yee, J.-H., G. Crowley, R. G. Roble, W. R. Skinner, M. D. Burrage, and P. B. Hays (1997). "Global simulations and observations of O(^1S), $O_2(^1\Sigma)$ and OH mesospheric nightglow emissions". In: *Journal of Geophysical Research* 102.A9, pp. 19949–19968. DOI: 10.1029/96JA01833.

Younger, J. P., C. S. Lee, I. M. Reid, R. A. Vincent, Y. H. Kim, and D. J. Murphy (2014). "The effects of deionization processes on meteor radar diffusion coefficients below 90 km". In: *Journal of Geophysical Research: Atmospheres* 119.16, pp. 10027–10043. DOI: 10.1002/2014JD021787.

A. Appendix

Figure A.1.: Map of part of the Arctic. Longyearbyen and Tromsø are marked in red. Image courtesy: Google Maps.

Figure A.2.: Map of Longyearbyen and surrounding areas. The locations of the old auroral station and the Kjell Henriksen Observatory are marked as black and red stars. Image courtesy: TopoSvalbard, Norwegian Polar Institute.

Figure A.3.: Map of Tromsø and surrounding areas. The location of Ramfjordmoen research station is marked as a black and red star. Image courtesy: Norgeskart, Norwegian Mapping Authority.

B. Papers

Paper 1

Mesospheric temperatures derived from three decades of hydroxyl airglow measurements from Longyearbyen, Svalbard (78°N)

Holmen, S. E., M. E. Dyrland and F. Sigernes

Published in Acta Geophysica, 62 (2), 302–315, doi: 10.2478/s11600-013-0159-4, 2013.

VERSITA

Acta Geophysica
DOI: 10.2478/s11600-013-0159-4

Mesospheric Temperatures Derived from Three Decades of Hydroxyl Airglow Measurements from Longyearbyen, Svalbard (78°N)

Silje E. HOLMEN[1,2,3], Margit E. DYRLAND[1,2], and Fred SIGERNES[1,2]

[1]The University Centre in Svalbard, Longyearbyen, Norway
e-mails: siljeh@unis.no (corresponding author), margitd@unis.no, freds@unis.no

[2]Birkeland Centre for Space Science, Bergen, Norway

[3]University of Tromsø – The Arctic University of Norway,
Tromsø Geophysical Observatory, Tromsø, Norway

A b s t r a c t

The airglow hydroxyl temperature record from Longyearbyen, Svalbard, is updated with data from the last seven seasons (2005/2006-2011/2012). The temperatures are derived from ground-based spectral measurements of the hydroxyl airglow layer, which ranges from 76 to 90 km height. The overall daily average mesospheric temperature for the whole temperature record is 206 K. This is by 3 K less than what Dyrland and Sigernes (2007) reported in their last update on the temperature series. This temperature difference is due to cold winter seasons from 2008 to 2010. 2009/2010 was the coldest winter season ever recorded over Longyearbyen, with a seasonal average of 185 K. Temperature variability within the winter seasons is investigated, and the temperature difference between late December (local minimum) and late January (local maximum) is approximately 8 K.

Key words: airglow, mesosphere, Arctic, temperature, hydroxyl.

1. INTRODUCTION

The mesosphere and lower thermosphere (MLT) region is a part of the atmosphere characterized by strong variability in winter temperatures. Break-

ing of tidal, planetary and gravity waves in the MLT region controls the large-scale circulation and hence actuates vertical motion leading to adiabatic heating/cooling (Becker 2012). The dynamic connections between wave activity and temperature variability are particularly obvious during sudden stratospheric warmings (SSWs). In major SSW events, the polar vortex breaks down and the zonal-mean zonal winds reverse from westerly to easterly, and the stratosphere warms by up to 60 K very rapidly (Matsuno 1971, Walterscheid *et al.* 2000, Cho *et al.* 2004, Liu and Roble 2002). SSWs are confirmed through several studies to have a strong impact on fluctuations in the mesospheric airglow layers and hence mesospheric temperatures (Walterscheid *et al.* 1994). Solar flux variability is also believed to have an influence on the thermodynamics of the mesosphere, but the relationship between mesospheric temperature and the 27-day and 11-year solar cycles is still not fully understood (Beig *et al.* 2012, Matthes *et al.* 2004).

The ground-based spectral measurement of hydroxyl (OH) airglow from Longyearbyen, Svalbard, started in 1980. The derived rotational temperature series is one of the longest continuous winter records in the world. Sigernes *et al.* (2003) and Dyrland and Sigernes (2007) have earlier reported on trends and features in the temperature series from Longyearbyen. Also other studies have been carried out on the OH* temperatures from Longyearbyen, with focus mainly on tidal and seasonal variations and the influence of SSWs and gravity waves (Myrabø 1984, Nielsen *et al.* 2002, Dyrland *et al.* 2010). Myrabø (1986) reported to have identified a seasonal pattern in winter with relatively low temperatures in late December followed by higher temperatures in January. Diurnal and semi-diurnal variations in the dataset have also been analysed, with results varying from a 13 K semi-diurnal amplitude found (Walterscheid *et al.* 1986) to no considerable periods identified (Dyrland and Sigernes 2007).

This study, with the supplement of OH* airglow derived temperatures from the last seven winter seasons, gives an update on the mesospheric winter temperature series from Longyearbyen, Svalbard. The OH* airglow temperatures are presented and discussed in connection with SSWs and wave activity. The spectral measurement technique is described in Section 2. The results are presented and discussed in Section 3. Section 4 is a summary of the results.

2. DATA AND MEASUREMENT TECHNIQUE

In this study, OH*(6-2) airglow rotational temperatures are derived from the 1 m focal length Ebert–Fastie spectrometer located in Longyearbyen. The temperatures are weighted averages from the height range of the vibrational state of OH*(6-2). According to Mulligan *et al.* (2009), the peak altitude of

the OH layer ranges from 76 to 90 km. The observing season is from the beginning of November to the end of February.

The Ebert–Fastie spectrometer was placed in the Auroral Station in Adventdalen (78°N, 15°E) in 1983, but it was moved to the new station, the Kjell Henriksen Observatory (KHO) on the mountain Breinosa (78°N, 16°E) in 2007. The distance between the two sites is approximately 8 km. The field of view of the instrument is 5 degrees in the zenith direction. The cone angle is slightly larger in the direction parallel to the entrance slit. At 90 km altitude the latter corresponds to a measurement area of $\sim 9 \times 12$ km. The move of the instrument should therefore have no impact on the comparability of the time series when it comes to the measurement area. However, the local weather conditions above the two different sites and contamination by artificial light sources may be slightly different. The potential impact on the derived temperatures will be discussed further in Section 3.1.

The rotational temperatures are derived from the measured spectra by calculating synthetic spectra as a function of instrumental bandpass and temperature. Then the background is detected by finding the optimal fit between the measured and synthetic spectra. The temperatures are derived from the slope of a linear fit to a Boltzmann plot using $P_1(2)$, $P_1(3)$, $P_1(4)$, and $P_1(5)$ rotational line intensities of the OH*(6-2) band. Energy term values are taken from Krassovsky *et al.* (1962), and Einstein coefficients are from Mies (1974). The basis for the calculation of the spectra is given by Herzberg (1950).

Some of the spectra are contaminated by aurora or by scattering of moonlight by clouds. To sort out contaminated spectra, the covariance between synthetic and measured spectra is calculated. A poor fit between the measured and the synthetic spectra is either caused by a very high background intensity or by occurrence of the auroral OI 8446 Å emission line, which is located close to the $P_2(4)$ line of the OH*(6-2) band. The fit variance of P_1 and P_2 is also calculated for every spectrum in order to ensure local thermal equilibrium. Spectra with covariance between measured and synthetic spectra less than 0.8 are discarded. This is also the case for spectra with P_1 fit variance greater than 0.05 and P_2 fit variance greater than 0.3. For further details on the instrument and the temperature retrieval method, see Sigernes *et al.* (2003) and Dyrland and Sigernes (2007). An example of a synthetic fit to an hourly averaged measured spectrum from 7 January 2012 at 19 UTC is shown in Fig. 1.

Viereck and Deehr (1989) considered the above method to have an uncertainty of approximately ± 5 K for 15 minute average temperature retrievals. For the more recent data the uncertainties have been calculated for each hourly averaged spectra from the error in the least squares fit of the Boltzmann plot. The error in the daily averaged temperature has been calculated

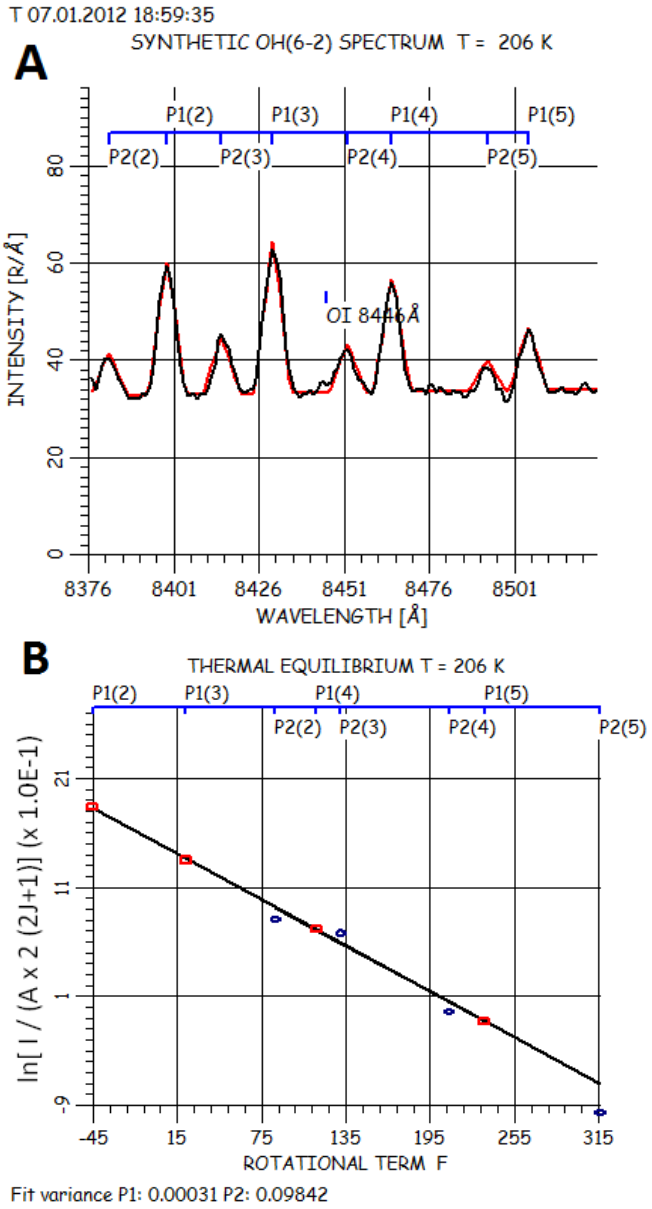

Fig. 1. Panel A shows the synthetic fit to an hourly averaged measured spectrum from 7 January 2012 at 19 UTC. The red curve is the measured spectrum, and the black curve is the synthetic, fitted spectrum. During this hour there was no contamination of the averaged spectrum due to the auroral OI 8446 Å emission line, as can be seen from the very good fit between the two curves. Panel B shows the corresponding Boltzmann plot to the spectrum in panel A. The straight line is the linear fit using P_1 and P_2 values. A spread of the P_2 values from the linear fit would indicate a departure from thermal equilibrium. For this particular spectrum the covariance, P_1 fit variance and P_2 fit variance were 0.99, 0.0003, and 0.1, respectively. Colour version of this figure is available in electronic edition only.

by weighting the hourly averaged temperatures according to their individual uncertainty following the method of Bevington and Robinson (1992). The errors of the daily averaged temperatures range between 0.2-5 K.

3. RESULTS AND DISCUSSION

3.1 Seasons 2005/2006-2011/2012

In Fig. 2 daily averaged temperatures retrieved from the OH* airglow layer over Longyearbyen are presented. Daily averages of temperatures are estimated for days with three or more hours of data that satisfy the covariance and fit variance criteria mentioned in Section 2. Together with the OH* temperatures, 10 hPa stratospheric temperature is plotted. The 10 hPa temperature is a NASA reanalysis temperature provided through the Modern-Era Retrospective analysis for Research and Applications (MERRA) project (NASA 2012).

From Fig. 2 we see that the data coverage over the seven winter seasons analysed is variable, but especially the 2010/2011 and 2011/2012 winters have very good data coverage. The reason is partly that the photomultiplier tube (PMT) of the instrument was changed in January 2011, providing a better signal-to-noise ratio that allowed more spectra to be analysed, and partly the varying weather conditions of the different seasons. The move of the in-

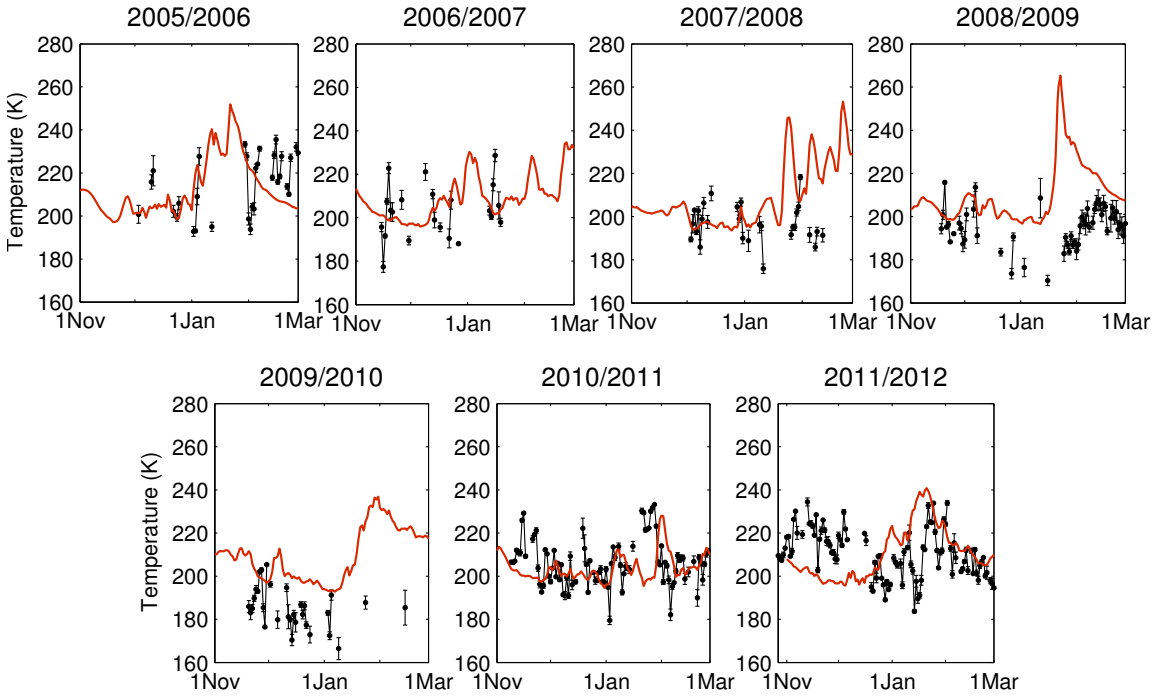

Fig. 2. Daily averaged temperatures retrieved from OH*(6-2) airglow emissions over Longyearbyen, Svalbard, for the winter seasons of 2005/2006 through 2011/2012. The OH* temperatures are plotted as black bullets with ± 1 standard deviation indicated as errorbars. The 10 hPa stratospheric MERRA temperatures are plotted as red lines. The OH* temperatures are weighted averages from 76 to 90 km, while the 10 hPa MERRA temperatures are at about 30 km in the stratosphere and vary by a few km depending on the synoptic meteorological conditions. Colour version of this figure is available in electronic edition only.

strument itself in 2007 may also have contributed to an increase in data points. Contamination from artificial light from the town is much less at the KHO compared to the old Auroral Station because of the larger distance to the town. In addition, there is significantly less light contamination from snowmobiles and cars. No official cloud cover statistics for the two sites exists, so it is hard to draw categorical conclusions about the local differences. It is however possible that there may be some local differences in cloud cover that would bring a bias to the temperatures, but this difference is here assumed to be small.

The seven seasons reported here appear to some extent to agree with a hypothesis that some SSWs are preceded by a cooling seen in OH* temperatures a few days earlier, which is reported earlier in literature (Hoffmann *et al.* 2007, Walterscheid *et al.* 2000). We see that an increase in stratospheric temperature (red line) sometimes succeeds a decrease in OH* temperatures, but this is hard to confirm to a full extent because of the lack of data for some periods.

It must be noted that a change in OH* temperature may be due to either a temperature change in the height distribution of OH*(6-2), a change in the height distribution itself, or a combination of both (Baker and Stair 1988, Mulligan *et al.* 2009).

The average temperature, standard deviation and maximum and minimum temperatures of all seven seasons are listed in Table 1. We see that the standard deviation in general is higher in January compared to December. A reason for this may be a higher occurrence of SSWs and planetary wave activity in late winter (January–March) (Labitzke and Naujokat 2000, Kuttippurath and Nikulin 2012), which again is a source of high variability in OH* temperatures.

Table 1

Average, maximum, and minimum temperatures, including standard deviations, for seasons 2005/2006 through 2011/2012

Winter season	Number of days	Mean *T* Nov-Feb [K]	Mean *T* Dec [K]	Mean *T* Jan [K]	Max *T* [K]	Min *T* [K]
2005/2006	31	215 ± 13	208 ± 8	211 ± 17	236	193
2006/2007	22	203 ± 12	202 ± 11	208 ± 11	229	177
2007/2008	28	197 ± 9	199 ± 7	196 ± 10	218	176
2008/2009	54	195 ± 9	193 ± 12	187 ± 10	216	170
2009/2010	30	185 ± 9	182 ± 7	180 ± 9	205	166
2010/2011	93	206 ± 11	201 ± 7	212 ± 13	233	180
2011/2012	103	211 ± 11	207 ± 12	210 ± 13	234	184

Note: In addition to the average over the whole winter season from November through February, the average for December and January is listed.

Occasionally, the OH* temperatures increase very rapidly over a relatively short time period. This is especially noticeable in January 2012, when the temperature increases by approximately 50 K in just a couple of days. This takes place during a minor SSW. These kind of fluctuations in the OH* airglow are most likely due to propagation and breaking of planetary and gravity waves in the mesosphere, as reported in literature (Sivjee *et al.* 1987, Hoffmann *et al.* 2007).

3.2 The updated temperature series 1983-2012

In Fig. 3 annual averaged airglow temperatures from the 1983/1984 through the 2011/2012 seasons are presented. Only seasons with ten or more daily averaged temperatures calculated have been included in the plot. The seasonal average is the average of December and January temperatures. Missing values for the 1990/1991, 1991/1992, 1992/1993, 1993/1994, 1996/1997, and 1998/1999 seasons can either be explained by too few temperatures retrieved or by instrument problems.

The average temperature for the whole temperature series is 206 K, when using Einstein coefficients from Mies (1974). This is by 3 K less than what was found in the previous work done on the time series by Dyrland and Sigernes (2007) on the period from 1983 to 2005. The maximum temperature of the temperature record is 253 K (19 February 2004) and the minimum temperature is 166 K (9 January 2010). We see from Fig. 2 that some of the latest years analysed are quite cold years, especially the 2008/2009 and the 2009/2010 seasons. This is in accordance with recent publications from other

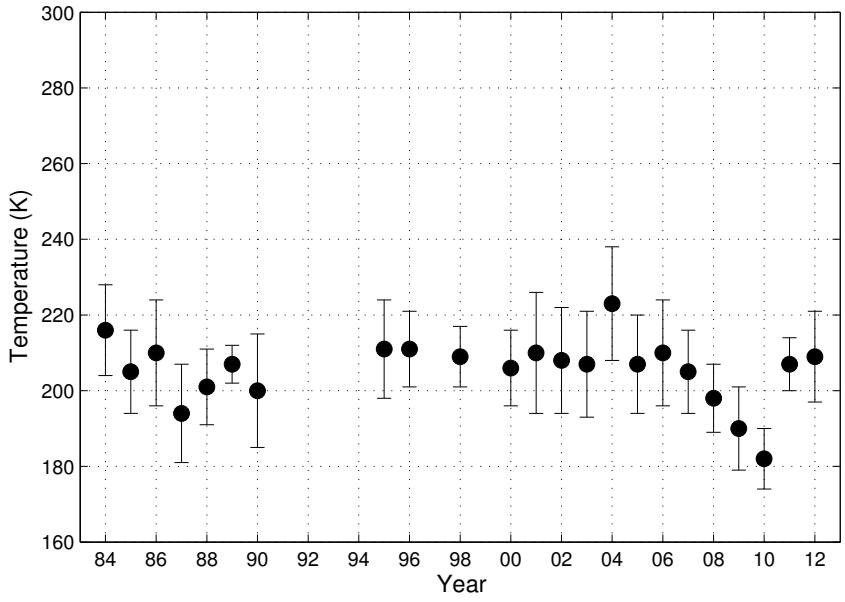

Fig. 3. Seasonal averages of OH* rotational temperatures from Longyearbyen, Svalbard, 1983-2012, plotted as black bullets with the standard deviation as errorbars.

locations (French and Klekociuk 2011, Offermann *et al.* 2010). This may partly be explained by that during the last decade, an increasing number of SSWs have been detected compared to the 1990s. Kuttippurath and Nikulin (2012) investigated the major SSWs in the Arctic observed between 2003/2004 and 2009/2010, and found that the SSW in the 2008/2009 season was the strongest. Even though the stratosphere was relatively cold in the first part of the 2009/2010 winter season, this season experienced the largest momentum flux of all seasons. This took place in the end of January and beginning of February.

Temperature variations within the winter season were examined by superposing all OH* temperatures by day of year and then applying a 5-day running mean on the superposed temperatures. This is the same method as that described in French and Klekociuk (2011) and Azeem *et al.* (2007). The superposed temperatures are shown in Fig. 4. The black lines represent ± 1 standard deviation, the red line represents the 5-day running mean, and the blue line represents a 15-day running mean. We see from the lines representing running means that there are some variations in temperature within the winter season. There are local temperature maxima in late January and in February, while there is a local minimum in the end of December / beginning of February. The local temperature minimum in late December / early January is consistent with what Myrabø (1986) found for the winter seasons in the first part of the 1980s in Longyearbyen. The temperature difference between late December and late January is approximately 8 K when looking at

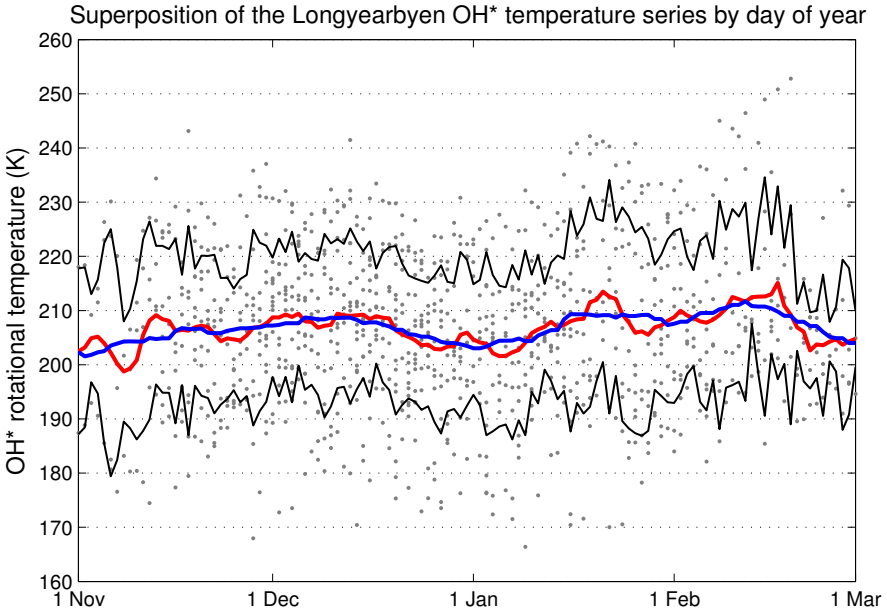

Fig. 4. Superposition of the Longearbyen OH* temperatures by day of year. Grey dots are the daily averaged OH* temperatures, and the black lines represent ± 1 SD. The red line is the 5-day running mean, and the blue line is the 15-day running mean. Colour version of this figure is available in electronic edition only.

the 5-day running mean. This is in accordance with the climatology Hall *et al.* (2012) reported for Svalbard using temperatures from the Nippon / Norway Svalbard Meteor Radar (NSMR) located in Adventdalen near Longyearbyen.

As mentioned for Fig. 2, the OH* temperatures used in Fig. 4 may be influenced not only by the temperature change within the height range, but also by a change in height of the OH* layer.

The overall standard deviation of the Longyearbyen hydroxyl temperature record is 15 K. This is higher than the standard deviations estimated for other locations (*e.g.*, French and Klekociuk 2011, Bittner *et al.* 2002). The reason for this is not completely clear, but one explanation may be that the mountainous topography in Svalbard favours gravity wave formation and thus great variability in temperatures. However, when looking at two high-latitude stations in Antarctica, the Davis and the Amundsen–Scott South Pole stations, these also experience substantial gravity wave activity (Beldon and Mitchell 2009, Collins *et al.* 1994). This occurs even though the standard deviations are reported to be significantly lower than for Longyearbyen. An explanation for some of the variability in temperatures may be the weather regimes. Especially the South Pole station is rarely hit by heavy storms, which are characteristic for Antarctic coastal areas. Also, there are in general less clouds above this station compared to over Longyearbyen (Town *et al.* 2007, eKlima 2012). Longyearbyen is frequently hit by strong low pressure systems, which makes the weather during the winter season unstable. This may result in higher standard deviations.

Mies was the first to calculate Einstein coefficients for hydroxyl vibration-rotation bands in 1974 (Mies 1974). Since then, several updates have been published in order to improve temperature estimates, *e.g.*, Turnbull and Lowe (1989), Goldman *et al.* (1998), and Van der Loo and Groenenboom (2007). Even though more recent updates on the Einstein coefficients exist, the coefficients from Mies (1974) were used in this study. This was done in order to compare the temperatures obtained from the seven winter seasons analysed with the temperatures obtained from 1983 to 2005. The use of different Einstein coefficients is considered to have a significant impact on the estimated temperatures. Perminov *et al.* (2007) state that the use of different Einstein coefficients may give differences in temperatures as high as 5-14 K. Several studies have been carried out during the last decade to determine which Einstein coefficients give the most accurate temperatures, and there is no general agreement about this matter (French *et al.* 2000, Pendleton and Taylor 2002, Cosby and Slanger 2007). It is important to have this in mind when looking at the absolute temperatures.

An updated trend of the Longyearbyen temperature record is not presented in this paper. A thorough analysis and discussion about the trend with

regard to seasonal variations and solar cycle dependence will be published in a future paper.

4. CONCLUSIONS

The OH*(6-2) airglow temperature record from Longyearbyen, Svalbard (78°N, 16°E) is updated with data from the winter seasons of 2005/2006 through 2011/2012. The data coverage of these seven seasons is variable, but the 2010/2011 and 2011/2012 seasons have excellent data coverage. We see that a decrease in OH* temperatures is to some extent followed by an increase in stratospheric temperatures during SSW events.

The variability in airglow temperatures over Longyearbyen is very high, both on a day-to-day basis and within a season. In some periods, OH* temperatures can increase or decrease by 30-50 K in just a couple of days. The standard deviations of each season range from 9 to 13 K. This is significantly higher than standard deviations reported from other locations. The reason for this is not fully understood, but one explanation may be that the topography around Longyearbyen favours gravity wave activity, which again is a known contributor to variability in mesospheric temperatures. Also weather systems in the Arctic, and thus unstable observing conditions, may explain temperature variability.

When looking at the whole temperature record from 1983 to 2012, the overall average temperature is 206 K, by 3 K less than what Dyrland and Sigernes (2007) reported for their update on the temperature record. It is noticeable that some of the most recent winter seasons were very cold. Especially the 2009/2010 season was cold, with a seasonal average of 185 K and a daily averaged minimum of 166 K measured on 9 January 2010. This is the lowest daily temperature of the whole temperature record. The low temperatures for the years 2008-2010 are in accordance with temperatures reported from other locations and with the fact that strong SSWs took place during that time.

There are monthly temperature variations within the winter season. The data show local temperature maxima in late January and in February, while there is a local minimum in the end of December / beginning of February. The temperature difference between late December and late January is approximately 8 K.

Acknowledgments. This work was financially supported by The Research Council of Norway through the projects named: Norwegian and Russian Upper Atmosphere Co-operation On Svalbard part 2 # 196173 / S30 (NORUSCA2), Infrastructure for Space Physics Related Research on Svalbard # 195385 (INFRASPACE) and High-Arctic Gravity waves and their impact on middle atmospheric circulation and temperature (# 204993).

References

Azeem, S.M.I., G.G. Sivjee, Y.-I. Won, and C. Mutiso (2007), Solar cycle signature and secular long-term trend in OH airglow temperature observations at South Pole, Antarctica, *J. Geophys. Res.* **112**, A1, A01305, DOI: 10.1029/2005JA011475.

Baker, D.J., and A.T. Stair Jr. (1988), Rocket measurements of the altitude distributions of the hydroxyl airglow, *Phys. Scr.* **37**, 4, 611, DOI: 10.1088/0031-8949/37/4/021.

Becker, E. (2012), Dynamical control of the middle atmosphere, *Space Sci. Rev.* **168**, 1-4, 283-314, DOI: 10.1007/s11214-011-9841-5.

Beig, G., S. Fadnavis, H. Schmidt, and G.P. Brasseur (2012), Inter-comparison of 11-year solar cycle response in mesospheric ozone and temperature obtained by HALOE satellite data and HAMMONIA model, *J. Geophys. Res.* **117**, D4, D00P10, DOI: 10.1029/2011JD015697.

Beldon, C.L., and N.J. Mitchell (2009), Gravity waves in the mesopause region observed by meteor radar. 2: Climatologies of gravity waves in the Antarctic and Arctic, *J. Atmos. Solar-Terr. Phys*. **71**, 8-9, 875-884, DOI: 10.1016/j.jastp.2009.03.009.

Bevington, P.R., and D.K. Robinson (1992), *Data Reduction and Error Analysis for the Physical Sciences*, McGraw-Hill, New York, 328 pp.

Bittner, M., D. Offermann, H.-H. Graef, M. Donner, and K. Hamilton (2002), An 18-year time series of OH rotational temperatures and middle atmosphere decadal variations, *J. Atmos. Solar-Terr. Phys*. **64**, 8-11, 1147-1166, DOI: 10.1016/S1364-6826(02)00065-2.

Cho, Y.-M., G.G. Shepherd, Y.-I. Won, S. Sargoytchev, S. Brown, and B. Solheim (2004), MLT cooling during stratospheric warming events, *Geophys. Res. Lett.* **31**, 10, L10104, DOI: 10.1029/2004GL019552.

Collins, R.L., A. Nomura, and C.S. Gardner (1994), Gravity waves in the upper mesosphere over Antarctica: Lidar observations at the South Pole and Syowa, *J. Geophys. Res.* **99**, D3, 5475-5485, DOI: 10.1029/93JD03276.

Cosby, P.C., and T.G. Slanger (2007), OH spectroscopy and chemistry investigated with astronomical sky spectra, *Can. J. Phys*. **85**, 2, 77-99, DOI: 10.1139/p06-088.

Dyrland, M.E., and F. Sigernes (2007), An update on the hydroxyl airglow temperature record from the Auroral Station in Adventdalen, Svalbard (1980-2005), *Can. J. Phys*. **85**, 2, 143-151, DOI: 10.1139/p07-040.

Dyrland, M.E., F.J. Mulligan, C.M. Hall, F. Sigernes, M. Tsutsumi, and C.S. Deehr (2010), Response of OH airglow temperatures to neutral air dynamics at 78°N, 16°E during the anomalous 2003-2004 winter, *J. Geophys. Res.* **115**, D7, D07103, DOI: 10.1029/2009JD012726.

eKlima (2012), Norwegian Meteorological Institute's climate database, http://eklima.met.no/, accessed November 2012.

French, W.J.R., and A.R. Klekociuk (2011), Long-term trends in Antarctic winter hydroxyl temperatures, *J. Geophys. Res.* **116**, D4, D00P09, DOI: 10.1029/2011JD015731.

French, W.J.R, G.B. Burns, K. Finlayson, P.A. Greet, R.P. Lowe, and P.F.B. Williams (2000), Hydroxyl (6-2) airglow emission intensity ratios for rotational temperature determination, *Ann. Geophys*. **18**, 10, 1293-1303, DOI: 10.1007/s00585-000-1293-2.

Goldman, A., W.G. Schoenfeld, D. Goorvitch, C. Chackerian Jr., H. Dothe, F. Mélen, M.C. Abrams, and J.E.A. Selby (1998), Updated line parameters for OH $X^2\Pi$-$X^2\Pi$ (v″,v′) transitions, *J. Quant. Spectrosc. Radiat. Transfer* **59**, 3-5, 453-469, DOI: 10.1016/S0022-4073(97)00112-X.

Hall, C.M., M.E. Dyrland, M. Tsutsumi, and F.J. Mulligan (2012), Temperature trends at 90 km over Svalbard, Norway (78°N 16°E), seen in one decade of meteor radar observations, *J. Geophys. Res.* **117**, D8, D08104, DOI: 10.1029/2011JD017028.

Herzberg, G. (1950), *Molecular Spectra and Molecular Structure. Vol. I. Spectra of Diatomic Molecules*, Van Nostrand Company Inc., New York.

Hoffmann, P., W. Singer, D. Keuer, W.K. Hocking, M. Kunze, and Y. Murayama (2007), Latitudinal and longitudinal variability of mesospheric winds and temperatures during stratospheric warming events, *J. Atmos. Solar-Terr. Phys*. **69**, 17-18, 2355-2366, DOI: 10.1016/j.jastp.2007.06.010.

Krassovsky, V.I., N.N. Shefov, and V.I. Yarin (1962), Atlas of the airglow spectrum 3000-12 400 Å, *Planet. Space Sci*. **9**, 12, 883-915, DOI: 10.1016/0032-0633(62)90008-9.

Kuttippurath, J., and G. Nikulin (2012), A comparative study of the major sudden stratospheric warmings in the Arctic winters 2003/2004-2009/2010, *Atmos. Chem. Phys*. **12**, 17, 8115-8129, DOI: 10.5194/acp-12-8115-2012.

Labitzke, K., and B. Naujokat (2000), The lower Arctic stratosphere in winter since 1952, *SPARC Newsletter* **15**, 11-14.

Liu, H.-L, and R.G. Roble (2002), A study of a self-generated stratospheric sudden warming and its mesospheric-lower thermospheric impacts using the coupled TIME-GCM/CCM3, *J. Geophys. Res.* **107**, D23, 4695, DOI: 10.1029/2001JD001533.

Matsuno, T. (1971), A dynamical model of the stratospheric sudden warming, *J. Atmos. Sci.* **28**, 8, 1479-1494, DOI: 10.1175/1520-0469(1971)028<1479:ADMOTS>2.0.CO;2.

Matthes, K., U. Langematz, L.L. Gray, K. Kodera, and K. Labitzke (2004), Improved 11-year solar signal in the Freie Universität Berlin Climate Middle Atmosphere Model (FUB-CMAM), *J. Geophys. Res.* **109**, D6, D06101, DOI: 10.1029/2003JD004012.

Mies, F.H. (1974), Calculated vibrational transition probabilities of OH($X^2\Pi$), *J. Mol. Spectrosc.* **53**, 2, 150-188, DOI: 10.1016/0022-2852(74)90125-8.

Mulligan, F.J., M.E. Dyrland, F. Sigernes, and C.S. Deehr (2009), Inferring hydroxyl layer peak heights from ground-based measurements of OH(6-2) band integrated emission rate at Longyearbyen (78°N, 16°E), *Ann. Geophys.* **27**, 11, 4197-4205, DOI: 10.5194/angeo-27-4197-2009.

Myrabø, H.K. (1984), Temperature variation at mesopause levels during winter solstice at 78°N, *Planet. Space Sci.* **32**, 2, 249-255, DOI: 10.1016/0032-0633(84)90159-4.

Myrabø, H.K. (1986), Winter-season mesopause and lower thermosphere temperatures in the northern polar region, *Planet. Space Sci*. **34**, 11, 1023-1029, DOI: 10.1016/0032-0633(86) 90012-7.

NASA (2012), Annual Meteorological Statistics, National Aeronautics Space Administration, http://acdb-ext.gsfc.nasa.gov/Data_services/met/ann_data.html, accessed October 2012.

Nielsen, K.P., F. Sigernes, E. Raustein, and C.S. Deehr (2002), The 20-year change of the Svalbard OH-temperatures, *Phys. Chem. Earth* **27**, 6-8, 555-561, DOI: 10.1016/S1474-7065(02)00037-2.

Offermann, D., P. Hoffmann, P. Knieling, R. Koppmann, J. Oberheide, and W. Steinbrecht (2010), Long-term trends and solar cycle variations of mesospheric temperature and dynamics, *J. Geophys. Res.* **115**, D18, D18127, DOI: 10.1029/2009JD013363.

Pendleton Jr., W.R., and M.J. Taylor (2002), The impact of *L*-uncoupling on Einstein coefficients for the OH Meinel (6,2) band: implications for *Q*-branch rotational temperatures, *J. Atmos. Solar-Terr. Phys*. **64**, 8-11, 971-983, DOI: 10.1016/S1364-6826(02)00051-2.

Perminov, V.I., A.I. Semenov, and N.N. Shefov (2007), On rotational temperature of the hydroxyl emission, *Geomag. Aeron*. **47**, 6, 756-763, DOI: 10.1134/S0016793207060084.

Sigernes, F., N. Shumilov, C.S. Deehr, K.P. Nielsen, T. Svenøe, and O. Havnes (2003), Hydroxyl rotational temperature record from the auroral station in Adventdalen, Svalbard (78°N, 15°E), *J. Geophys. Res.* **108**, A9, 1342, DOI: 10.1029/2001JA009023.

Sivjee, G.G., R.L. Walterscheid, J.H. Hecht, R.M. Hamwey, G. Schubert, and A.B. Christensen (1987), Effects of atmospheric disturbances on polar mesopause airglow OH emissions, *J. Geophys. Res.* **92**, A7, 7651-7656, DOI: 10.1029/JA092iA07p07651.

Town, M.S., V.P. Walden, and S.G. Warren (2007), Cloud cover over the South Pole from visual observations, satellite retrievals, and surface-based infrared radiation measurements, *J. Climate* **20**, 3, 544-559, DOI: 10.1175/JCLI4005.1.

Turnbull, D.N., and R.P. Lowe (1989), New hydroxyl transition probabilities and their importance in airglow studies, *Planet. Space Sci*. **37**, 6, 723-738, DOI: 10.1016/0032-0633(89)90042-1.

Van der Loo, M.P., and G.C. Groenenboom (2007), Theoretical transition probabilities for the OH Meinel system, *J. Chem. Phys*. **126**, 11, 114314-1-114314-7, DOI: 10.1063/1.2646859.

Viereck, R.A., and C.S. Deehr (1989), On the interaction between gravity waves and the OH Meinel (6-2) and the O_2 atmospheric (0-1) bands in the polar night airglow, *J. Geophys. Res*. **94**, A5, 5397-5404, DOI: 10.1029/JA094iA05p05397.

Walterscheid, R.L., G.G. Sivjee, G. Schubert, and R.M. Hamwey (1986), Large-amplitude semidiurnal temperature variations in the polar mesopause: evidence of a pseudotide, *Nature* **324**, 7445, 347-349, DOI: 10.1038/324347a0.

Walterscheid, R.L., G. Schubert, and M.P. Hickey (1994), Comparison of theories for gravity wave induced fluctuations in airglow emissions, *J. Geophys. Res*. **99**, A3, 3935-3944, DOI: 10.1029/93JA03312.

Walterscheid, R.L., G.G. Sivjee, and R.G. Roble (2000), Mesospheric and lower thermospheric manifestations of a stratospheric warming event over Eureka, Canada (80°N), *Geophys. Res. Lett*. **27**, 18, 2897-2900, DOI: 10.1029/2000GL003768.

Received 23 November 2012
Received in revised form 20 March 2013
Accepted 18 April 2013

Paper 2

Long-term trends and the effect of solar cycle variations on mesospheric winter temperatures over Longyearbyen, Svalbard (78°N)

Holmen, S. E., M. E. Dyrland and F. Sigernes

Published in Journal of Geophysical Research: Atmospheres, 119, 6596–6608, doi: 10.1002/2013JD021195, 2014.

AGU PUBLICATIONS

JGR

Journal of Geophysical Research: Atmospheres

RESEARCH ARTICLE
10.1002/2013JD021195

Key Points:
- Svalbard airglow temperatures are adjusted for seasonal and solar variations
- The solar response coefficient is 3.6 K/100 SFU with an uncertainty of 4.0 K
- The long-term mesospheric temperature trend is a near-zero trend

Correspondence to:
S. E. Holmen,
siljeh@unis.no

Citation:
Holmen, S. E., M. E. Dyrland, and F. Sigernes (2014), Long-term trends and the effect of solar cycle variations on mesospheric winter temperatures over Longyearbyen, Svalbard (78°N), *J. Geophys. Res. Atmos.*, *119*, 6596–6608, doi:10.1002/2013JD021195.

Received 13 NOV 2013
Accepted 23 MAY 2014
Accepted article online 27 MAY 2014
Published online 13 JUN 2014

Long-term trends and the effect of solar cycle variations on mesospheric winter temperatures over Longyearbyen, Svalbard (78°N)

Silje E. Holmen[1,2,3], Margit E. Dyrland[1,2], and Fred Sigernes[1,2]

[1]University Centre in Svalbard, Longyearbyen, Norway, [2]Birkeland Centre for Space Science, Bergen, Norway, [3]UiT—Arctic University of Norway, Tromsø Geophysical Observatory, Tromsø, Norway

Abstract This paper gives an update on the long-term trend in hydroxyl (OH*) airglow winter temperatures measured by a 1 m Ebert-Fastie spectrometer in Longyearbyen, Svalbard (78°N, 16°E), from 1983 to 2013. The temperatures are derived through synthetic fits of measured airglow spectra of the OH*(6-2) vibrational state. The data set is corrected for seasonal variations by subtracting the mean climatology. Also, solar cycle dependence is investigated. A solar response coefficient of 3.6 K ± 4.0 K/100 solar flux units (SFU) is calculated from F10.7 cm solar radio flux data. After subtraction of the climatology and solar response, the remaining long-term trend is a near-zero trend, −0.2 K ± 0.5 K/decade. Trend analysis of monthly temperatures indicates positive trends for November, January, and February and a negative trend for December, but the uncertainties are high.

1. Introduction

For many years, great attention has been given to the ongoing change in the Earth's climate. Most studies have focused on the climate change in the lower atmosphere [e.g., *Dickinson and Cicerone*, 1986; *Brasseur and Hitchman*, 1988], but during the last decades attention regarding climate change issues has also been drawn toward the middle and upper atmosphere. Model studies report that global warming at the Earth's surface has its counterpart in cooling of the stratosphere and mesosphere due to global increase of CO_2 and other greenhouse gases [*Akmaev and Fomichev*, 1998, 2000]. In this part of the atmosphere, greenhouse gases absorb energy and radiate it back to space, which leads to cooling. Some studies indicate that temperature change takes place first in the mesosphere and lower thermosphere (MLT region) and later propagates downward [*Hoffmann et al.*, 2007]. More sophisticated generations of models show that a doubled CO_2 concentration in the atmosphere indicates a cooling in the atmosphere everywhere above the tropopause. However, the smallest values of cooling occur around the mesopause [*Schmidt et al.*, 2006]. These results make temperature trends and variations in the MLT region important to investigate further.

The MLT region is characterized by strong variability in winter temperatures. This is among others due to planetary and gravity wave activity and Sudden Stratospheric Warmings (SSW), which are coupling processes between the lower, middle, and upper atmosphere [*Funke et al.*, 2010]. Solar flux variability is also believed to have an influence on variability of mesospheric temperatures, but how much influence is not fully agreed upon [*Beig et al.*, 2008; 2012; *Huang and Brasseur*, 1993; *Schmidt and Brasseur*, 2006].

The hydroxyl airglow temperature series from Longyearbyen, Svalbard, is one of the longest continuous measurement records of hydroxyl (OH*) winter temperatures in the world. *Sigernes et al.* [2003] and *Dyrland and Sigernes* [2007] have earlier reported on trends and features of the temperature series from Longyearbyen. *Sigernes et al.* [2003] reported a close to zero trend for the period 1983 to 2001: +0.6 K ± 2.0 K/decade. *Dyrland and Sigernes* [2007] reported a slightly positive trend from the period 1983 to 2005: +2.0 K ± 1.0 K/decade.

This study, with the supplement of OH* airglow temperatures from the last eight winter seasons, gives an update on the mesospheric temperature trend above Longyearbyen, Svalbard. In section 2, we describe the instrument, the temperature retrieval method, and the calibration procedure. In section 3, trends are presented and discussed with regard to seasonal variations and solar cycle variability. A summary of the results is presented in section 4.

Table 1. Number of Data Points in Each Winter Season From 1983/84 to 2012/13[a]

1983/84	42	1993/94*	6	2003/04	85
1984/85	42	1994/95	15	2004/05	27
1985/86	48	1995/96	23	2005/06	31
1986/87	40	1996/97*	1	2006/07	22
1987/88	66	1997/98	35	2007/08	28
1988/89*	5	1998/99*	3	2008/09	54
1989/90	58	1999/00	47	2009/10	30
1990/91*	9	2000/01	57	2010/11	93
1991/92*	–	2001/02	29	2011/12	103
1992/93*	–	2002/03	35	2012/13	91

[a]Seasons with less than 10 days of retrieved data are noted with *. These seasons are excluded from the trend analysis.

2. Instrumentation and Data

2.1. Data and Measurement Technique

Measurements of OH* airglow intensities in Longyearbyen on a regular basis date back to 1980. Then OH* rotational temperatures were obtained from the OH*(8-3) band using a ½ m focal length Ebert-Fastie spectrometer. To gain spectral resolution, the instrument was replaced with a 1 m Ebert-Fastie spectrometer in 1983, scanning the P branch of the OH*(6-2) band. Temperatures derived from the airglow intensities are weighted averages from the height range of the vibrational state of OH*(6-2). The observing season is from the beginning of November to the end of February, and temperatures are retrieved as long as the Sun is more than 12° below the horizon. The spectrometer scans one spectrum every 25 s. Daily averaged temperatures are estimated for days with 3 or more hours of retrieved data. Seasonal averages are estimated for seasons with 10 or more days of retrieved data. The number of data points in each season contributing to the means is listed in Table 1.

The rotational temperatures were derived from hourly averaged measured spectra by calculating synthetic spectra as a function of instrumental band pass and temperature. The typical instrumental band pass is 5 Å. The background was detected by finding the optimal fit between the measured and synthetic spectra. The temperatures were derived from the slope of a linear fit to a Boltzmann plot using $P_1(2)$, $P_1(3)$, $P_1(4)$, and $P_1(5)$ rotational line intensities of the OH*(6-2) band. Also, the corresponding P_2 lines ($P_2(3)$, $P_2(4)$, and $P_2(5)$) were ensured to follow the same linear fit, although their intensities were not used for temperature retrieval. Using rotational temperatures to represent neutral air temperatures requires an assumption of local thermodynamical equilibrium (LTE) with the environment. Initially, the hydrogen-ozone reaction produces OH* in highly excited rotational states which are not in LTE, but through collisions the lower vibrational and rotational states can be thermalized. Given the collisional frequency and radiative lifetime the OH*($v = 6$) state is considered to have undergone enough collisions to conform to a Boltzmann distribution [*Sivjee and Hamwey*, 1987] and that the OH*(6-2) vibrational-rotational band can been considered in quasi-LTE, meaning rotational states with rotational quantum number < 6 follow the Boltzmann distribution, but higher levels do not [*Pendleton et al.*, 1993]. Following this, our choice to include the $P_1(N = 2)$ to $P_1(N = 5)$ lines in our analysis is validated. The conclusion that the OH*(6-2) band is thermalized has been questioned quite recently by *Cosby and Slanger* [2007] who found that rotational temperatures derived from low rotational line intensities show a strong dependence on vibrational level, with higher temperatures for higher vibrational levels. This difference in temperature is only partly explained by the fact that different vibrational levels have their peak emissions at different altitudes [*von Savigny et al.*, 2012]. The interpretation of OH* temperatures as absolute neutral air temperatures is therefore questionable, especially for higher rotational-vibrational levels, and we therefore limit our analysis to spectra that follow the Boltzmann distribution and that can be considered in quasi-LTE. To ensure this, we employ certain criteria for selection of good spectra which are described below.

Covariance between hourly averaged measured and synthetic spectra was calculated to remove spectra that were contaminated by aurora, which occur frequently at 78°N. Spectra with a very high background due to scattering of moonlight or artificial light by clouds were also filtered out. Spectra with a covariance between the measured and synthetic spectra less than 0.8 were discarded. In addition, the fit variance for P_1 and P_2 was calculated for every spectrum to ensure that the different rotational lines follow the Boltzmann distribution and thus are in (quasi) LTE with the environment. Spectra with P_1 fit variance greater than 0.05 and P_2 fit

variance greater than 0.3 were omitted from further analysis. These criteria for selecting good spectra have been chosen based on experience and consistency for the whole data set. Depending on the weather conditions and auroral activity of each winter, the fraction of hourly averaged spectra that are discarded from further analyses ranges between 50% and 88%.

Uncertainties were calculated for each hourly averaged spectrum from the error in the least-squares fit to the Boltzmann plot. The error in the daily averaged temperatures was calculated by weighting the hourly averaged temperatures according to their individual uncertainty [*Bevington and Robinson*, 1992]. The error of the daily averaged temperatures ranges between 0.2 and 5 K. A more detailed description of the instrument and the temperature retrieval method can be found in *Sigernes et al*. [2003].

The temperature retrieval of the whole Longyearbyen OH* temperature record was done using Einstein coefficients from *Mies* [1974]. Using different Einstein coefficients has been demonstrated to have a significant impact on estimated temperatures [e.g., *Perminov et al*., 2007], but since this paper concerns a trend assessment and relative variations within a temperature series, the choice of transition probabilities does not affect the result as long as the same set is used for the entire data set.

From 1980 to 2007, OH* airglow measurements were done at the Auroral Station in Adventdalen (78°N, 15°E), but in 2007 the spectrometer was moved to the new observatory, the Kjell Henriksen Observatory (KHO) (78°N, 16°E). The distance between the two sites is approximately 8 km. The instrument's field of view is approximately 5 degrees in the zenith direction. The cone angle is slightly larger in the direction parallel to the entrance slit. At 90 km altitude, this corresponds to an area of measurement of ~9 × 12 km. Differences in local weather conditions between the two sites are small [*Holmen et al*., 2014]; thus, there should be no geophysical reasons why the change of location has influenced the measured temperatures. Also, analysis of the spectral background shows that it did not change significantly after 2007. Thus, the moving of the spectrometer is considered to have no impact on the comparability of the OH* measurement series.

2.2. Calibration

The wavelengths measured by a spectrometer will drift slightly with time and environmental conditions. To ensure the accuracy of the measurements, periodic calibrations must be conducted. Sensitivity calibrations of the 1 m Ebert-Fastie spectrometer conducted in 1980, 2002, and 2004 are presented in *Sigernes et al*. [2003] and *Dyrland and Sigernes* [2007]. Calibrations have been performed yearly since 2007. *Dyrland and Sigernes* [2007] concluded that the instrument had been operating stably with no overall degradation in sensitivity from 1983 to 2004.

Operating a spectrometer stably over time is a continuous battle of upgrading software and electronics, including detector and counting circuit. The spectrometer has for instance changed operating system five times during its lifetime. This involves change of counter cards, high voltage supplies, pulse amplifier/discriminator (PAD), photomultiplier tube (PMT), and cooler. This will all affect the performance of the instrument. Fine tuning of mirror, grating, and slit position is also important for optical performance. Therefore, we conduct sensitivity calibrations yearly. Note that the optical and mechanical elements of the instrument have never been replaced.

The main components in the calibration of the spectrometer are a Lambertian diffusive screen (SRT-99-180, Spectralon®, Labsphere Inc.) and a lamp. The lamp acts as a point source to the screen, and the screen is the actual source of the calibration.

The spectral radiance of the screen is given by:

$$B(\lambda) = \rho(\lambda) \times M_0(\lambda) \times \left(\frac{z_0}{z}\right)^2 \times \cos\ \alpha \qquad \left[\frac{R}{\text{Å}}\right]$$

where $\rho(\lambda)$ is the reflectance factor of the Lambertian surface and is nearly constant throughout the near-infrared region of the spectrum ($\rho(\lambda) \approx 0.98$). z is the distance between the center of the screen and the lamp, and α is the angle between the Lambertian screen and the lamp axis. $M_0(\lambda)$ is the known irradiance of the lamp in Rayleigh per Ångström [R/Å], initially obtained at a distance z_0. The lamp irradiance certification is in units of mW/m^{-2}nm, but is converted to number of photons cm^{-2} s^{-1} sr^{-1} and multiplied by $4\pi \times 10^{-6}$ to obtain the unit R/Å [*Sigernes et al*., 2007, 2012].

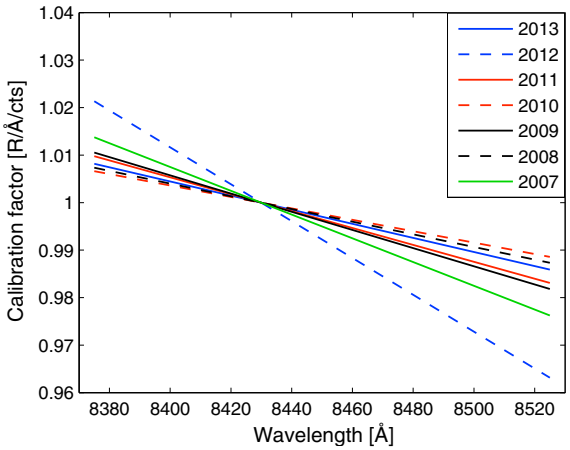

Figure 1. Spectrometer calibration factors for calibrations conducted from 2007 to 2013. Calibrations conducted from 2008 to 2013 were performed outdoors at the Kjell Henriksen Observatory (KHO) using a 200 W tungsten lamp. The 2007 calibration was conducted indoors in the optical lab at The University Centre in Svalbard, using a 45 W lamp.

The calibration factor of the instrument is given by:

$$K(\lambda) = \frac{B(\lambda)}{B(\lambda)} \qquad \left[\frac{R}{\text{Å}}/Cts\right]$$

where $C(\lambda)$ is the raw counts of the instrument produced by the illuminated screen. Calibration factors for calibrations performed from 2007 to 2013, normalized at the $P_1(3)$ line, are shown in Figure 1. The 2007 calibration was conducted indoors in the optical lab at The University Centre in Svalbard, without taking the plexiglass dome into account. A 45 W lamp (Oriel SN7-1633) was used. Since 2008, calibrations have been conducted outdoors at the KHO, using a 200 W tungsten lamp (Oriel SN7-1859).

Variation within the wavelength region from 8375 to 8525 Å and corresponding temperature uncertainties for the years 2007 to 2013 are shown in Table 2. Note that the spectral slopes of the calibration factors in the wavelength region are nearly constant through the years. It is a change in slope of the calibration factors that is important to the retrieval of the temperatures. The variation is within 4%, except for 2012, when the spectral slope was 5.3%. The reason for the higher variation in 2012 is not clear but could be weather related. The spectral slope of the calibration factors retrieved before and after the move of the instrument in 2007 did not change significantly. Temperature uncertainty as a consequence of the spectral slope was found by multiplying the calibration factors to synthetic spectra with constant background and zero slope, generated with temperatures ranging from 180 to 260 K. The temperatures derived from the spectra give an estimate of the temperature uncertainty due to the spectral slope. Temperature uncertainties range from 1 to 6 K. The absolute values of the calibration factors at 8430 Å ($P_1(3)$ line) are also listed in Table 2. The absolute value of the calibration factor varies by a factor of ~2 between 2009 and the latter years, and a factor of ~4 from that found by *Dyrland and Sigernes* [2007] for the earlier years.

It must be emphasized that our yearly calibration is a secondary calibration. The 200 W Tungsten lamp used for calibration outdoors is certified by comparing to our NIST (National Institute of Standards and Technology) traceable lamp source located in the calibration lab of The University Centre in Svalbard. Even though we have improved the secondary lamp housing to be more weather resistant and use lasers to measure distance, the outside temperature and wind conditions still affect the calibration outcome. A change in effective temperature is easily seen in the current running through the filament of the lamp. Snow and ice conditions near the instrument dome may also affect the setup of the Lambertian surface and the angle measurements. The above uncertainties are the main reasons for change in the level of the calibration factors in Table 2. Based on that the spectral slopes of the calibration factors are nearly constant through the years, we conclude that temperature measurements by the spectrometer are reliable for the time period 1983 to 2013.

Table 2. Calibration Output[a]

	Spectral Slope	Temperature Uncertainty	Absolute Value, 8430 Å
2013	2.4%	1–3 K	0.89
2012	5.3%	3–6 K	1.08
2011	2.9%	2–4 K	0.92
2010	1.6%	1–2 K	1.11
2009	1.5%	1–2 K	1.94
2008	1.7%	1–2 K	1.19
2007	3.7%	1–3 K	1.14

[a]Variation over the wavelength region 8375–8525 Å for years 2007 to 2013. The corresponding temperature uncertainties caused by the spectral slopes are also listed, together with the absolute values of the calibration factors at 8430 Å ($P_1(3)$ line).

The above procedure is our standard way of conducting secondary sensitivity calibrations of the Ebert-Fastie spectrometer. An improved method could be to use a portable low-light source and to monthly calibrate the instrument indoors, under its dome, reducing weather effects and logistics.

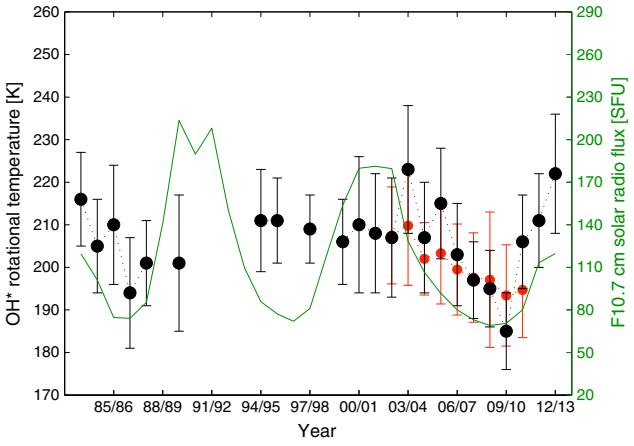

Figure 2. Seasonal averages of OH* temperatures before correction for seasonality and solar response. Seasonal averages are averages from November through February. Standard deviations are plotted as errorbars. Meteor radar temperatures at 90 km (November–February averages) from the NSMR radar in Longyearbyen are plotted as red bullets with standard deviations as errorbars. Variation of F10.7 cm solar radio flux during the same period is plotted as a green line.

3. Results and Discussion

There are many variables that can influence OH* temperatures. Sources of temperature variability are the mean meridional flow, planetary wave activity, solar flux variability, tides, gravity waves, and chemical processes like ozone depletion [*French and Klekociuk*, 2011; *Beig et al*., 2003]. These processes result in variations in OH* airglow temperatures on time scales ranging from minutes to decades. Also, variations in derived OH* temperatures may be influenced by changes in the altitude of the OH* layer. When investigating the long-term trend of a mesospheric temperature series, the goal is to identify factors influencing the natural variability and subtract their effects from the data set.

Uncorrected, seasonal averages of all winters in the Longyearbyen hydroxyl airglow temperature series are plotted in Figure 2 and reveal that there were some cold winter seasons in the period from 2008 to 2010. Temperatures retrieved from meteor trail echoes at 90 km altitude from the Nippon/Norway Svalbard Meteor Radar (NSMR) located in Adventdalen near Longyearbyen show a decrease in the same time period. Figure 2 shows that the meteor radar temperatures follow the variations in the airglow temperatures reasonably well, even though the magnitude of the variations is smaller. A period of lower temperatures around 2008 to 2010 can also be recognized in data from the Davis station in Antarctica, though not of the same magnitude [*French and Klekociuk*, 2011]. The solar activity was at a minimum during that time and the solar minimum around 2008 was the weakest solar minimum in nearly 100 years [*Ahluwalia and Jackiewicz*, 2011]. OH* temperatures are correlated reasonably well with solar activity over the most recent solar minimum. It is hard to see the same coincident pattern over the solar minimum around 1996. The temperature over the 1989/1990 winter is at odds with the solar maximum during that period, and temperatures around 1999 to 2003 do not appear to increase with the 2001 solar maximum. Reasons for this will be discussed in section 3.3.

In section 3.1, we explain how the mean climatology is removed from the time series to subtract the effect of seasonal variations from the data set. In section 3.2, solar cycle dependence is investigated. In section 3.3, the new and updated long-term trend is presented and discussed in terms of sources of temperature variability and changes in the altitude of the OH* layer. The trend is also compared with the previous trend update and trends from other sites. Monthly trends are evaluated in section 3.4.

3.1. Subtraction of Climatology

The seasonal variation is largely a result of the mean meridional flow. The method described in *French and Klekociuk* [2011] and *Azeem et al*. [2007] was used to subtract effects of seasonal variations from the data set. First, the time series was superposed by day of year, and daily averages for the same day of year were calculated. Then a 5-day running mean of these daily averages was applied. The running mean values obtained were then considered to be the mean winter climatology. To remove the effects of seasonal variations from the temperature record, the mean climatology for each day of year was subtracted from each daily temperature in the data set. The superposed temperatures with the 5 day running mean are shown in Figure 3. A more detailed description of the seasonal variations in the Longyearbyen OH* temperature data set can be found in *Holmen et al*. [2014].

Seasonal averages of the residual temperatures were estimated as the mean of daily averaged temperatures measured from November through February. Earlier trend estimates on the temperature record have used

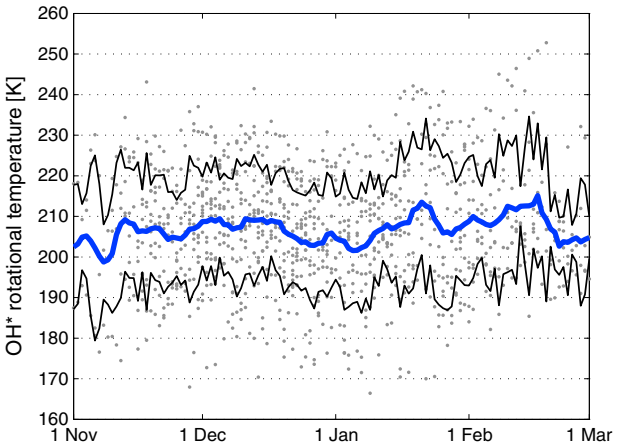

Figure 3. Superposition of the Longyearbyen OH* temperatures by day of year. Grey dots are the daily averaged OH* temperatures and the black lines represent ± 1 standard deviation. The blue line is the 5-day running mean.

the average of December and January as the seasonal average, but since the temperatures are now corrected for seasonal variations we choose to include the whole data set.

3.2. Solar Cycle Dependence

According to most recent studies on mesospheric long-term trend assessments, solar activity is believed to have an effect on mesospheric temperatures [e.g., *Azeem et al.*, 2007; *Offermann et al.*, 2010]. To subtract the effect from the data set we must know the level of influence. When it comes to irradiance and appearance, several measures of solar variation exist. In this paper, three different measures have been used to investigate solar dependence on OH* temperatures: The 11 year sunspot cycle (SSN), the F10.7 cm solar radio flux and total solar irradiance (TSI). The 11-year solar cycle is the periodic variation of the number of sunspots on the Sun. Records of the daily sunspot number are freely available from Solar Influences Data Analysis Center (SIDC). The F10.7 cm solar flux is a measure of the solar radio flux per unit frequency at a wavelength of 10.7 cm, near the peak of the observed solar radio emission. The global daily value of this index is measured at local noon at the Penticton Radio Observatory in Canada, and it has been measured daily since 1947. It is freely available on the webpage of National Geophysical Data Center (NGDC), a part of the National Oceanic and Atmospheric Administration (NOAA). The total solar irradiance is the spatially and spectrally integrated solar radiation incident at the top of the Earth's atmosphere. The time series used is the Active Cavity Radiometer Irradiance Monitor (ACRIM) composite, available at the ACRIM web page.

A solar response coefficient can be defined as how many Kelvin of the measured mesospheric temperatures that are accredited variability in solar activity. This coefficient can be estimated by the linear fit to a scatterplot of OH* residual temperatures against the different measures of solar activity. The slope of the linear fit is the solar response coefficient. Solar forcing, correlations, and 95% confidence limits for all three measures of solar activity

Table 3. Solar Forcing[a]

	Pearson's *r*	Solar Forcing	95% Confidence Intervals
F10.7 cm			
Daily average	0.12*	3.7 K ± 0.9 K/100 SFU	+1.9 K < S < +5.5 K
Monthly average	0.21^	4.4 K ± 2.4 K/100 SFU	−0.3 K < S < +9.1 K
Monthly average minus SSW	0.25^	5.1 K ± 2.7 K/100 SFU	−0.4 K < S < +10.6 K
Seasonal average	0.20	3.6 K ± 4.0 K/100 SFU	−4.7 K < S < +11.9 K
Total solar irradiance (TSI)			
Daily average	0.15*	3.7 K ± 0.8 K/Wm^{-2}	+2.2 K < S < +5.2 K
Monthly average	0.27*	4.8 K ± 2.1 K/Wm^{-2}	+0.7 K < S < +8.9 K
Monthly average minus SSW	0.32*	6.5 K ± 2.6 K/Wm^{-2}	+1.2 K < S < +11.9 K
Seasonal average	0.29	4.5 K ± 3.2 K/Wm^{-2}	−2.5 K < S < +10.8 K
Sunspot cycle			
Daily average	0.11*	3.3 K ± 0.9 K/100 spots	+1.5 K < S < +5.0 K
Monthly average	0.20^	4.5 K ± 2.5 K/100 spots	−0.4 K < S < +9.4 K
Monthly average minus SSW	0.17	3.6 K ± 2.8 K/100 spots	−2.0 K < S < +9.1 K
Seasonal average	0.20	4.0 K ± 4.3 K/100 spots	−4.9 K < S < +12.9 K

[a]Correlations, solar forcing coefficients, and 95% confidence limits calculated for three different measures of solar activity against the seasonally corrected OH* residuals. The solar forcing coefficients for the seasonal averages are computed using multivariate regression. Note the different units on the solar forcing coefficients. *: correlation at better than 95% significance. ^: correlation at better than 90% significance.

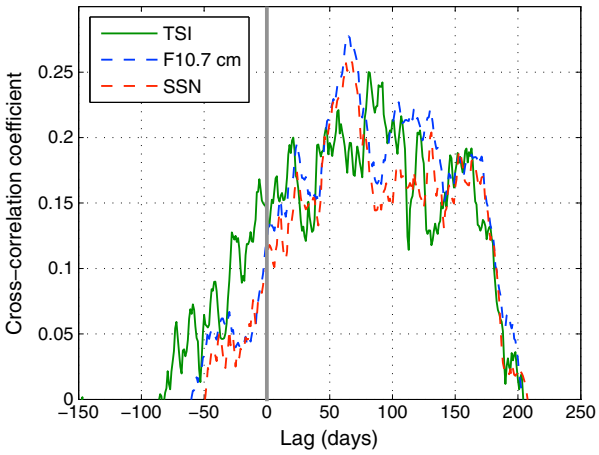

Figure 4. Lag-correlation analysis of daily averaged temperature residuals with corresponding daily values of total solar irradiance (TSI), F10.7 cm solar radio flux, and the sunspot number.

are listed in Table 3. The temperature residuals were averaged over a monthly and seasonal time scale. By averaging over a monthly time scale, the effect of planetary wave variability is reduced. SSWs are events caused by planetary waves and may last for several weeks. Since these events apparently have a significant influence on mesospheric temperatures [*Hoffmann et al.*, 2007], months where SSWs were present were excluded to see if that made any difference. SSW periods were identified using reanalysis temperatures and winds provided through the Modern-Era Retrospective analysis for Research and Applications (MERRA) project, available as annual meteorological statistics at the NASA webpage.

The highest correlation was achieved for the OH* residuals against the TSI but only slightly better than for the F10.7 cm solar flux and SSN. It is hard to say why the correlation was highest between TSI and the temperature residuals. Correlation between SSN and the OH* residuals may be biased by that even though the number of sunspots may be zero for many days in a row, the OH* temperatures still vary. The correlations are overall lower than correlations achieved for some other high-latitude sites [*Azeem et al.*, 2007; *French and Klekociuk*, 2011]. The correlation increases slightly when excluding SSW months, except for SSN. By eliminating SSW months, we are left with a data set that is dynamically quieter. This is not representative for average conditions. Therefore, we do not exclude SSW periods in further analyses.

There may be a phase difference between solar input and solar response. This can affect the magnitude of the solar response coefficient [*Wynn and Wickwar*, 2009; *French and Klekociuk*, 2011]. A cross-correlation analysis was performed to check if the correlation improved when a time lag was applied to the data sets. Lag correlation of the daily residuals with daily TSI, F10.7 cm solar flux and SSN is shown in Figure 4. Peak correlation for the association of TSI and temperature occurs at a lag of ~80 days. The correlation coefficients between the residuals and both F10.7 and SSN peaks at where the solar activity measures lead the temperature by ~65 days. At this point, F10.7 correlation ($r = 0.28$) exceeds both SSN and TSI correlation. By applying a 65 day lag between the daily residuals and the corresponding F10.7 data, the solar response coefficient becomes 8.8 K ± 0.9 K/100 solar flux units (SFU). This is a significantly higher response than at zero lag. By applying the same time lag to the monthly averaged residuals and F10.7, the solar response is 6.4 K ± 2.3 K/100 SFU, also higher than at zero lag.

French and Klekociuk [2011] found a time lag between solar input and OH* temperature response of ~160 days. *Shapiro et al.* [2012] found highest correlations between tropical mesospheric OH* and Lyman-α irradiance at about zero time lag. The zero time lag was justified by the short lifetime of OH*. According to *Wynn and Wickwar* [2009], it is reasonable to have phase lags between the solar input and the atmospheric response of up to several years at 90 km height. It is hard to find a plausible explanation for why the correlations are higher at lags of ~65 and ~80 days. Since we do not have continuous airglow measurements for all days or months in the winter seasons from 1983 to 2013 the lag-correlation analysis must be evaluated with caution.

A solar response around 4 K/100 SFU retrieved with the F10.7 cm index is comparable with what is reported for other locations in polar regions and midlatitudes during the last decade [*She and Krueger*, 2004; *Azeem et al.*, 2007; *Offermann et al.*, 2010; *French and Klekociuk*, 2011]. *Schmidt et al.* [2006] reported that temperature response in the mesopause to the solar cycle lies between 2 and 10 K. However, *Hall et al.* [2012] found a solar response coefficient of 16 K/100 SFU for the temperature series derived from the NSMR radar in Adventdalen, Longyearbyen. This is significantly higher than our response coefficient. It is likely that the main explanation for the large difference is the difference in time span of the two temperature series. While the OH* temperatures go back to 1983, the meteor radar temperatures go back to 2001. When only taking the OH*

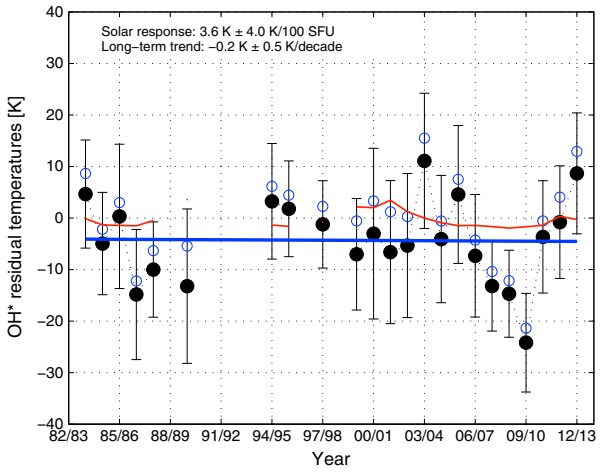

Figure 5. Hydroxyl (OH*) residual temperatures from Longyearbyen, 1983–2013, corrected for seasonal variations and solar response. Standard deviations are plotted as errorbars. Blue circles are seasonally averaged residuals corrected for climatology. The red line is the multivariate fit to the climatologically corrected residuals of the form $Fit_T = Y.Trend + S.F107 + const$. Seasonal averages corrected also for solar response are plotted as black bullets with standard deviations as errorbars. The blue line is the linear long-term trend.

temperatures from 2001 to 2011 into consideration, we get a solar response coefficient of 10.9 K/100 SFU. This is significantly higher than the coefficient estimated for the whole time period but still less than what was found by *Hall et al.* [2012]. A 10.9 K/100 SFU response is within the 95% confidence interval for the solar forcing of the overall fit to the data by F10.7 cm (see Table 3).

Sigernes et al. [2003] reported that there seemed to be no connection between the F10.7 cm flux and the OH* temperatures for the Longyearbyen data set from 1983 to 2001. Calculating the solar response coefficient for this time period gives a result that is close to 0 K/100 SFU. The length of the time series may be a reason for this. A long time series is required to assure a reliable result. The zero response from 1983 to 2001 is within the 95% confidence interval of the overall fit to the data.

Offermann et al. [2010] raise the question whether the solar response coefficient obtained by a linear fit between temperature and solar flux index gives an optimal approximation of the true value. They argued that the length of the time series at least had to be longer than one solar cycle, but even a long time series gives no guarantee for a correctly determined solar response coefficient.

3.3. Updated Trend, 1983–2013

A multivariate regression fit of the form $Fit_{temp} = Y.Trend + S.F107 + const$ was made to detect the long-term coefficient coupled with the solar cycle coefficient. This was done to take both parameters into account simultaneously. Figure 5 shows the multivariate fit to the seasonal temperatures with climatology removed, with no F10.7 lag.

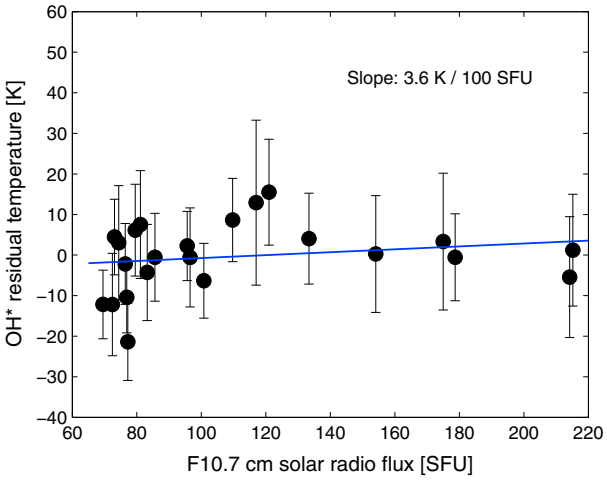

Figure 6. Scatterplot of the seasonally averaged temperatures against the corresponding F10.7 cm solar flux values. Standard deviations are plotted as errorbars. The blue line is the linear fit to the data.

Figure 6 shows a scatterplot of the seasonally averaged temperatures against the corresponding F10.7 cm solar flux values. The decoupled solar cycle component is 3.6 K ± 4.0 K/100 SFU. Figure 5 shows the decoupled long-term trend component. The uncertainty of the trend was estimated by removing 1 year at the time from the time window and estimating trends based on the remaining data points. This is commonly referred to as the bootstrap method. The standard deviation of the trends was considered the overall uncertainty [*Efron and Tibshirani*, 1993]. The long-term temperature trend is −0.2 K ± 0.5 K/decade. By performing a multivariate regression analysis with TSI values, which gave a higher correlation with the residuals at zero lag, the solar response coefficient is 4.2 K ± 3.2 K/Wm^{-2}.

Table 4. Seasonal and Monthly Trends

	Linear Trend	95% Confidence Intervals
Seasonal (F10.7 cm)	$-0.2\,K \pm 0.5$ K/decade	$-4.2\,K < Y < +4.0\,K$
Seasonal (TSI)	$-0.7\,K \pm 0.5$ K/decade	$-4.9\,K < Y < +3.4\,K$
November	$+4.5\,K \pm 1.1$ K/decade	$-2.6\,K < Y < +11.5\,K$
December	$-2.9\,K \pm 0.5$ K/decade	$-7.0\,K < Y < +12.2\,K$
January	$+1.4\,K \pm 0.6$ K/decade	$-4.3\,K < Y < +7.1\,K$
February	$+2.9\,K \pm 1.0$ K/decade	$-6.4\,K < Y < +12.2\,K$

The corresponding long-term trend is $-0.7\,K \pm 0.5$ K/decade. Ninety-five percent confidence limits for the seasonal trends are listed in Table 4.

There is variability in the temperature data set that is not accounted for by the seasonal variation or the solar cycle and long-term trend component. The regression fit is not an optimal fit to the residual temperatures. Around the cold period from 2008 to 2010, the difference between the regression fit and the seasonally averaged residual temperatures is between 10 and 20 K. The remaining variability may be explained by, e.g., planetary waves, gravity waves, SSWs, and instrument calibration uncertainty. SSWs occur quite often in the Northern Hemisphere and are believed to be connected with mesospheric processes [*Hoffmann et al*., 2007]. During the 1980s and after 2000, a large number of SSWs were detected (close to one major or minor warming per Arctic winter). As a contrast, very few SSWs were detected in the 1990s [*Kuttipurath and Nikulin*, 2012]. In the Southern Hemisphere, only one SSW has ever been observed. This occurred in September 2002 [*Peters et al*., 2007]. This may help explain why the variability in OH* temperatures is much larger in our data compared to, e.g., data from the Davis and the Amundsen-Scott South Pole stations. Gravity wave activity may be a source of temperature variability. However, both the Davis and the Amundsen-Scott stations experience substantial gravity wave activity [*Beldon and Mitchell*, 2009]. The remaining variability in temperatures not accounted for by the multivariate fit is thus not completely understood.

Another factor that can affect temperature variations and trends is changes in the altitude of the OH* layer. The height profile of the hydroxyl emission is determined by the shape of the bottom side of the atomic oxygen emission, i.e., the atomic oxygen scale height relative to that of the neutral atmosphere [*Beig et al*., 2003]. The peak altitude is controlled mainly by the rate of downward diffusion and gravity waves, tides, and planetary-scale disturbances which cause vertical motion of the peak. There is an inverse correlation between OH* altitude and integrated emission rate, and the brightness/intensity increases as the altitude decreases [e.g., *Liu and Shepherd*, 2006]. Thus, the hydroxyl rotational temperature corresponds, in general, neither to the temperature at a particular altitude nor to a particular pressure surface. Still, it is considered a good proxy for the temperature at the peak altitude [*Beig et al*., 2003].

The peak altitude of the OH* layer has been established by rocket and satellite measurements and is generally considered to be 87 km with a full width at half maximum (FWHM) of 8 km [*Baker and Stair*, 1988]. However, recent satellite measurements from polar latitudes have shown that the peak altitude of the OH* emissions can range from 75 to >90 km, particularly during winters when the polar vortex is disturbed and SSWs occur [*Winick et al*., 2009]. They also found that there is a longitudinal asymmetry depending on the position of the polar vortex. Furthermore, the peak altitude also varies with the upper vibrational level of the transition, and a recent paper found that it changes by about 0.5 km per vibrational level, the higher vibrational levels peaking at a higher altitude [*von Savigny et al*., 2012]. Since our paper presents data from only one vibrational band, the latter is not important to consider for this study.

For the Svalbard data, the inverse relationship between OH* peak altitude and emission rate/temperature has been verified using data from the winter season 2003–2004 [*Mulligan et al*., 2009], when the OH* layer peak altitude ranged from 76 to 90 km during a period of a highly disturbed circulation system over the Arctic. The low altitudes were attributed to downwelling due to the strengthening of the polar vortex after an SSW in January–February 2004 [*Dyrland et al*., 2010]. A temperature increase of the order of 15 K was attributed to the lowering of the layer, so the altitude is definitely a key factor in determining the OH* temperature [*Dyrland et al*., 2010]. Similarly, low OH* peak altitudes were observed after the SSW in 2006 [*Winick et al*., 2009]. Whether the relatively low temperatures from 2008 to 2010 can be connected to an unusually high OH* peak would be very interesting to study but is beyond the scope of this paper. To verify this, we would need satellite data overlapping our data. The only instrument that could provide this is SABER (Sounding of the Atmosphere using Broadband Emission Radiometry) on the TIMED (Thermosphere Ionosphere Mesosphere Energetics Dynamics) satellite. However, these data would only be

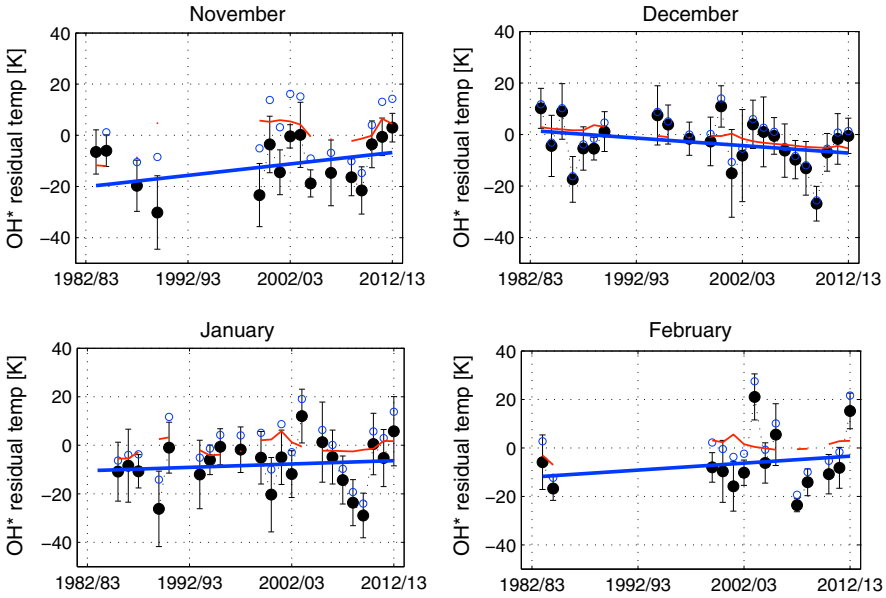

Figure 7. Monthly trends for November through February. Blue, hollow circles represent seasonally corrected residual temperatures. Red lines represent multivariate fits to the residuals. Monthly hydroxyl (OH*) temperatures corrected for both seasonal variations and solar response is plotted as black bullets, with standard deviations as errorbars. Blue lines are linear trends.

available for the latter part of the time series. Alternatively, the peak altitude could be modeled following the empirical measurements of OH* band intensity [*Mulligan et al.*, 2009; *Liu and Shepherd*, 2006]. However, the limited accuracy of the sensitivity calibrations (due to reasons mentioned in section 2.2: weather conditions, temperature, lamp currents etc.) makes it very difficult to verify the absolute intensity values for the data.

Compared to the last trend analysis done by *Dyrland and Sigernes* [2007], the new trend is now negative, but not significantly different from zero. The seasonally adjusted temperature residuals in, e.g., the 2009/2010 winter season is close to 10 K colder than for any of the other seasons. The period of lower temperatures around 2008 to 2010 contributes to that the trend is a near-zero trend, compared to the slightly positive trend found by *Dyrland and Sigernes* [2007].

Hall et al. [2012] found a negative trend of $-4\,\mathrm{K} \pm 2\,\mathrm{K}$/decade for the meteor radar temperatures from Longyearbyen. The reason for the large difference in trend is partly explained by the difference in solar response due to the time span of the two data sets and the fact that the meteor radar temperatures are recorded all year-round. Therefore, also summer trends are included in the meteor radar temperature trend. Some studies indicate that negative temperature trends in the mesosphere are most evident during summer, but others disagree [*Lübken*, 2000; *Bremer and Berger*, 2002; *Beig et al.*, 2008]. Also, the OH* emission peak altitude is slightly different from the altitude for maximum echo occurrence rate observed by the meteor radar [*Hall et al.*, 2012].

Other studies on long-term mesospheric temperature trends from midlatitude and high-latitude sites report mostly negative or near-zero trends. *Semenov* [2000] found a negative trend of $-9.2\,\mathrm{K} \pm 0.8$ K/decade for the winter mesosphere over several stations at midlatitudes. Temperatures were derived from rocket soundings, OH* airglow, lidar measurements, and interferometric measurements of oxygen emissions. *Reisin and Scheer* [2002] also reported a negative trend, $-10.5\,\mathrm{K} \pm 0.8\,\mathrm{K}$/decade, for airglow temperatures measured at El Leoncito (32°S, 69°W). The more recent study of *Offermann et al.* [2010] showed a trend of $-2.3\,\mathrm{K} \pm 0.6\,\mathrm{K}$/decade from the OH* temperature series from Wuppertal (51°N, 7°E). Studies from high-latitude sites show no clear pattern. *French and Klekociuk* [2011] reported a trend of $-1.2\,\mathrm{K} \pm 0.9\,\mathrm{K}$/decade for the Davis station (68°S, 78°E) in Antarctica for the period 1995 to 2011. *Azeem et al.* [2007] reported a trend of $+1.0\,\mathrm{K} \pm 2.0\,\mathrm{K}$/decade for the period 1994 to 2004 for the South Pole Station (90°S). Model simulations of the mesopause region indicate trends usually below 1 K/decade [*Beig et al.*, 2003]. Our trend is in line with this.

3.4. Monthly Trends

Monthly trends give an understanding of the seasonal variability of trends. Monthly averages were estimated for months with 4 or more days of retrieved data. Trends were estimated making multivariate regression fits. Uncertainties were calculated using the bootstrap method. Figure 7 shows the monthly residuals, multivariate fits, and linear trends for November through February. Trends and 95% confidence limits for all 4 months are listed in Table 4. The same pattern as for the data series as a whole, with low temperatures from 2008 to 2010, can also be seen in the monthly averages.

All monthly trends are positive, except for December. However, the 95% confidence intervals do not rule out negative trends for November, January, and February, or a positive trend for December.

Offermann et al. [2010] found negative trends for December, January, and February, while the trend for November was close to zero. *French and Klekociuk* [2011] found a trend close to zero for May, June, and July (corresponding to November, December, and January in the Northern Hemisphere) and a cooling trend for August (corresponding to February in NH). There seem to be few similarities between their monthly trends and ours. This indicates that there are high uncertainties, but also that the OH* layer in different parts of the world is influenced differently by gravity and planetary waves, solar variability, etc.

4. Summary and Conclusions

In this study, the long-term trend of the currently 30 year long hydroxyl airglow temperature series from Longyearbyen is updated. The mean climatology was subtracted from the data set to remove effects from seasonal variations. In the previous trend updates, the winter average has been calculated from temperatures from December and January, but since the temperatures in this paper have been seasonally corrected also November and February temperatures are included. Solar cycle dependence was investigated by looking into three different measures of solar variation; the F10.7 cm solar radio flux, the sunspot number, and the total solar irradiance. Highest correlation was achieved for OH* temperatures against TSI but only slightly better than for F10.7 and SSN. A solar response coefficient of around 4 K/100 SFU was obtained from the slope of linear fits to scatterplots of the temperature residuals against the F10.7 cm solar radio flux.

A lag-correlation analysis was performed on the data set to check for correlation improvement when a time lag was applied. Peak correlation for OH* temperatures and F10.7 occurred at a lag of ~65 days. At this point, F10.7 correlation exceeded SSN and TSI correlations. The lag-correlation analysis must be evaluated with caution since the data set is not continuous.

A multivariate regression fit of the form $Fit_{temp} = Y.Trend + S.F107 + const$ was made to detect long-term trend coupled with solar response. Decoupled solar response is 3.6 K ± 4.0 K/100 SFU, and the updated long-term trend of the Longyearbyen hydroxyl temperature series is −0.2 K ± 0.5 K/decade. Cold winter seasons between 2008 and 2010 turn the new trend slightly negative compared to the previous trend update by *Dyrland and Sigernes* [2007]. The cold winters occurred during a period of solar minimum, and this solar minimum is the weakest registered in nearly 100 years. Temperatures from the NSMR radar near Longyearbyen show the same tendency as the airglow temperatures.

There is variability in the data set not accounted for by seasonal variation or the solar cycle and long-term trend components. Remaining variability may be caused by planetary waves, gravity waves, and SSWs, but this issue is not fully understood. Also, changes in the altitude of the OH* layer can affect temperature variations. The peak altitude of the OH* emissions can change particularly during winters when the polar vortex is disturbed and SSWs occur.

The recent trend analysis on temperatures at 90 km altitude using meteor radar observations from Longyearbyen by *Hall et al.* [2012] shows a more negative trend and a stronger solar response for the meteor radar temperatures. One reason may be the different lengths of the time series. Our trend is in line with climate models that predict only small changes in temperature in the mesopause region with increasing CO_2 emissions [*Beig et al.*, 2003].

Monthly trends were also evaluated using multivariate regression fits. The analysis reveals that trends for November, January, and February are positive, while the December trend is negative. However, 95% confidence intervals do not rule out a positive December trend and negative trends for the other winter months.

Acknowledgments

This work was financially supported by The Research Council of Norway through contract 223252/F50 (CoE) and the projects named: Norwegian and Russian Co-operation on Svalbard part 2 (196173/S30, NORUSCA2), Infrastructure for Space Physics related Research on Svalbard (195385, INFRASPACE), and High-Arctic Gravity waves and their impact on middle atmospheric circulation and temperature (204993). The authors wish to thank Chris Hall at Tromsø Geophysical Observatory, Norway, and Masaki Tsutsumi at the National Institute of Polar Research, Japan, for providing temperatures from the Nippon-Norway Svalbard Meteor Radar. Inquiries about calculated airglow temperatures used for this paper can be addressed to Fred Sigernes, The University Centre in Svalbard (freds@unis.no). Records of the daily sunspot number, F10.7 cm solar radio flux and total solar irradiance are freely available from the Solar Influences Data Analysis Center (SIDC), the National Geophysical Data Center (NGDC), and the Active Cavity Radiometer Irradiance Monitor (ACRIM), respectively.

References

Ahluwalia, H. S., and J. Jackiewicz (2011), Sunspot cycle 23 descent to an unusual minimum and forecasts for cycle 24 activity, *Adv. Space Res.*, *50*, doi:10.1016/j.asr.2011.04.023.

Akmaev, R. A., and V. I. Fomichev (1998), Cooling of the mesosphere and lower thermosphere due to doubling of CO_2, *Ann. Geophys.*, *16*, 1501–1512.

Akmaev, R. A., and V. I. Fomichev (2000), A model estimate of cooling in the mesosphere and lower thermosphere due to the CO_2 increase over the last 3-4 decades, *Geophys. Res. Lett.*, *27*(14), 2113–2116, doi:10.1029/1999GL011333.

Azeem, S. M. I., G. G. Sivjee, Y.-I. Won, and C. Mutiso (2007), Solar cycle signature and secular long-term trend in OH airglow temperature observations at South Pole, Antarctica, *J. Geophys. Res.*, *112*, A01305, doi:10.1029/2005JA011475.

Baker, D. J., and A. T. Stair Jr. (1988), Rocket measurements of the altitude distribution of the hydroxyl airglow, *Phys. Scripta*, *37*, 611–622.

Beig, G., et al. (2003), Review of mesospheric temperature trends, *Rev. Geophys.*, *41*(4), 1015, doi:10.1029/2002RG000121.

Beig, G., J. Scheer, M. G. Mlynczak, and P. Keckhut (2008), Overview of the temperature response in the mesosphere and lower thermosphere to solar activity, *Rev. Geophys.*, *46*, RG3002, doi:10.1029/2007RG000236.

Beig, G., S. Fadnavis, H. Schmidt, and G. P. Brasseur (2012), Inter-comparison of 11-year solar cycle response in mesospheric ozone and temperature obtained by HALOE satellite data and HAMMONIA model, *J. Geophys. Res.*, *117*, D00P10, doi:10.1029/2011JD015697.

Beldon, C. L., and N. J. Mitchell (2009), Gravity waves in the mesopause region observed by meteor radar, 2: Climatologies of gravity waves in the Antarctic and Arctic, *J. Atmos. Sol. Terr. Phys.*, *71*, 875–884, doi:10.1016/j.jast.2009.03.009.

Bevington, B. R., and D. K. Robinson (1992), *Data Reduction and Error Analysis for the Physical Sciences*, McGraw-Hill, New York.

Brasseur, G., and M. H. Hitchman (1988), Stratospheric response to trace gas pertubations: Changes in ozone and temperature distributions, *Science*, *240*, 634–637.

Bremer, J., and U. Berger (2002), Mesospheric temperature trends derived from ground-based LF phase-height observations at mid-latitudes: comparison with model simulations, *J. Atmos. Sol. Terr. Phys.*, *64*, 805–816.

Cosby, P. C., and T. G. Slanger (2007), OH spectroscopy and chemistry investigated with astronomical sky spectra, *Can. J. Phys.*, *85*, 77–99, doi:10.1139/P06-088.

Dickinson, R. E., and R. J. Cicerone (1986), Future global warming from atmospheric trace gases, *Nature*, *319*, 109–115.

Dyrland, M. E., and F. Sigernes (2007), An update on the hydroxyl airglow temperature record from the Auroral Station in Adventdalen, Svalbard (1980-2005), *Can. J. Phys.*, *85*(2), 143–151, doi:10.1139/P07-040.

Dyrland, M. E., F. J. Mulligan, C. M. Hall, F. Sigernes, M. Tsutsumi, and C. S. Deehr (2010), Response of OH airglow temperatures to neutral air dynamics at 78°N, 16°E during the anomalous 2003–2004 winter, *J. Geophys. Res.*, *115*, D07103, doi:10.1029/2009JD012726.

Efron, B., and T. Tibshirani (1993), *An introduction to the bootstrap*, Chapman and Hall, New York.

French, W. J. R., and A. R. Klekociuk (2011), Long-term trends in Antarctic winter hydroxyl temperatures, *J. Geophys. Res.*, *116*, D00P09, doi:10.1029/2011JD015731.

Funke, B., M. López-Puertas, D. Bermejo-Pantaleón, M. Garcia-Comas, G. P. Stiller, T. von Clarmann, M. Kiefer, and A. Linden (2010), Evidence for dynamical coupling from the lower atmosphere to the thermosphere during a major stratospheric warming, *Geophys. Res. Lett.*, *37*, L13803, doi:10.1029/2010GL043619.

Hall, C. M., M. E. Dyrland, M. Tsutsumi, and F. J. Mulligan (2012), Temperature trends at 90 km over Svalbard, Norway (78°N 16°E), seen in one decade of meteor radar observations, *J. Geophys. Res.*, *117*, D08104, doi:10.1029/2011JD017028.

Hoffmann, P., W. Singer, D. Keuer, W. K. Hocking, M. Kunze, and Y. Murayama (2007), Latitudinal and longitudinal variability of mesospheric winds and temperatures during stratospheric warming events, *J. Atmos. Sol. Terr. Phys.*, *69*, 2355–2366.

Holmen, S. E., M. E. Dyrland, and F. Sigernes (2014), Mesospheric temperatures derived from three decades of hydroxyl airglow measurements from Longyearbyen, Svalbard (78°N), *Acta Geophys.*, *62*(2), 302–315, doi:10.2478/s11600-013-0159-4.

Huang, T. Y. W., and G. P. Brasseur (1993), Effect of long-term variability in a two-dimensional interactive model of the middle atmosphere, *J. Geophys. Res.*, *98*(D11), 20,413–20,427, doi:10.1029/93JD02187.

Kuttipurath, J., and G. Nikulin (2012), A comparative study of the major sudden stratospheric warmings in the Arctic winters 2003/2004-2009/2010, *Atmos. Chem. Phys.*, *12*, 8115–8129, doi:10.5194/acp-12-8115-2012.

Liu, G., and G. G. Shepherd (2006), An empirical model for the altitude of the OH nightglow emission, *Geophys. Res. Lett.*, *33*, L09805, doi:10.1029/2005GL025297.

Lübken, F.-J. (2000), Nearly zero temperature trend in the polar summer mesosphere, *Geophys. Res. Lett.*, *27*(21), 3603–3606, doi:10.1029/2000GL011893.

Mies, F. H. (1974), Calculated vibrational transition probabilities of OH($X_2\Pi$), *J. Mol. Spectrosc.*, *53*, 150–188.

Mulligan, F. J., M. E. Dyrland, F. Sigernes, and C. S. Deehr (2009), Inferring hydroxyl layer peak heights from ground-based measurements of OH(6-2) band integrated emission rate at Longyearbyen (78°N, 16°E), *Ann. Geophys.*, *27*, 4197–4205.

Offermann, D., P. Hoffmann, P. Knieling, R. Koppmann, J. Oberheide, and W. Steinbrecht (2010), Long-term trends and solar cycle variations of mesospheric temperature and dynamics, *J. Geophys. Res.*, *115*, D18127, doi:10.1029/2009JD013363.

Pendleton, W. R., P. J. Espy, and M. R. Hammond (1993), Evidence for non-local-thermodynamical-equilibrium rotation in the OH nightglow, *J. Geophys. Res.*, *98*(A7), 2156–2202, doi:10.1029/93JA00740.

Perminov, V. I., A. I. Semenov, and N. N. Shefov (2007), On Rotational Temperature of the Hydroxyl Emission, *Geomagn. Aeron.*, *47*(6), 756–763, doi:10.1134/S0016793207060084.

Peters, D., P. Vargin, and H. Koernich (2007), A study of the zonally asymmetric tropospheric forcing of the austral vortex splitting during September 2002, *Tellus*, *59A*, 384–394, doi:10.1111/j.1600-0870.2007.00228.x.

Reisin, E. R., and J. Scheer (2002), Searching for trends in mesopause region airglow intensities and temperatures at El Leoncito, *Phys. Chem. Earth*, *27*, 563–569.

Schmidt, H., and G. P. Brasseur (2006), The response of the middle atmosphere to solar cycle forcing in the Hamburg Model of the Neutral and Ionized Atmosphere, *Space Sci. Rev.*, *125*, 345–356, doi:10.1007/s11214-006-9068-z.

Schmidt, H., G. P. Brasseur, M. Charron, E. Manzini, M. A. Giorgetta, and T. Diehl (2006), The HAMMONIA Chemistry Climate Model: Sensitivity of the Mesopause Region to the 11-year Solar Cycle and CO_2 Doubling, *J. Clim.*, *19*(16), 3903–3931, doi:10.1175/JCLI3829.1.

Semenov, A. I. (2000), Long Term Temperature Trends for Different Seasons by Hydroxyl Emission, *Phys. Chem. Earth Part B*, *25*(5-6), 525–529.

Shapiro, A. V., E. Rozanov, A. I. Shapiro, S. Wang, T. Egorova, W. Schmutz, and T. Peter (2012), Signature of the 27-day solar rotation cycle in mesospheric OH and H_2O observed by the Aura Microwave Limb Sounder, *Atmos. Chem. Phys.*, *12*, 3181–3188, doi:10.5194/acp-12-3181-2012.

She, C. Y., and D. A. Krueger (2004), Impact of natural variability in the 11-year mesopause region temperature observation over Fort Collins, CO (41°N, 105°W), *Adv. Space Res.*, *34*, 330–336, doi:10.1016/j.asr.2003.02.047.

Sigernes, F., N. Shumilov, C. S. Deehr, K. P. Nielsen, T. Svenøe, and O. Havnes (2003), Hydroxyl rotational temperature record from the auroral station in Adventdalen, Svalbard (78°N, 15°E), *J. Geophys. Res.*, *108*(A9), 1342, doi:10.1029/2001JA009023.

Sigernes, F., J. M. Holmes, M. Dyrland, D. A. Lorentzen, S. A. Chernouss, T. Svenøe, J. Moen, and C. S. Deehr (2007), Absolute calibration of optical devices with a small field of view, *J. Opt. Technol.*, *74*(10), 669–674, doi:10.1364/JOT.74.000669.

Sigernes, F., et al. (2012), Hyperspectral all-sky imaging of auroras, *Opt. Express*, *20*(25), 27,650–27,660.

Sivjee, G. G., and R. M. Hamwey (1987), Temperature and chemistry of the polar mesopause OH, *J. Geophys. Res.*, *92*(A5), 4663–4672, doi:10.1029/JA092iA05p04663.

von Savigny, C., I. C. McDade, K.-U. Eichmann, and J. P. Burrows (2012), On the dependence of the OH^* Meinel emission altitude on vibrational level: SCIAMACHY observations and model simulations, *Atmos. Chem. Phys.*, *12*, 8813–8828, doi:10.5194/acp-12-8813-2012.

Winick, J. R., P. P. Wintersteiner, R. H. Picard, D. Esplin, M. G. Mlynczak, J. M. Russell III, and L. L. Gordley (2009), OH layer characteristics during unusual boreal winters of 2004 and 2006, *J. Geophys. Res.*, *114*, A02303, doi:10.1029/2008JA013688.

Wynn, T. A., and V. B. Wickwar (2009), The effects of model misspecification on linear regression coefficients as applicable to solar and linear terms, *Annual Report of the Rocky Mountain NASA Space Grant Consortium*.

Paper 3

Change in turbopause altitude at 52 and 78°N

Hall, C. M., S. E. Holmen, C. E. Meek, A. H. Manson and S. Nozawa

Published in Atmospheric Chemistry and Physics, 16, 2299–2308, doi: 10.5194/acp-16-2299-2016, 2016.

Atmos. Chem. Phys., 16, 2299–2308, 2016
www.atmos-chem-phys.net/16/2299/2016/
doi:10.5194/acp-16-2299-2016

Atmospheric Chemistry and Physics Open Access EGU

Change in turbopause altitude at 52 and 70° N

Chris M. Hall[1], **Silje E. Holmen**[1,2,5], **Chris E. Meek**[3], **Alan H. Manson**[3], **and Satonori Nozawa**[4]

[1]Tromsø Geophysical Observatory, UiT – The Arctic University of Norway, Tromsø, Norway
[2]The University Centre in Svalbard, Svalbard, Norway
[3]University of Saskatchewan, Saskatoon, Canada
[4]Nagoya University, Nagoya, Japan
[5]Birkeland Centre for Space Science, Bergen, Norway

Correspondence to: Chris M. Hall (chris.hall@uit.no)

Received: 5 May 2015 – Published in Atmos. Chem. Phys. Discuss.: 24 July 2015
Revised: 22 January 2016 – Accepted: 10 February 2016 – Published: 26 February 2016

Abstract. The turbopause is the demarcation between atmospheric mixing by turbulence (below) and molecular diffusion (above). When studying concentrations of trace species in the atmosphere, and particularly long-term change, it may be important to understand processes present, together with their temporal evolution that may be responsible for redistribution of atmospheric constituents. The general region of transition between turbulent and molecular mixing coincides with the base of the ionosphere, the lower region in which molecular oxygen is dissociated, and, at high latitude in summer, the coldest part of the whole atmosphere.

This study updates previous reports of turbopause altitude, extending the time series by half a decade, and thus shedding new light on the nature of change over solar-cycle timescales. Assuming there is no trend in temperature, at 70° N there is evidence for a summer trend of $\sim 1.6\,\mathrm{km\,decade^{-1}}$, but for winter and at 52° N there is no significant evidence for change at all. If the temperature at 90 km is estimated using meteor trail data, it is possible to estimate a cooling rate, which, if applied to the turbopause altitude estimation, fails to alter the trend significantly irrespective of season.

The observed increase in turbopause height supports a hypothesis of corresponding negative trends in atomic oxygen density, [O]. This supports independent studies of atomic oxygen density, [O], using mid-latitude time series dating from 1975, which show negative trends since 2002.

1 Introduction

The upper mesosphere and lower thermosphere (UMLT) regime of the atmosphere exhibits a number of features, the underlying physics of which are interlinked and, relative to processes at other altitudes, little understood. At high latitude, the summer mesopause, around 85 km is the coldest region in the entire atmosphere. The UMLT is, inter alia, characterised by the base of the ionosphere, dissociation of molecular species (for example oxygen) by sunlight, and, the focus in this study, the transition from turbulent mixing to distribution of constituents by molecular diffusion. The altitude at which transition turbulence-dominated mixing gives way to molecular diffusion is known as the turbopause, and typically occurs around 100 km, but displaying a seasonal variation, being lower in summer (e.g. ~ 95 km) and higher in winter (e.g. ~ 110 km) (Danilov et al., 1979). Many processes in the UMLT are superimposed and linked. One example is where the mesopause temperature structure determines the altitude dependence of breaking of upwardly propagating gravity waves (e.g. McIntyre, 1991) and thus generation of turbulence. Indeed, the concept of a "wave turbopause" was proposed by Offermann et al. (2007) and compared with the method used forthwith by Hall et al. (2008). Prevailing winds filter or even inhibit propagation of gravity waves generated in the lower atmosphere, and the static stability (or lack of it) of the atmosphere dictates the vertical distribution of gravity wave saturation and breaking. The generation of turbulence and its height distribution vary with season and similarly affect the turbopause altitude (e.g. Hall et al., 1997). Turbulence is somewhat distributed through the high-latitude win-

ter mesosphere, whereas in summer the gravity waves "save their energy" more until reaching the "steep beach" (a visualisation attributable to M. E. McIntyre, personal communication, 1988) of the summer mesopause near 85 km. Vertical transport by turbulent mixing and horizontal transport by winds redistribute constituents such as atomic oxygen, hydroxyl and ozone. Thus, long-term change in trace constituents cannot be fully explained in isolation from studies of corresponding change in temperature and neutral dynamics.

One means of locating the turbopause is to measure the concentration of particular species as a function of height and noting where the constituents exhibit scale heights that depend on their respective molecular weights (e.g. Danilov et al., 1979). Detection of turbulence and estimation of its intensity is non-trivial because direct measurement by radar depends on turbulent structures being "visible" due to small discontinuities in refractive index (e.g. Schlegel et al., 1978, and Briggs, 1980). At 100 km, this implies some degree of ionisation and even in situ detectors often depend on ionisation as a tracer (e.g. Thrane et al., 1987). A common means of quantifying turbulent intensity is the estimation of turbulent energy dissipation rate, ε. In the classical visualisation of turbulence in two dimensions, large vortices generated by, for example, breaking gravity waves or wind shears form progressively smaller vortices (eddies) until inertia is insufficient to overcome viscous drag in the fluid. Viscosity then "removes" kinetic energy and transforms it to heat. This "cascade" from large-scale vortices to the smallest-scale eddies capable of being supported by the fluid, and subsequent dissipation of energy, was proposed by Kolmogorov (1941) but more accessibly described by Batchelor (1953) and, for example, Kundu (1990). At the same time, a minimum rate of energy dissipation by viscosity is supported by the atmosphere (defined subsequently). The altitude at which these two energy dissipation rates are equal is also a definition of the turbopause and corresponds to the condition where the Reynolds number, the ratio between inertial and viscous forces, is unity.

The early work to estimate turbulent energy dissipation rates using medium-frequency (MF) radar by Schlegel et al. (1978) and Briggs (1980) was adopted by Hall et al. (1998a). The reader is referred to these earlier publications for a full explanation, but in essence velocity fluctuations relative to the background wind give rise to fading with time of echoes from structures in electron density drifting through the radar beam. While the drift is determined by cross-correlation of signals from spaced receiver antennas, autocorrelation yields fading times which may be interpreted as velocity fluctuations (the derivation of which is given in the following section). The squares of the velocity perturbations can be equated to turbulent kinetic energy and then when divided by a characteristic timescale become energy dissipation rates. Energy is conserved in the cascade to progressively smaller and more numerous eddies such that the energy dissipation rate is representative of the ultimate conversion of kinetic energy to heat by viscosity. Hall et al. (1998b, 2008) subsequently applied the turbulent intensity estimation to identification of the turbopause. The latter study, which offers a detailed explanation of the analysis, compares methods and definitions and represents the starting point for this study. In addition, Hocking (1983, 1996) and Vandepeer and Hocking (1993) offer a critique on assumptions and pitfalls pertaining to observation of turbulence using radars. For the radars to obtain echoes from the UMLT, a certain degree of ionisation must be present and daylight conditions yield better results than night-time, and similarly results are affected by solar cycle variation. However, there is a trade-off: too little ionisation prevents good echoes while too much gives rise to the problem of group delay of the radar wave in the ionospheric D region. Space weather effects that are capable of creating significant ionisation in the upper mesosphere are infrequent, and aurora normally occur on occasional evenings at high latitude, and then only for a few hours' duration at the most. Of the substantial data set used in this study, however, only a small percentage of echo profiles are expected to be affected by auroral precipitation that would cause problematic degrees of ionisation below the turbopause. While it must be accepted that group delay at the radar frequencies used for the observations reported here cannot be dismissed, the MF-radar method is the only one that has been available for virtually uninterrupted measurement of turbulence in the UMLT region over the past decades.

Full descriptions of the radar systems providing the underlying data used here are to be found in Hall (2001) and Manson and Meek (1991); the salient features of the radars relevant for this study are given in Table 1.

2 Analysis methodology

The characteristic fading time of the signal, τ_c, is used to define an indication of the upper limit for turbulent energy dissipation present in the atmosphere, ε', as explained above. First, velocity fluctuations, v', relative to the background wind are identified as

$$v' = \frac{\lambda\sqrt{\ln 2}}{4\pi\,\tau_c}, \quad (1)$$

where λ is the radar wavelength. This relationship has been presented and discussed by Briggs (1980) and Vandepeer and Hocking (1993). In turn v'^2 can be considered to represent the turbulent kinetic energy of the air such that the rate of dissipation of this energy is obtained by dividing by a characteristic timescale. If the Brunt–Väisälä period T_B ($= 2\pi/\omega_B$ where ω_B is the Brunt–Väisälä frequency in rad s^{-1}) can be a characteristic timescale, then it has been proposed that

Table 1. Salient radar parameters.

Parameter	Tromsø	Saskatoon
Geographic coordinates	69.58° N, 19.22° E	52.21° N, 107.11° E
Operating frequency	2.78 MHz	2.22 MHz
Pulse length	20 µs	20 µs
Pulse repetition frequency	100 Hz	60 Hz
Power (peak)	50 kW	25 kW
Antenna beamwidth	17° at −3 dB	17° at −6 dB
Altitude resolution	3 km	3 km
Time resolution (post-analysis)	5 min	5 min

$$\varepsilon' = 0.8 v'^2 / T_\mathrm{B}, \tag{2}$$

the factor 0.8 being related to an assumption of a total velocity fluctuation (see Weinstock, 1978). Alternatively, this can be expressed as

$$\varepsilon' = 0.8 v'^2 \omega_\mathrm{B} / 2\pi, \tag{3}$$

wherein the Brunt–Väisälä frequency is given by

$$\omega_\mathrm{B} = \sqrt{\left(\frac{\mathrm{d}T}{\mathrm{d}z} + \frac{g}{c_p}\right)\frac{g}{T}}, \tag{4}$$

where T is the neutral temperature, z is altitude, g is the acceleration due to gravity and c_p is the specific heat of the air at constant pressure. Due to viscosity, there is a minimum energy dissipation rate, ε_min, present in the atmosphere, given by

$$\varepsilon_\mathrm{min} = \omega_\mathrm{B}^2 \nu / \beta, \tag{5}$$

where ν is the kinematic viscosity. The factor β, known as the mixing or flux coefficient (Oakey, 1982; Fukao et al., 1994; Pardyjak et al., 2002), is related to the flux Richardson number R_f ($\beta = R_\mathrm{f}/(1 - R_\mathrm{f})$). R_f is in turn related to the commonly used gradient Richardson number, *Ri*, by the ratio of the momentum to thermal turbulent diffusivities, or turbulent Prandtl number (e.g. Kundu, 1990). Fukao et al. (1994) proposed 0.3 as a value for β. The relationships are fully described by Hall et al. (2008). The MF-radar system employed here to estimate turbulence is not well suited to estimating *Ri* due to the height resolution of 3 km; moreover more detailed temperature information would be required to arrive at R_f.

Anywhere in the atmosphere, energy dissipation is by the sum of the available processes. In this study, therefore, the turbulent energy dissipation rate can be considered the total rate minus that corresponding to viscosity:

$$\varepsilon = \varepsilon' - \varepsilon_\mathrm{min}. \tag{6}$$

Importantly, the kinematic viscosity is given by the dynamic viscosity, μ, divided by the density, ρ:

$$\nu = \mu / \rho. \tag{7}$$

Thus, since density is inversely proportional to temperature, kinematic viscosity is (approximately) linearly dependent on temperature; ω_B^2 is inversely proportional to temperature and therefore ε_min is approximately independent of temperature. On the other hand, ε' is proportional to ω_B and therefore inversely proportional to the square root of temperature.

If we are able to estimate the energy dissipation rates described above, then the turbopause may be identified as the altitude at which $\varepsilon = \varepsilon_\mathrm{min}$. This corresponds to equality of inertial and viscous effects and hence the condition where Reynolds number, *Re*, is unity as explained earlier.

To implement the above methodology, temperature data are required. Since observational temperature profiles cannot be obtained reliably, NRLMSISE-00 empirical model (Picone et al., 2002) profiles are, of necessity, used in the derivation of turbulent intensity from MF-radar data. The reasons for this are discussed in detail in the following section. While a temperature profile covering the UMLT region is not readily available by ground-based observations from Tromsø, meteor-trail echo fading times measured by the Nippon/Norway Tromsø Meteor Radar (NTMR) can be used to yield neutral temperatures at 90 km altitude. Any trend in temperature can usefully be obtained (the absolute values of the temperatures being superfluous since they are only available for one height). The method is exactly the same as used by Hall et al. (2012) to determine 90 km temperatures over Svalbard (78° N) using a radar identical to NTMR. Hall et al. (2005) investigate the unsuitability of meteor radar data for temperature determination above ∼ 95 km and below ∼ 85 km. In summary, ionisation trails from meteors are observed using a radar operating at a frequency less than the plasma frequency of the electron density in the trail (this is the so-called "underdense" condition). It is then possible to derive ambipolar diffusion coefficients D from the radar echo decay times, τ_meteor (as distinct from the corresponding fading time for the medium-frequency radars), according to

$$\tau_{\text{meteor}} = \frac{\lambda^2}{16\pi^2 D}, \quad (8)$$

wherein λ is the radar wavelength. Thereafter the temperature T may be derived using the relation

$$T = \sqrt{\frac{P \cdot D}{6.39 \times 10^{-2} K_0}}, \quad (9)$$

where P is the neutral pressure and K_0 is the zero field mobility of the ions in the trail (here we assume $K_0 = 2.4 \times 10^{-4}\,\text{m}^{-2}\,\text{s}^{-1}\,\text{V}^{-1}$) (McKinley, 1961; Chilson et al., 1996; Cervera and Reid, 2000; Holdsworth et al., 2006). The pressure, P, was obtained from NRLMSISE-00 for consistency with the turbulence calculations. In the derivations by Dyrland et al. (2010) and Hall et al. (2012), for example, temperatures were then normalised to independent measurements by the MLS (Microwave Limb Sounder) on board the EOS (Earth Observing System) Aura spacecraft launched in 2004. The MLS measurements were chosen because the diurnal coverage was constant for all measurements, and it was therefore simpler to estimate values that were representative of daily means than other sources such as SABER. In this way, the influence of any systematic deficiencies in NRLMSISE-00 (e.g. due to the age of the model) was minimised.

3 Results and implications for changing neutral air temperature

Following the method described above and by Hall et al. (1998b, 2008), the turbopause position is determined as shown in Fig. 1. The time and height resolutions of the MF radars used for the investigation are 5 min and 3 km respectively, and daily means of turbulent energy dissipation rate profiles are used to determine corresponding turbopause altitudes. The figure shows the evolution since 1999: 70° N, 19° E (Tromsø) in the upper panel and 52° N, 107° W (Saskatoon) in the lower panel. Results are, of course, specific to these geographical locations and it must be stressed that they are in no way zonally representative (hereafter, though, "70° N" and "52° N" may be used to refer to the two locations for convenience). Data are available from 1 January 1999 to 25 June 2014 for Saskatoon, but thereafter technical problems affected data quality. Data are shown from 1 January 1999 to 25 October 2015 for Tromsø. The cyan background corresponding to the period 16 February 1999 to 16 October 2000 in the 70° N (Tromsø) panel indicates data available but using different experiment parameters, and thus 70° N data prior to 17 October 2000 are excluded from this analysis. A 30-day running mean is shown by the thick lines with the shading either side indicating the standard deviation. The seasonal variation is clear to see, and for illustrative purposes, trend lines have been fitted to June and December values together with hyperbolae showing the 95 % confidence limits in the linear fits (Working and Hotelling, 1929); the seasonal dependence of the trends is addressed in more detail subsequently. The months of June and December are chosen simply because these correspond to the solstices and thus to avoid any a priori conception of when one could anticipate the maxima and minima to be. It is evident that, apart from the seasonal variation, the mid-latitude turbopause changes little over the period 1999–2014, whereas at high latitude there is more change for the summer state over the period 2001–2015 (the summers of 1999 and 2000 being excluded from the fitting due to changes in experiment parameters for the Tromsø radar). To investigate the seasonal dependence of the change further, the monthly values for 70 and 52° N are shown in Fig. 2. Since 2001, the high-latitude turbopause has increased in height during late spring and mid-summer but otherwise remained constant. Since individual months are selected the possibility of "end-point" biases is not an issue in the trend-line fitting as would be the case if analysing entire data sets with non-integer numbers of years. Even so, certain years may be apparently anomalous, for example the summer of 2003. In this study, the philosophy is to look for any significant change in the atmosphere over the observational period. If anomalous years are caused by, for example, changes in gravity-wave production (perhaps due to an increasing frequency of storm in the troposphere) and filtering in the underlying atmosphere, these too should be considered part of climate change. The trend (or overall change) over the observation period is indeed sensitive to exclusion of certain years. Although not illustrated here, this was tested briefly: selecting data from only 2004 onwards indicates no significant change for summer, but a slightly increased negative winter change (to $-1.7 \pm 0.2\,\text{K decade}^{-1}$); excluding only 2003 (the visually anomalous year) fails to alter the summer and winter values significantly at all. The above findings represent an update of those by Hall et al. (1998b, 2008), adding more years to the time series and therefore now covering a little over one solar cycle (the latter half of cycle 23 and first half of 24). As for the preceding papers and for consistency the neutral atmosphere parameters (temperature and density) required have been obtained from the NRLMSISE-00 empirical model (Picone et al., 2002) and have been assumed not to exhibit any trend over the observation period. In other terms, 1-year seasonal climatology temperature models at 1-day resolution for 70 and 52° N and altitude range appropriate for the respective radars are therefore used for all years for consistency with earlier results and for consistency between the two latitudes studied here. Satellite-based temperature determinations are of course available, including for example SABER (Sounding of the Atmosphere by Broadband Emission Radiometry) on board TIMED (Thermosphere Ionosphere Mesosphere Energetics and Dynamics), which was launched in 2001. The temporal sampling by such instruments makes the estimation of (for example) daily means somewhat complicated. Moreover, the measurements are not necessarily representative of the field of view of the

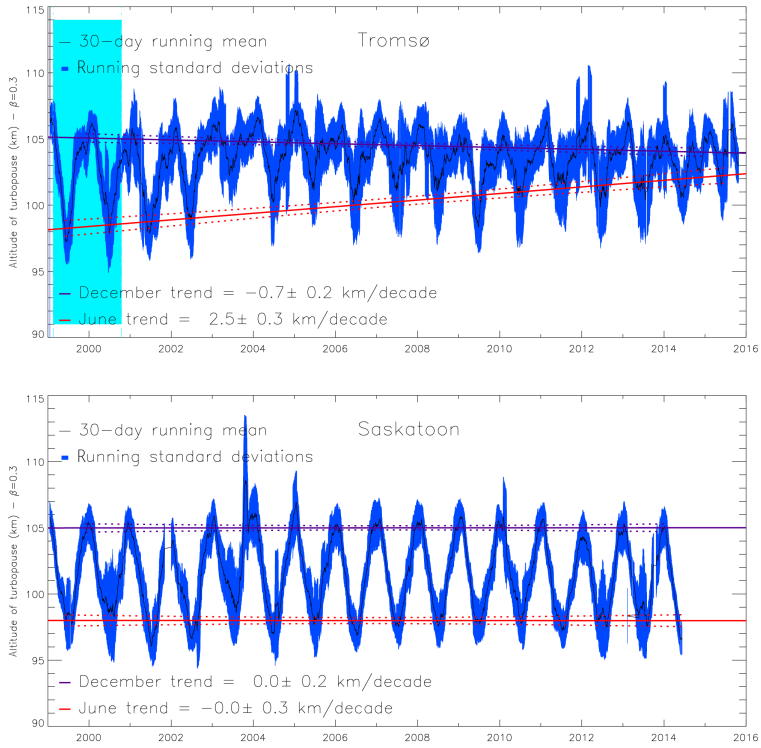

Figure 1. Turbopause altitude as determined by the definition and method described in this paper. The thick solid line shows the 30-day running mean and the shading behind it the corresponding standard deviations. The straight lines show the fits to summer and winter portions of the curve. Upper panel: 70° N (Tromsø); lower panel: 52° N (Saskatoon). The cyan background in the 70° N panel indicates data available but unused here due to different experiment parameters.

radar because the geographical coverage of remote sensing data needs to be sufficiently large to obtain the required annual coverage, since the sampling region can vary with season (depending on the satellite). Choice of the somewhat dated NRLMSISE-00 model at least allows the geographical location to be specified and furthermore ensures a degree of consistency between the two sets of radar observations and also earlier analyses. The only ground-based temperature observations both available and suitable are at 70° N and 90 km altitude as described earlier and used subsequently.

Next, we have attempted to investigate the effects of changing temperature. In a very simplistic approach, hypothetical altitude-invariant trends are imposed on the NRLMSISE-00 profiles. In other words, the same hypothetical trend is applied to all heights (in want of better information) in the NRLMSISE-00 profile to generate evolving (cooling or warming) temperature time series. The suggested trends vary from -20 to $+20$ K decade^{-1}, thus well encompassing any realistically conceivable temperature change (cf. Blum and Fricke, 2008; Danilov, 1997, Lübken, 1999). The result of applying hypothetical temperature trends to the time-invariant turbopause heights shown earlier is demonstrated in Fig. 3. Given the seasonal differences identified earlier, four combinations are shown: summer (average of May, June and July) and winter (average of November, December and January) for each geographic location. Realistic temperature trends can be considered within the range ± 6 K decade^{-1} such that the only significant response of turbopause height to temperature trend is for 70° N in summer.

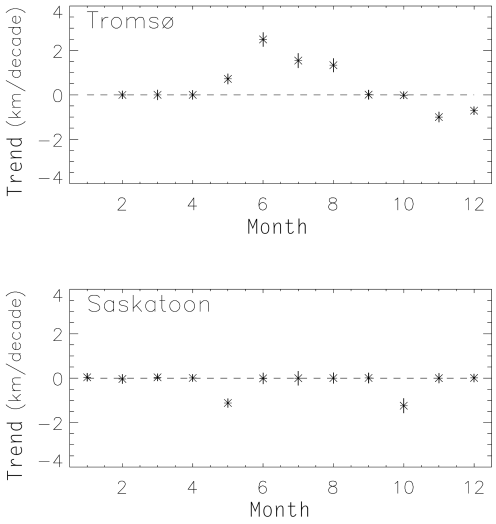

Figure 2. Trends for the period as a function of month. Upper panel: 70° N (Tromsø); lower panel: 52° N (Saskatoon).

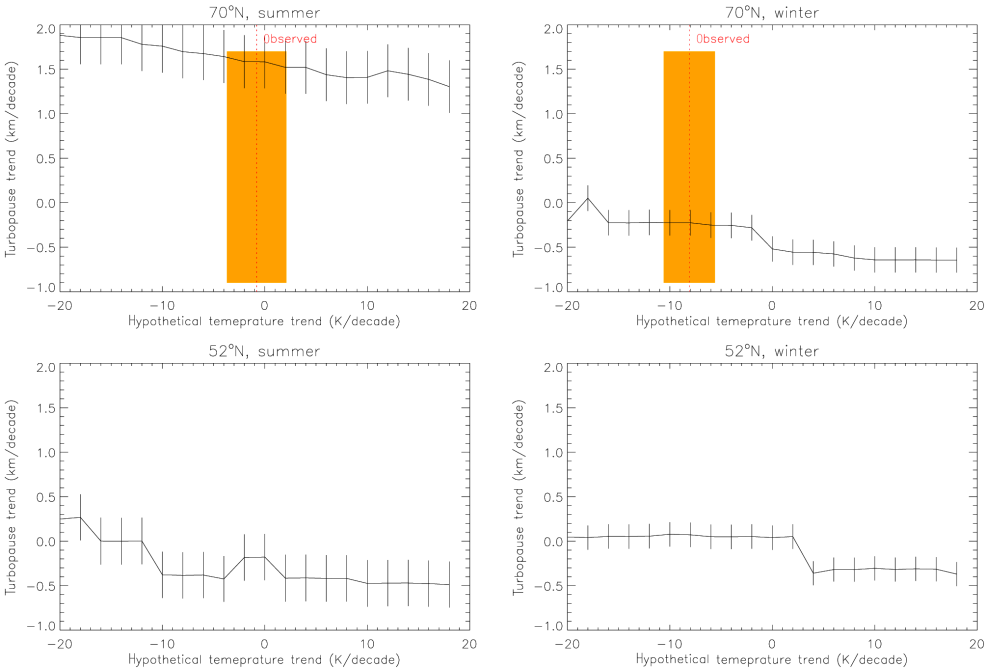

Figure 3. Response of turbopause trend line to different upper-mesosphere/lower-thermosphere temperature trends. Hypothetical trends range from an unrealistic cooling of 20 K decade^{-1} to a similarly unrealistic warming. Top left: 70° N summer (average of May, June and July); top right: 70° N winter (average of November, December and January); bottom left: 52° N summer; bottom right: 52° N winter. Observed values for 70° N are also identified on the upper panels (dashed vertical lines) together with uncertainties (shading).

In addition, the figure includes estimated trends obtained from observations, which shall be explained forthwith. The salient point arising from the figure is that no realistic temperature trend (at least given the simple model employed here) has the capability of reversing the corresponding trend in turbopause height.

In a recent study, Holmen et al. (2015) have built on the method of Hall et al. (2012) to determine 90 km temperatures over NTMR, as has been described in the previous section. This new work presents more sophisticated approaches for normalisation to independent measurements and investigation of the dependence of derived temperatures on solar flux. Having removed seasonal and solar cycle variations in order to facilitate trend-line fitting (as opposed to isolating a hypothetical anthropogenic-driven variation), Holmen et al. (2015) arrive at a temperature trend of -3.6 ± 1.1 K decade^{-1} determined over the time interval 2004–2014 inclusive. This can be considered statistically significant (viz. significantly non-zero at the 5 % level) since the uncertainty ($2\sigma = 2.2$ K decade^{-1}) is less than the trend itself (e.g. Tiao et al., 1990).

Estimations of changes in temperature corresponding to the period for determination of the turbopause were only viable for 70° N, these being -0.8 ± 2.9 K decade^{-1} for summer and -8.1 ± 2.5 K decade^{-1} for winter, and these results are indicated in Fig. 3. Again the simple idea of superimposing a gradual temperature change (the same for all heights) on the temperature model used for the turbulence determination thus fails to alter the change in turbopause height significantly, for the approximate decade of observations. Although direct temperature measurements are not available for the 52° N site, Offermann et al. (2010) report cooling rates of ~ 2.3 K decade^{-1} for 51° N, 7° E, and She et al. (2015) ~ 2.8 K decade^{-1} for 42° N, 112° W. As for 70° N, these results do not alter the conclusions inferred from Fig. 3.

4 Discussion

The aim of this study has been to update earlier reports (viz. Hall et al., 2008) of turbopause altitude and change determined for two geographic locations: 70° N, 19° E (Tromsø) and 52° N, 107° W (Saskatoon). An effort has been made to demonstrate that conceivable temperature trends are unable to alter the overall results, viz. that there is evidence of increasing turbopause altitude at 70° N, 19° E in summer, but otherwise no significant change during the period 2001 to 2014. Assimilating results from in situ experiments spanning the time interval 1966–1992, Pokhunkov et al. (2009) present estimates of turbopause height trends for several geographical locations, but during a period prior to that of our observations. For high latitudes the turbopause is reported to have fallen by $\sim$2–4 km between 1968 and 1989 – the opposite sign of our finding for 2001–2014. More recently, further evidence has been presented for a long-term descent of the tur-

bopause, at least at mid-latitude (Oliver et al., 2014, and references therein). The rationale for this is that the atomic oxygen density [O] has been observed to increase during the time interval 1975–2014 at a rate of approximately 1 % year^{-1}. The associated change in turbopause height may be estimated thusly as

$$H = RT/mg, \tag{10}$$

where H is scale height, R is the universal gas constant ($= 8.314\,\mathrm{J\,mol^{-1}\,K^{-1}}$), m is the mean molecular mass ($\mathrm{kg\,mol^{-1}}$) and g is the acceleration due to gravity. At 120 km altitude, g is taken to be $9.5\,\mathrm{m\,s^{-2}}$. For air and atomic oxygen, $m = 29$ and 16 respectively. For a typical temperature of 200 K, the two corresponding scale heights are therefore $H_{\mathrm{air}} = 6.04$ km and $H_{\mathrm{oxygen}} = 10.94$ km. If the change (fall) in turbopause height is denoted by Δh_{turb}, then Oliver et al. (2014) indicate that the factor by which [O] would increase is given by

$$\exp(\Delta h_{\mathrm{turb}}/H_{\mathrm{air}})/\exp(\Delta h_{\mathrm{turb}}/H_{\mathrm{oxygen}}). \tag{11}$$

Note that Oliver et al. (2014) state that "[O] … would increase by the amount", but, since Eq. (1) is dimensionless, the reader should be aware this is a factor, not an absolute quantity. At first, there would appear to be a fundamental difference between the findings derived from [O] at a mid-latitude station and those for ε from a high-latitude station, and indeed the paradox could be explained by either the respective methods and/or geographic locations. Usefully, in this context, Shinbori et al. (2014) and Kozubek et al. (2015) investigate such geographical diversity. However if one examines the period from 2002 onwards (corresponding to the high-latitude data set, but only about one-quarter of that from the mid-latitude station), a decrease in [O] corresponds with an increase in Δh_{turb}. If Δh_{turb} for the measured summer temperature change at high latitude (viz. 0.16 km year^{-1} from Fig. 3) is inserted in Eq. (1) together with the suggested scale heights for air and atomic oxygen, one obtains a corresponding decrease in [O] of 16 % decade^{-1} over the period 2002–2015. The corresponding time interval is not analysed per se by Oliver et al. (2014), but a visual inspection suggests a decrease of the order of 20 %; the decrease itself is incontrovertible and therefore in qualitative agreement with our high-latitude result.

It is somewhat unfortunate that it is difficult to locate simultaneous and approximately co-located measurements by different methods. The turbopause height change by Oliver et al. (2014) is derived by measurements of [O] and at mid-latitude; those by Pokhunkov et al. (2009), also by examining constituent scale heights, include determinations for Heiss Island (80° N, 58° E), but this rocket sounding programme was terminated prior to the start of our observation series (Danilov et al., 1979). It should be noted, however, that the results of seasonal variability presented by Danilov et al. (1979) agree well with those described here giving credence to the method and to the validity of the comparisons above.

Finally, the change in turbopause altitude during the last decade or more should be placed in the context of other observations. The terrestrial climate is primarily driven by solar forcing, but several solar cycles of data would be required to evaluate the effects of long-term change in space weather conditions on turbulence in the upper atmosphere. A number of case studies have been reported, however, that indicate how space weather events affect the middle atmosphere (Jackman et al., 2005; Krivolutsky et al., 2006). One recurring mechanism is forced change in stratospheric chemistry (in particular, destruction and production of ozone and hydroxyl); the associated perturbations in temperature structure adjust the static stability of the atmosphere through which gravity waves propagate before reaching the mesosphere. In addition, greenhouse gases causing global warming in the troposphere act as refrigerants in the middle atmosphere and so changing the static stability and therefore the degree to which gravity waves shed turbulence en route to the UMLT. Not a subject of this study, it is hypothesised that changes in the troposphere and oceans give rise to a higher frequency of violent weather; this in turn could be expected to increase the overall gravity wave activity originating in the lower atmosphere but propagating through the middle atmosphere. Sudden stratospheric warmings (SSWs) also affect (by definition) the vertical temperature structure and thus gravity wave propagation (e.g. de Wit et al., 2015; Cullens et al., 2015). Apart from direct enhancements of stratospheric temperatures, SSWs have been demonstrated to affect planetary wave activity even extending into the opposite hemisphere (e.g. Stray et al., 2015). If such effects were capable of, for example, triggering the springtime breakdown of the polar vortex, associated horizontal transport of stratospheric ozone would contribute to determination of the tropopause altitude (e.g. Hall, 2013) and, again, gravity wave propagation. Overall change in the stratosphere is proposed as the origin of the observed strengthening of the Brewer–Dobson circulation during the last 35 years at least (Fu et al., 2015). Closer to the 70° N, 19° E (Tromsø) observations, Hoffmann et al. (2011) report increases in gravity wave activity at 55° N, 13° E during summer, including at 88 km. Although not co-located, the increasing gravity wave flux, with waves breaking at the summer high-latitude mesopause, would similarly increase turbulence intensity and support the change reported here. Further references to long-term change in the middle and upper atmosphere in general can be found in Cnossen et al. (2015). Background winds and superimposed tides thus affecting gravity wave propagation and filtering in the atmosphere underlying the UMLT also vary from location to location at high latitude, and the two studies by Manson et al. (2011) study this zonal difference and compare with a current model. However, for approximately 10° further north than the Tromsø radar site, these studies give valuable

background information, not only on the wind field but also on tidal amplitude perturbation due to deposition of gravity waves' horizontal momentum.

5 Conclusion

Updated temporal evolutions of the turbopause altitude have been presented for two locations: 70° N, 19° E (Tromsø) and 52° N, 107° W (Saskatoon), the time interval now spanning 1999 to 2015. These turbopause altitude estimates are derived from estimates of turbulent energy dissipation rate obtained from medium-frequency radars. The method entails knowledge of neutral temperature that had earlier (Hall et al., 2008) been assumed to be constant with time. Here the response of the change in turbopause heights over the period of the study to temperature trends – both hypothetical and observed – is examined. No temperature trend scenario was capable of altering the observed turbopause characteristics significantly; at 70° N, 19° E an increase in turbopause height is evident during the 1999–2015 period for summer months, whereas for winter at 70° N, 19° E and all seasons at 52° N, 107° W the turbopause height has not changed significantly. In evaluating these results, however, there are a number of caveats that must be remembered. Firstly, the radar system does not perform well with an aurorally disturbed D region – the study, on the other hand incorporates well over 100 000 h of data for each radar site, and auroral conditions are occasional and of the order of a few hours each week at most. Secondly, an influence of the semi-empirical model used to provide both density and Brunt–Väisälä frequencies cannot be disregarded. It should also be stressed that a change is being reported for the observational periods of approximately 15 years (i.e. just over one solar cycle) and parameterised by fitting linear trend lines to the data; this is distinct from asserting long-term trends in which solar and anthropogenic effects can be discriminated.

At first, this conclusion would appear to contradict the recent report by Oliver et al. (2014) and Pokhunkov et al. (2009). However, closer inspection shows that if one considers the time interval 2002–2012 in isolation, there is a qualitative agreement. In fact, we note that Oliver et al. (2014) deduce a turbopause change based on changing atomic oxygen concentration and so we are similarly able to deduce a change in atomic oxygen concentration based on the change in turbopause height obtained from direct estimation of turbulence intensity. Given an average (i.e. not differentiating between seasons) temperature change of $-3.4 \pm 0.5\,\mathrm{K\,decade^{-1}}$ for 70° N, 19° E (Tromsø), the change in turbopause height in summer over the same time interval is $1.6 \pm 0.3\,\mathrm{km\,decade^{-1}}$ suggesting a decrease in atomic oxygen concentration of 16 %.

The primary aim of this study is to demonstrate the increasing altitude of the summer turbopause at 70° N, 19° E and the apparently unvarying altitude in winter and at 52° N, 107° W during the time interval 1999–2014. Independent studies using a radically different method demonstrate how to infer a corresponding decrease in atomic oxygen concentration, as a spin-off result. Finally, the question as to the exact mechanism causing the evolution of turbulence in the lower thermosphere at, in particular 70° N, 19° E, remains unanswered. Furthermore, dynamics at this particular geographic location may be pathological. The solution perhaps lies in seasonally dependent gravity wave filtering in the underlying atmosphere being affected by climatic tropospheric warming and/or middle atmosphere cooling; hitherto, however, this remains a hypothesis.

Acknowledgements. The authors thank the referees of this paper.

Edited by: G. Stiller

References

Batchelor, G. K.: The theory of homogeneous turbulence, 197 pp., Athenaceum Press Ltd., Newcastle-upon-Tyne, Great Britain, 1953.

Blum, U. and Fricke, K. H.: Indications for a long-term temperature change in the polar summer middle atmosphere, J. Atmos. Sol.-Terr. Phy., 70, 123–137, 2008

Briggs, B. H.: Radar observations of atmospheric winds and turbulence: a comparison of techniques, J. Atmos. Terr. Phys., 42, 823–833, 1980.

Cervera, M. A. and Reid, I. M.: Comparison of atmospheric parameters derived from meteor observations with CIRA, Radio Sci., 35, 833–843, 2000.

Chilson, P. B., Czechowsky, P., and Schmidt, G.: A comparison of ambipolar diffusion coefficients in meteor trains using VHF radar and UV lidar, Geophys. Res. Lett., 23, 2745–2748, 1996.

Cnossen, I., Laštovička, J., and Emmert, J. T.: Introduction to special issue on "Long-term changes and trends in the stratosphere, mesosphere, thermosphere and ionosphere", J. Geophys. Res., 120, 11401–11403, doi:10.1002/2015JD024133, 2015.

Cullens, C. Y., England, S. L., and Immel, T. J.: Global responses of gravity waves to planetary waves during stratospheric sudden warming observed by SABER, J. Geophys. Res., 120, 12018–12026, doi:10.1002/2015JD023966, 2015.

Danilov, A. D., Kalgin, U. A., and Pokhunov, A. A.: Variation of the mesopause level in polar regions, Space Res. XIX, 83, 173–176, 1979.

Dyrland, M. E., Hall, C. M., Mulligan, F. J., and Tsutsumi, M.: Improved estimates for neutral air temperatures at 90 km and 78° N using satellite and meteor radar data, Radio Sci., 45, RS4006, doi:10.1029/2009RS004344, 2010.

Fu, Q., Lin, P., Solomon, S., and Hartmann, D. L.: Observational evidence of the strengthening of the Brewer-Dobson circulation since 1980, J. Geophys. Res., 120, 10214–10228, doi:10.1002/2015JD023657, 2015.

Fukao, S., Yamanaka, M. D., Ao, N., Hocking, W. K., Sato, T., Yamamoto, M., Nakamura, T., Tsuda, T., and Kato, S.: Seasonal variability of vertical eddy diffusivity in the middle atmosphere,

1. Three-year observations by the middle and upper atmosphere radar, J. Geophys. Res., 99, 18973–18987, 1994.

Hall, C. M.: The Ramfjormoen MF radar (69° N, 19° E): Application development 1990–2000, J. Atmos. Sol.-Terr. Phy., 63, 171–179, 2001.

Hall, C. M.: The radar tropopause above Svalbard 2008–2012: characteristics at various timescales, J. Geophys. Res., 118, 2600-2608, doi:10.1002/jgrd.50247, 2013.

Hall, C. M., Blix, T. A., Thrane, E. V., and Lübken, F.-J.: Seasonal variation of mesospheric turbulent kinetic energy dissipation rates at 69° N, Proc. 13th ESA symposium, 505–509, 1997.

Hall, C. M., Manson, A. H., and Meek, C. E.: Measurements of the arctic turbopause, Ann. Geophys., 16, 342–345, 1998a.

Hall, C. M., Manson, A. H., and Meek, C. E.: Seasonal variation of the turbopause: One year of turbulence investigation at 69° N by the joint University of Tromsø/University of Saskatchewan MF radar, J. Geophys. Res., 103, 28769–28773, 1998b.

Hall, C. M., Aso, T., Tsutsumi, M., Nozawa, S., Manson, A. H., and Meek, C. E.: *Letter to the Editior* Testing the hypothesis of the influence of neutral turbulence on the deduction of ambipolar diffusivities from meteor trail expansion, Ann. Geophys., 23, 1071–1073, doi:10.5194/angeo-23-1071-2005, 2005.

Hall, C. M., Meek, C. E., Manson, A. H., and Nozawa, S.: Turbopause determination, climatology and climatic trends, using medium frequency radars at 52° and 70° N, J. Geophys. Res., 113, D13104, doi:10.1029/2008JD009938, 2008.

Hall, C. M., Dyrland, M. E., Tsutsumi, M., and Mulligan, F.: Temperature trends at 90 km over Svalbard seen in one decade of meteor radar observations, J. Geophys. Res., 117, D08104, doi:10.1029/2011JD017028, 2012.

Hocking, W. K.: On the extraction of atmospheric turbulence parameters from radar backscatter Doppler spectra – I. Theory, J. Atmos. Terr. Phys., 45, 89–102, 1983.

Hocking, W. K.: An assessment of the capabilities and limitations of radars in measurements of upper atmosphere turbulence, Adv. Space Res., 17, 37–47, 1996.

Hoffmann, P., Rapp, M., Singer, W., and Keuer, D.: Trends of mesospheric gravity waves at northern middle latitudes during summer, J. Geophys. Res., 116, D00P08, doi:10.1029/2011JD015717, 2011.

Holdsworth, D. A., Morris, R. J., Murphy, D. J., Reid, I. M., Burns, G. B., and French, W. J. R.: Antarctic mesospheric temperature estimation using the Davis MST radar, J. Geophys. Res., 111, D05108, doi:10.1029/2005JD006589, 2006.

Holmen, S. E., Hall, C. M., and Tsutsumi, M.: Neutral atmosphere temperature change at 90 km, 70° N, 19° E, 2003–2014, Atmos. Chem. Phys. Discuss., 15, 15289–15317, doi:10.5194/acpd-15-15289-2015, 2015.

Jackman, C. H., DeLand, M. T., Labow, G. J., Fleming, E. L., Weisenstein, D. K., Ko, M. K. W., Sinnhuber, M., Anderson, J., and Russel, J. M.: The influence of the several very large solar proton events in years 2000–2003 on the middle atmosphere, Adv. Space Res., 35, 445–450, doi:10.1016/j.asr.2004.09.006, 2005.

Kolmogorov, A. N.: Dissipation of energy in the locally isotropic turbulence, Proc. USSR Academy of Sciences, 30, 299–303, 1941.

Kozubek, M., Krizan, P., and Lastovicka, J.: Northern Hemisphere stratospheric winds in higher midlatitudes: longitudinal distribution and long-term trends, Atmos. Chem. Phys., 15, 2203–2213, doi:10.5194/acp-15-2203-2015, 2015.

Krivolutsky, A. A., Klyuchnikova, A. V., Zakharov, G. R., Vyushkova, Y. T., and Kuminov, A. A.: Dynamical response of the middle atmosphere to solar proton event of July 2000: three dimensional model simulations, Adv. Space Res., 37, 1602–1613, doi:10.1016/j.asr.2005.05.115, 2006.

Kundu, P. K.: Fluid Mechanics, 638 pp., Academic Press, San Diego, USA, 1990.

Lübken, F.-J.: Nearly zero temperature trend in the polar summer mesosphere, Geophys. Res. Lett., 104, 9135–9149, 1999.

Manson, A. H. and Meek, C. E.: Climatologies of mean winds and tides observed by medium frequency radars at Tromsø (70N) and Saskatchewan (52N) during 1987–1989, Can. J. Phys., 69, 966–975, 1991.

Manson, A. H., Meek, C. E., Xu, X., Aso, T., Drummond, J. R., Hall, C. M., Hocking, W. K., Tsutsumi, M., and Ward, W. E.: Characteristics of Arctic winds at CANDAC-PEARL (80° N, 86° W) and Svalbard (78° N, 16° E) for 2006–2009: radar observations and comparisons with the model CMAM-DAS, Ann. Geophys., 29, 1927–1938, doi:10.5194/angeo-29-1927-2011, 2011.

McIntyre, M. E.: On dynamics and transport near the polar mesopause in summer, J. Geophys. Res., 94, 20841–20857, 1991.

McKinley, D. W. R.: Meteor Science and Engineering, 309 pp., McGrath-Hill, New York, 1961.

Oakey, N. S.: Determination of the rate of dissipation of turbulent energy from simultaneous temperature and velocity shear microstructure measurements, J. Phys. Oceanogr., 12, 256–271, 1982.

Offermann, D., Jarisch, M., Schmidt, H., Oberheide, J., Grossmann, K. U., Gusev, O., Russell III, J. M., and Mlynczak, M. G.: The "wave turbopause", J. Atmos. Sol.-Terr. Phy., 69, 2139–2158, 2007.

Offermann, D., Hoffmann, P., Knieling, P., Koppmann, R., Oberheide, J., and Steinbrecht, W.: Long-term trends and solar cycle variations of mesospheric temperature and dynamics, J. Geophys. Res., 115, D18127, doi:10.1029/2009JD013363, 2010.

Oliver, W. L., Holt, J. M., Zhang, S.-R., and Goncharenko, L. P.: Long-term trends in thermospheric neutral temperature and density above Millstone Hill, J. Geophys. Res.-Space, 119, 1–7, doi:10.1002/2014JA020311, 2014.

Pardyjak, E. R., Monti, P., and Fernando, H. J. S.: Flux Richardson number measurements in stable atmospheric shear flows, J. Fluid Mech., 459, 307–316, doi:10.1017/S0022112002008406, 2002.

Picone, J. M., Hedin, A. E., Drob, D. P., and Atkin, A. C.: NRLMSISE-00 empirical model of the atmosphere: statistical comparisons and scientific issues, J. Geophys. Res., 107, 1468, doi:10.1029/2002JA009430, 2002.

Pokhunkov, A. A., Rybin, V. V., and Tulinov, G. F.: Quantitative characteristics of long-term changes in parameter of the upper atmosphere of the Earth over the 1966–1992 period, Cosmic Res., 47, 480–490, 2009

Schlegel, K., Brekke, A., and Haug, A.: Some characteristics of the quiet polar D-region and mesosphere obtained with the partial reflection method, J. Atmos. Terr. Phys., 40, 205–213, 1978.

She, C.-Y., Krueger, D. A., and Yuan, T.: Long-term midlatitude mesopause region temperature trend deduced from quarter cen-

tury (1990–2014) Na lidar observations, Ann. Geophys., 33, 363–369, doi:10.5194/angeo-33-363-2015, 2015.

Shinbori, A., Koyama, Y., Nose, M., Hori, T., Otsuka, Y., and Yatagai, A.: Long-term variation in the upper atmosphere as seen in the geomagnetic solar quiet daily variation, Earth Planet. Space, 66, 155–175, doi:10.1186/s40623-014-0155-1, 2014.

Stray, N. H., Orsolini, Y. J., Espy, P. J., Limpasuvan, V., and Hibbins, R. E.: Observations of planetary waves in the mesosphere-lower thermosphere during stratospheric warming events, Atmos. Chem. Phys., 15, 4997–5005, doi:10.5194/acp-15-4997-2015, 2015.

Tiao, G. C., Reinsel, G. C., Xu, D., Pedrick, J. H., Zhu, X., Miller, A. J., DeLuisi, J. J., Mateer, C. L., and Wuebbles, D. J.: Effects of autocorrelation and temporal sampling schemes on estimates of trend and spatial correlation, J. Geophys. Res., 95, 20507–20517, 1990.

Thrane, E. V., Blix, T. A., Hall, C., Hansen, T. L., von Zahn, U., Meyer, W., Czechowsky, P., Schmidt, G., Widdel, H.-U., and Neumann, A.: Small scale structure and turbulence in the mesosphere and lower thermosphere at high latitudes in winter, J. Atmos. Terr. Phys., 49, 751–762, 1987.

Vandepeer, B. G. W. and Hocking, W. K.: A comparison of Doppler and spaced antenna radar techniques for the measurement of turbulent energy dissipation rates, Geophys. Res. Lett., 20, 17–20, 1993.

Weinstock, J.: Vertical turbulent diffusion in a stably stratified fluid, J. Atmos. Sci., 35, 1022–1027, 1978.

de Wit, R. J., Hibbins, R. E., Espy, P. J., and Hennum, E. A.: Coupling in the middle atmosphere related to the 2013 major sudden stratospheric warming, Ann. Geophys., 33, 309–319, doi:10.5194/angeo-33-309-2015, 2015.

Working, H. and Hotelling, H.: Application of the theory of error to the interpretation of trends, J. Am. Stat. Assoc., 24, 73–85, 1929.

Paper 4

Neutral atmosphere temperature trends and variability at 90 km, 70°N, 19°E, 2003–2014

Holmen, S. E., C. M. Hall and M. Tsutsumi

Published in Atmospheric Chemistry and Physics, 16, 7853-7866, doi: 10.5194/acp-16-7853-2016, 2016.

Atmos. Chem. Phys., 16, 7853–7866, 2016
www.atmos-chem-phys.net/16/7853/2016/
doi:10.5194/acp-16-7853-2016

Atmospheric Chemistry and Physics Open Access EGU

Neutral atmosphere temperature trends and variability at 90 km, 70° N, 19° E, 2003–2014

Silje Eriksen Holmen[1,2,3], **Chris M. Hall**[2], **and Masaki Tsutsumi**[4,5]

[1]The University Centre in Svalbard, Longyearbyen, Norway
[2]Tromsø Geophysical Observatory, UiT – The Arctic University of Norway, Tromsø, Norway
[3]Birkeland Centre for Space Science, Bergen, Norway
[4]National Institute of Polar Research, Tokyo, Japan
[5]The Graduate University for Advanced Studies (SOKENDAI), Department of Polar Science, Hayama, Japan

Correspondence to: Silje Eriksen Holmen (siljeh@unis.no)

Received: 28 April 2015 – Published in Atmos. Chem. Phys. Discuss.: 5 June 2015
Revised: 11 May 2016 – Accepted: 6 June 2016 – Published: 27 June 2016

Abstract. Neutral temperatures at 90 km height above Tromsø, Norway, have been determined using ambipolar diffusion coefficients calculated from meteor echo fading times using the Nippon/Norway Tromsø Meteor Radar (NTMR). Daily temperature averages have been calculated from November 2003 to October 2014 and calibrated against temperature measurements from the Microwave Limb Sounder (MLS) on board Aura. Large-scale periodic oscillations ranging from ∼9 days to a year were found in the data using Lomb–Scargle periodogram analysis, and these components were used to seasonally detrend the daily temperature values before assessing trends. Harmonic oscillations found are associated with the large-scale circulation in the middle atmosphere together with planetary and gravity wave activity. The overall temperature change from 2003 to 2014 is $-2.2\,\mathrm{K} \pm 1.0\,\mathrm{K\,decade^{-1}}$, while in summer (May–June–July) and winter (November–December–January) the change is $-0.3\,\mathrm{K} \pm 3.1\,\mathrm{K\,decade^{-1}}$ and $-11.6\,\mathrm{K} \pm 4.1\,\mathrm{K\,decade^{-1}}$, respectively. The temperature record is at this point too short for incorporating a response to solar variability in the trend. How well suited a meteor radar is for estimating neutral temperatures at 90 km using meteor trail echoes is discussed, and physical explanations behind a cooling trend are proposed.

1 Introduction

Temperature changes in the mesosphere and lower thermosphere (MLT) region due to both natural and anthropogenic variations cannot be assessed without understanding the dynamical, radiative and chemical couplings between the different atmospheric layers. Processes responsible for heating and cooling in the MLT region are many. Absorption of UV by O_3 and O_2 causes heating, while CO_2 causes strong radiative cooling. Planetary waves (PWs) and gravity waves (GWs) break and deposit heat and momentum into the middle atmosphere and influence the mesospheric residual circulation, which is the summer-to-winter circulation in the mesosphere. Also, heat is transported through advection and adiabatic processes.

For decades, it has been generally accepted that increased anthropogenic emissions of greenhouse gases are responsible for warming of the lower atmosphere (e.g. Manabe and Wetherald, 1975) and that these emissions are causing the mesosphere and thermosphere to cool (Akmaev and Fomichev, 2000; Roble and Dickinson, 1989). Akmaev and Fomichev (1998) report, using a middle atmospheric model, that if CO_2 concentrations are doubled, temperatures will decrease by about 14 K at the stratopause, by about 10 K in the upper mesosphere and by 40–50 K in the thermosphere. Newer and more sophisticated models include important radiative and dynamical processes as well as interactive chemistries. Some model results indicate a cooling rate near the mesopause lower than predicted by Akmaev and Fomichev (1998), while others maintain the negative signal

(French and Klekociuk, 2011; Beig, 2011). The thermal response in this region is strongly influenced by changes in dynamics, and some dynamical processes contribute to a warming which counteracts the cooling expected from greenhouse gas emissions (Schmidt et al., 2006).

Even though the increasing concentration of greenhouse gases is generally accepted to be the main driver, other drivers of long-term changes and temperature trends also exist, namely stratospheric ozone depletion, long-term changes of solar and geomagnetic activity, secular changes of the Earth's magnetic field, long-term changes of atmospheric circulation and mesospheric water vapour concentration (Laštovička et al., 2012). Dynamics may influence temperatures in the MLT region on timescales of days to months, and investigations of the influence of this variability on averages used for temperature trend assessments are important. The complexity of temperature trends in the MLT region and their causes act as motivation for studying these matters further.

In this paper, we investigate trend and variability of temperatures obtained from the Nippon/Norway Tromsø Meteor Radar (NTMR), and we also look at summer and winter seasons separately. In Sect. 2, specifications of the NTMR radar are given, and the theory behind the retrieval of temperatures using ambipolar diffusion coefficients from meteor trail echoes is explained. In Sect. 3, the method behind the calibration of NTMR temperatures against Aura MLS temperatures is explained. Section 4 treats trend analysis and analysis of variability and long-period oscillations in temperatures. The theory and underlying assumptions for the method used for determining neutral temperatures from meteor trail echoes, thus how well suited a meteor radar is for estimating such temperatures is discussed in Sect. 5. Also, physical explanations behind changes in temperature and observed temperature variability are discussed, as well as comparison with other reports on trends.

2 Instrumentation and data

The NTMR is located at Ramfjordmoen near Tromsø, at 69.58° N, 19.22° E. It is operated 24 h per day, all year round. Measurements are available for more than 90 % of all days since the radar was first operative in November 2003. The meteor radar consists of one transmitter antenna and five receivers and is operating at 30.25 MHz. It detects echoes from ionised trails from meteors, which appear when meteors enter and interact with the Earth's neutral atmosphere in the MLT region. The ionised atoms from the meteors are thermalised, and the resulting trails expand in the radial direction mainly due to ambipolar diffusion, which is diffusion in plasma due to interaction with the electric field. Underdense meteors, which are the ones used in this study, have a plasma frequency that is lower than the frequency of the radar, which makes it possible for the radio wave from the radar to penetrate into the meteor trail and be scattered by each electron.

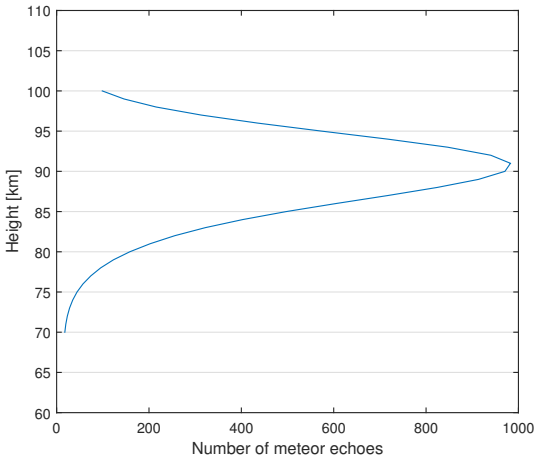

Figure 1. Vertical distribution of the occurrence of meteor echoes over Tromsø, averaged over height between 2003 and 2014. The peak occurrence height is just over 90 km altitude.

Echoes are detected from a region within a radius of approximately 100 km (horizontal space). The radar typically detects around 10 000 echoes per day, of which around 200–600 echoes are detected per hour at the peak occurrence height of 90 km. Figure 1 shows the vertical distribution of meteor echoes as a function of height, averaged over the time period 2003–2014. The number of echoes detected per day allows for a 30 min resolution of temperature values. The intraday periodicity in meteor detections by the NTMR radar is less pronounced than that of lower-latitude stations and we do not anticipate tidally induced bias regarding echo rates at specific tidal phases for daily averages. The height resolution and the range resolution are both 1 km, when looking at altitudes around the peak occurrence height. From the decay time of the radar signal we can derive ambipolar diffusion coefficients, D_a:

$$D_a = \frac{\lambda^2}{16\pi^2\tau}, \quad (1)$$

where λ is the radar wavelength and τ is the radar echo decay time. It has been shown that this coefficient also can be expressed in terms of atmospheric temperature and pressure:

$$D_a = 6.39 \times 10^{-2} K_0 \frac{T^2}{p}, \quad (2)$$

where p is pressure, T is temperature and K_0 is the zero-field reduced mobility factor of the ions in the trail. In this study we used the value for K_0 of $2.4 \times 10^{-4}\,\mathrm{m^2\,s^{-1}\,V^{-1}}$, in accordance e.g. with Holdsworth et al. (2006). Pressure values were derived from atmospheric densities obtained from falling sphere measurements appropriate for 70° N, combining those of Lübken and von Zahn (1991) and Lübken (1999), previously used by e.g. Holdsworth (2006) and Dyrland et al. (2010). These densities do not take into account long-term solar cycle variations.

The NTMR radar is essentially identical to the Nippon/Norway Svalbard Meteor Radar (NSMR) located in Advent Valley on Spitsbergen at 78.33° N, 16.00° E. Further explanation of the radar and explanation of theories can be found in e.g. Hall et al. (2002), Hall et al. (2012), Cervera and Reid (2000) and McKinley (1961).

Calibration of temperatures derived from meteor echoes with an independent, coinciding temperature series is necessary, according to previous studies (e.g. Hocking, 1999). Temperatures from the NSMR radar have been derived most recently by Dyrland et al. (2010), employing a new calibration approach for the meteor radar temperatures, wherein temperature measurements from the Microwave Limb Sounder (MLS) on the Aura satellite were used instead of the previously used rotational hydroxyl and potassium lidar temperatures from ground-based optical instruments (Hall et al., 2006). Neither ground-based optical observations nor lidar soundings are available for the time period of interest or the location of the NTMR. In this study we therefore employ the same approach as Dyrland et al. (2010), using Aura MLS temperatures to calibrate the NTMR temperatures.

NASA's EOS Aura satellite was launched 15 July 2004 and gives daily global coverage (between 82° S and 82° N) with about 14.5 orbits per day. The MLS instrument is one of four instruments on Aura and samples viewing forward along the spacecraft's flight direction, scanning its view from the ground to $\sim$ 90 km every $\sim$ 25 s, making measurements of atmospheric temperature, among others (NASA Jet Propulsion Laboratory, 2015).

Because of a general cooling of most of the stratosphere and mesosphere the last decades due to e.g. altered concentrations of CO_2 and O_3, the atmosphere has been shrinking, leading to a lowering of pressure surfaces at various altitudes. It is important to distinguish between trends on fixed pressure altitudes and fixed geometric altitudes, since trends on geometric altitudes include the effect of a shrinking atmosphere (Lübken et al., 2013). In this study, we have obtained Aura MLS temperature data (version 3.3) for latitude 69.7° N ± 5.0° and longitude 19.0° E ± 10.0° at 90 km geometric altitude.

3 Calibration of NTMR temperatures

Figure 2 shows daily NTMR temperatures from November 2003 to October 2014, derived from Eqs. (1) and (2), plotted together with Aura MLS temperatures. Standard error of the mean is omitted in the plot for better legibility, but typical standard error for daily temperatures is 0.2–0.6 K, highest in winter. The Aura satellite overpasses Tromsø at 01:00–03:00 and 10:00–12:00 UTC, which means that the Aura daily averages are representative for these time windows. It was therefore necessary to investigate any bias arising from Aura not measuring throughout the whole day. A way to do this is to

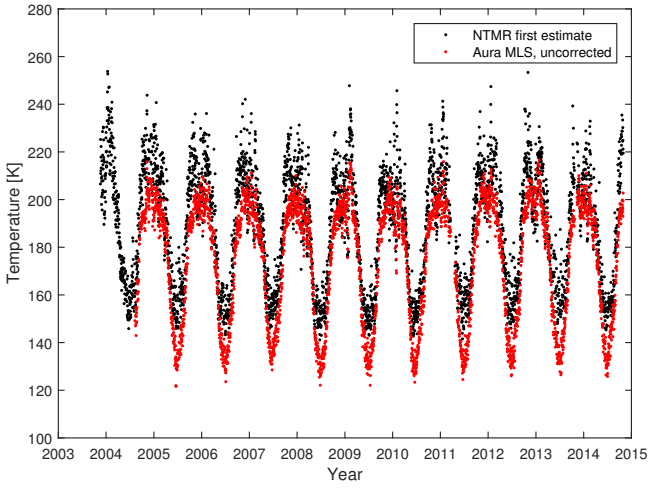

Figure 2. Daily values of NTMR temperatures derived from Eqs. (1) and (2) before correction for high D_a, plotted together with Aura MLS temperatures before applying any corrections.

assume that Aura temperatures and NTMR temperatures follow the same diurnal variation and thus investigate the diurnal variation of NTMR temperatures. This was done by superposing all NTMR temperatures by time of day, obtaining 48 values for each day, since the radar allows for a 30 min resolution.

There is an ongoing investigation into the possibility that D_a derived by NTMR can be affected by modified electron mobility during auroral particle precipitation. According to Rees et al. (1972), neutral temperatures in the auroral zone show a positive correlation with geomagnetic activity. It is therefore a possibility that apparent D_a enhancements during strong auroral events do not necessarily depict neutral temperature increase. This matter requires further attention.

Plotting hourly D_a values shows clear evening enhancements, especially during winter (not shown here). Investigation of possible unrealistic D_a enhancements was carried out by calculating standard errors of estimated hourly D_a values:

$$\mathrm{se} = \frac{\sigma}{\sqrt{\mathrm{ne}}}, \tag{3}$$

where σ is standard deviation and ne is the number of echoes detected by the radar. By examining and testing different rejection criteria, we arrived at a threshold of 7 % in standard error of hourly D_a values for identifying unrealistic enhancements. This rejection criterion led to that 5.4 % of the D_a values were rejected. NTMR temperatures after application of the D_a rejection procedure will hereafter be referred to as D_a-rejected NTMR temperatures.

Figure 3 shows monthly averages of the superposed values of D_a-rejected NTMR temperatures as a function of time of day for days coinciding with Aura measurements. It is evident from the figure that the lowest temperatures are in general achieved in the forenoon, which coincides with one of

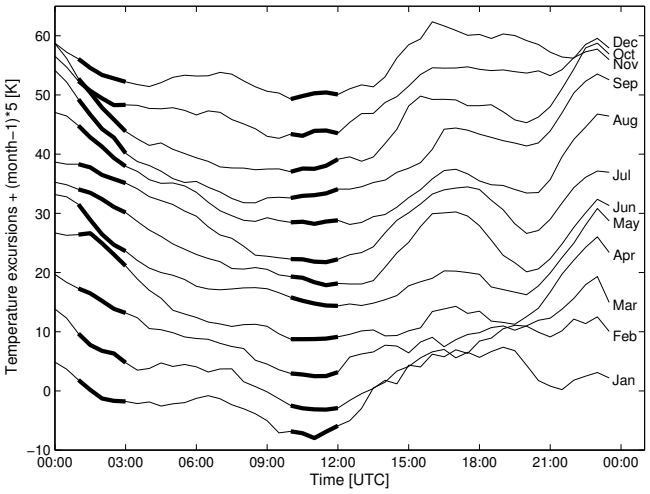

Figure 3. Monthly averages of diurnal temperature variation derived from NTMR after correction for high D_a at 90 km altitude. For clarity, time series are displaced by 5 K per month subsequent to January. The time of day corresponding to when Aura makes measurements over Tromsø (01:00–03:00 and 10:00–12:00 UTC) is highlighted.

the periods per day when Aura MLS makes measurements over Tromsø.

Subtracting monthly averages of the 00:00–24:00 UTC temperatures from the 01:00–03:00 and 10:00–12:00 UTC temperatures gave the estimated biases in Aura daily means due to only sampling during some hours of the day and are given in Table 1. By judging by the measurement windows, Aura underestimates the daily mean (00:00–24:00 UTC) more during winter than during spring and summer. Note the higher standard deviations in spring and summer compared with winter.

The initially obtained Aura temperatures were corrected by adding the biases from Table 1 in order to arrive at daily mean temperatures that were representative for the entire day. Also, the Aura temperatures were corrected for "cold bias". French and Mulligan (2010) report that Aura MLS temperatures exhibit a 10 K cold bias compared with OH*(6–2) nightly temperatures at Davis Station, Antarctica. A newer study by García-Comas et al. (2014) shows that Aura MLS exhibits a bias compared with several satellite instruments which varies with season. According to their findings, a 10 K correction for cold bias was applied to the Aura summer and winter temperatures (June–August, December–February), while a 5 K correction was applied to autumn and spring temperatures (September–November, March–May). The corrected Aura temperatures will hereafter be referred to as local time and cold bias-corrected Aura MLS temperatures.

Local time and cold bias-corrected Aura temperatures were plotted against D_a-rejected NTMR temperatures, and the linear fit ($R^2 = 0.83$) is described by:

$$T_{\mathrm{NTMR}} = 0.84\, T_{\mathrm{Aura}} + 32, \tag{4}$$

where T_{NTMR} is D_a-rejected temperature obtained from NTMR, and T_{Aura} is local time and cold bias-corrected temperature from Aura MLS. Inverting Eq. (4) enabled us to estimate NTMR temperatures calibrated with respect to Aura MLS temperatures. NTMR temperatures were now corrected for days of measurements coinciding with Aura measurements and are hereafter referred to as MLS-calibrated NTMR temperatures. For calibration of NTMR temperatures from November 2003 to August 2004 (before the beginning of the Aura MLS dataset), D_a-rejected NTMR temperatures were used as input to the inverted equation to arrive at calibrated NTMR temperatures.

To estimate the calibration uncertainty, all local time and cold bias-corrected Aura temperatures were subtracted from the MLS-calibrated NTMR temperatures, and the differences were plotted in a histogram with 5 K bins (not shown here). A Gaussian was fitted to the distribution. The standard deviation of the Gaussian was 11.9 K, which is considered to be the overall uncertainty of the calibration. Finally, Fig. 4 shows the MLS-calibrated NTMR temperatures with uncertainties plotted together with Aura MLS temperatures, corrected for cold and time-of-day measurement bias.

4 Results

Weatherhead et al. (1998) discuss the effects of autocorrelation and variability on trend estimation and emphasise that changes in environmental variables are often modelled as being a linear change, even though there may be a high degree of periodic variation within the data in addition to the linear trend. A linear trend model assumes that measurements of the variable of interest at time t can be expressed as follows:

$$Y_t = \mu + S_t + \omega L_t + N_t, \tag{5}$$

where μ is a constant term, S_t is a seasonal component, L_t is the linear trend function, ω is the magnitude of the trend and N_t is noise. N_t may be autocorrelated and the result of various natural factors, which give rise to somewhat smoothly varying changes in N_t over time. Such natural factors may not always be known or measurable.

Taking this into account, variability of the data was explored before assessing the linear trend of the temperature data. In Sect. 4.1, a Lomb–Scargle periodogram analysis is conducted, and periodic components in the data are identified before assessing the trend, while in Sect. 4.2 solar cycle dependence is briefly explored, even though the temperature record is too short for this to be incorporated in the trend analysis.

Table 1. Bias/overestimate expected from Aura monthly averages due to Aura MLS only measuring between 01:00 and 03:00 UTC and between 10:00 and 12:00 UTC.

Month	Jan	Feb	Mar	Apr	May	Jun	Jul	Aug	Sep	Oct	Nov	Dec
Aura bias (K)	−6.3	−6.5	−3.3	−0.08	−0.5	−0.6	−1.4	−1.3	−2.7	−3.5	−3.9	−4.6
σ (K)	3.2	4.7	6.0	8.1	6.6	7.1	7.5	6.7	6.0	5.3	2.6	1.8

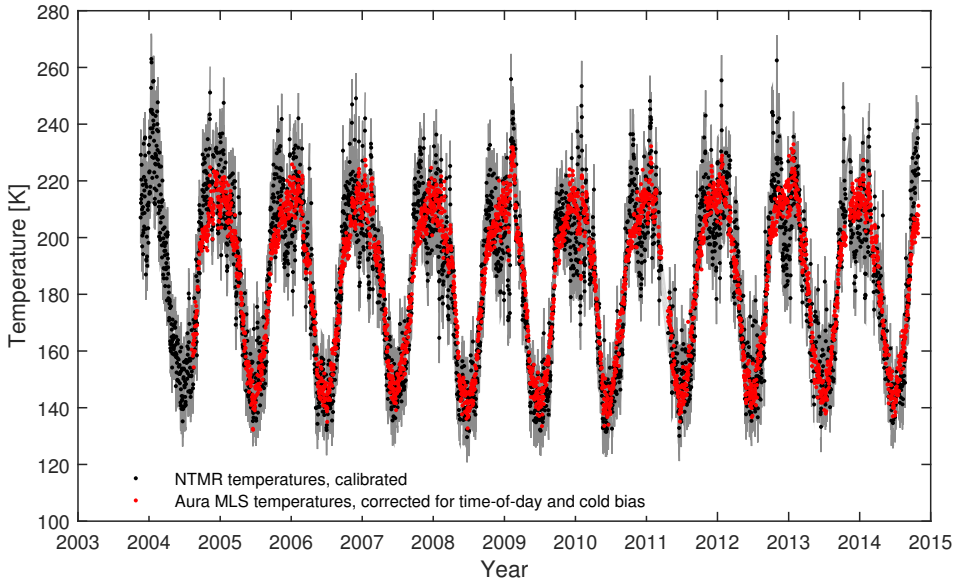

Figure 4. Daily values of MLS-calibrated NTMR temperatures plotted together with Aura MLS temperatures corrected for cold and time-of-day bias. The overall calibration uncertainty is indicated by the grey shading.

4.1 Estimation of periodic variability and trend

To identify periodic variability, a Lomb–Scargle (LS) periodogram analysis was applied to the MLS-corrected NTMR temperatures (Press and Rybicki, 1989). LS analysis is a modified discrete Fourier transform algorithm suitable for unevenly spaced data. Figure 5 (upper panel) shows the LS periodogram, identifying a particularly strong annual (A) component, but also a semi-annual (A/2) and two sub-annual peaks (A/3 and A/4), significant at the 99 % level.

Following the procedure of Niciejewski and Killeen (1995), the daily temperatures were fit to the following approximation:

$$T_{\mathrm{NTMR}}(t) = T_0 + \sum_i \left(d_i \sin \frac{2\pi}{p_i} t + e_i \cos \frac{2\pi}{p_i} t \right) + Lt, \quad (6)$$

where $T_{\mathrm{NTMR}}(t)$ is observed daily temperature, T_0 is the average temperature, i is the number of harmonic components found in the LS analysis, d_i and e_i are the amplitudes of the ith harmonic component, p_i is the period of the ith harmonic component and t is the day number. L represents the trend. The average temperature over the 11-year period, T_0, was found to be 189.4 ± 0.6 K.

It has been shown that the confidence levels in the periodogram are only strictly valid for the peak with the highest spectral power (Scargle, 1982). Thus, there may be peaks significant at the 95 % level even though they are not noticeable in the periodogram, due to their variance being overestimated by the presence of the larger peaks. Therefore, after fitting the primary periodic components with significance better than the 99 % level to the NTMR temperatures using Eq. (6), LS analysis was repeated on the temperature residuals to check for additional significant periodic components in the data. Horne and Baliunas (1986) point out that the periodogram power needs to be normalised by the total variance of the data in order to obtain spectral peaks with correct magnitude. The variance of the data was therefore adjusted to maintain the correct probability distribution of the periodogram. Figure 5 (lower panel) shows spectral power of harmonics found at better than 95 % significance level of residuals obtained after fitting the sinusoids of the four largest peaks. The apparently significant peaks located near 91, 121, 184 and 363 days, even though these harmonics have been filtered out at this stage, are due to spectral leakage, which means that for a sinusoidal signal at a given frequency, ω_0, the power in the periodogram not only appears at ω_0, but also leaks to other nearby frequencies (Scargle, 1982). All periodic components

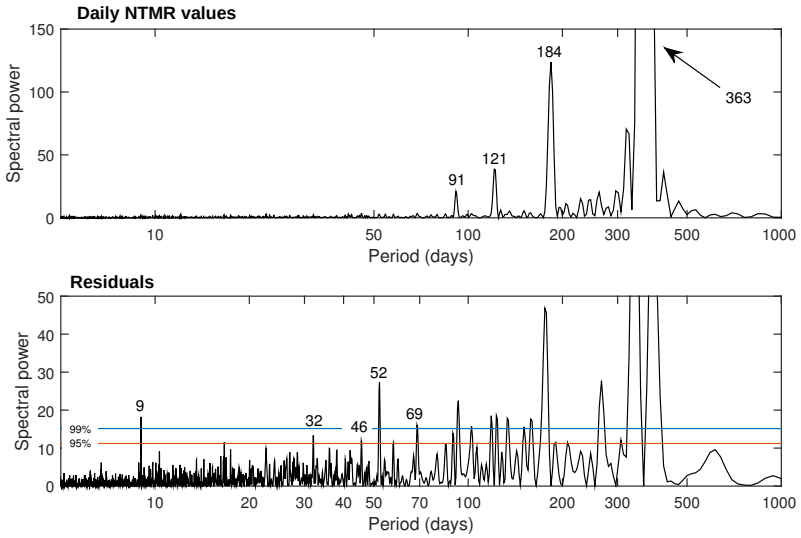

Figure 5. Upper panel: Lomb–Scargle periodogram for daily NTMR temperatures from 2003 to 2014. The y axis has been truncated for clarity. Lower panel: periodogram for residuals after fitting sinusoids for the four largest peaks from the upper panel. Peaks significant at better than 95 % are marked with numbers corresponding to period.

Table 2. Periodic components found in data using Lomb–Scargle periodogram analysis. All components were identified as better than the 99 % significance level, except for the 32-day harmonic, which was significant at the 95 % level. Amplitudes are given with 95 % confidence bounds.

Periodic component (days)	Amplitude (K)
363	21.5 ± 0.4
184	6.5 ± 0.4
121	3.8 ± 0.4
91	2.9 ± 0.4
69	1.2 ± 0.4
52	1.5 ± 0.4
46	1.1 ± 0.4
32	0.9 ± 0.4
9.0	1.0 ± 0.4

found at better than 95 % significance and their amplitudes are listed in Table 2.

The trend was estimated from the approximation in Eq. (6) to be $-2.2\,\mathrm{K} \pm 1.0\,\mathrm{K\,decade^{-1}}$. From Tiao et al. (1990), this trend can be considered significantly non-zero at the 5 % level, since the uncertainty ($2\sigma = 2.0\,\mathrm{K\,decade^{-1}}$) is less than the trend itself. We estimated the number of years for which a trend can be detectable, following the formulation of Weatherhead et al. (1998):

$$n^* \approx \left(\frac{3.3\sigma_N}{|\omega_0|} \sqrt{\frac{1+\varphi}{1-\varphi}} \right)^{2/3}, \quad (7)$$

where n^* is the number of years required, ω_0 is the magnitude of the trend per year, σ_N is the standard deviation of noise N and φ is the autocorrelation function of the noise at lag 1. The value 3.3 corresponds to a 90 % probability that the trend is detectable after n^* years. Solving Eq. (7) reveals that the minimum number of years required for detecting a decadal trend of -2.2 K is about 17 years.

The resulting composite of the least-squares fit is shown in Fig. 6, together with the MLS-corrected NTMR temperatures. We see that the smooth curve represents the periodicity in the data to a good extent, but there is still variability not accounted for. Temperature residuals obtained after subtracting the MLS-calibrated NTMR temperatures from the fit in Fig. 6 are henceforth referred to as fit residuals.

In addition to the harmonics listed in Table 2, we found a harmonic of $\sim$615 days (see Fig. 5, lower panel), which was not statistically significant. We also found a $\sim$17-day oscillation, significant at the 95 % level (see Fig. 5, lower panel), but the amplitude of this component was found to be close to 0 K. The 615-day and 17-day periodic components were therefore not incorporated in the composite fit.

In Fig. 7, all individual years are superposed by day of year. This was done to better visualise the variability of an average year. In addition to the broad maximum in temperatures during winter and the narrower minimum during summer, we see minor enhancements just after the spring equinox (day of year $\sim$100) and summer solstice (day of year $\sim$210) and also a local minimum in early winter. Explanations for the variability will be discussed in Sect. 5.1.

In addition to the average temperature change, we also treated summer and winter seasons separately. First, monthly averages of the temperature residuals were calculated and

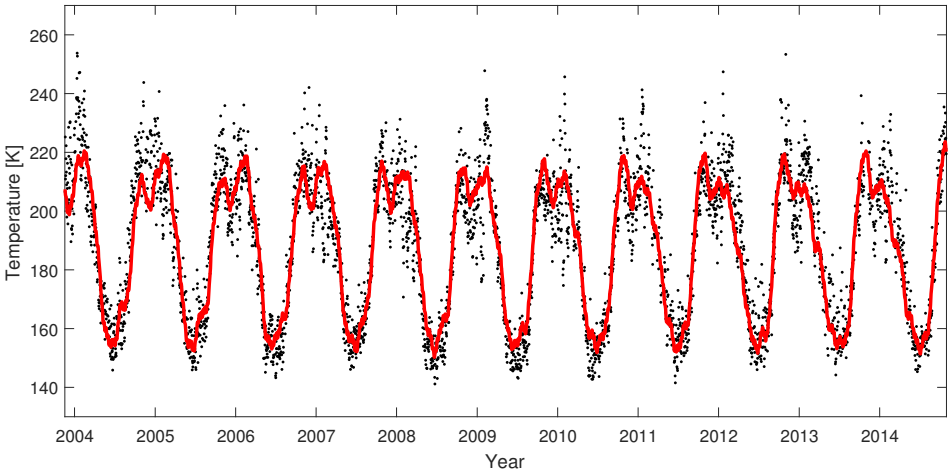

Figure 6. MLS-corrected NTMR daily temperatures (black dots) and the least-squares fit of the average, trend and periodic components (red curve).

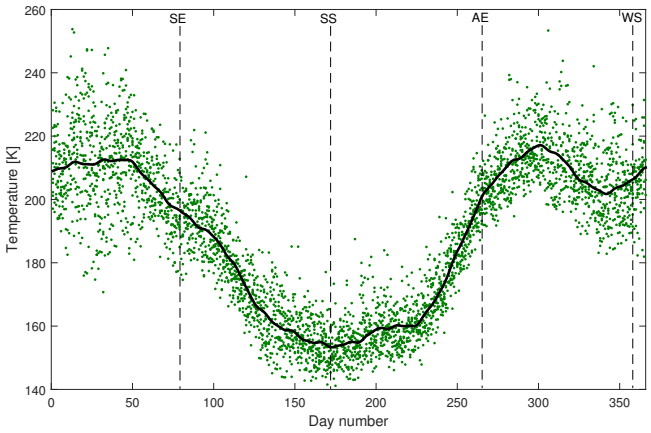

Figure 7. Superposed-epoch analysis of daily MLS-corrected NTMR temperatures. The smooth, black line is the composite fit of all periodic components listed in Table 2. Spring and autumn equinoxes and winter and summer solstice are marked SE, AE, WS and SS, respectively.

trends for each month were investigated. Figure 8 shows the result. Then, averages of November, December and January and of May, June and July were made. As opposed to the meteorological seasons as experienced in the troposphere, we have chosen to define "winter" and "summer" as the three months centred on the respective solstices. However, since the meteorological winter and summer are defined differently, we will refer to these trends as NDJ and MJJ trends. The linear NDJ trend is $-11.6\,\mathrm{K} \pm 4.1\,\mathrm{K\,decade}^{-1}$, and the MJJ trend is $-0.3\ \mathrm{K} \pm 3.1\,\mathrm{K\,decade}^{-1}$. Solving Eq. (7) for NDJ and MJJ trends reveals a minimum length for trend detection of 10.8 and 63 years, respectively.

The trend analysis was also performed without carrying out the D_a rejection procedure explained in Sect. 3. Final results of the trend analysis, both when excluding and including rejection of D_a values due to hypothetical anomalous electrodynamic processes, do not differ significantly. It is reasonable to believe that strong geomagnetic conditions can affect derived temperatures on a short timescale. However, due to the considerable quantity of data employed in this study, it is inconceivable that this effect will change the conclusions regarding trends, as our results also show.

4.2 Exploration of solar flux dependence

Our dataset covers 11 years of meteor radar temperatures and thus it is shorter than the corresponding solar cycle (which was somewhat longer than the average 11 years). Even though it is premature to apply solar cycle analysis to a time series this short, we will briefly explore and present our temperature data together with solar variability. In this study we use the F10.7 cm flux as a proxy for solar activity, which is the most commonly used index in middle/upper atmospheric temperature trend studies (e.g. Laštovicka et al., 2008; Hall et al., 2012).

Figure 9 shows yearly values of F10.7 cm plotted against yearly averaged fit residual temperatures. For clarity, black bullets corresponding to years are connected with lines, making it easier to see the progression from high solar flux to solar minimum and back to solar maximum. We see that, to some extent, there is a conjunction between low solar flux values and negative temperature fit residuals. For the years 2006–2010, which were years of solar minimum, fit residuals were on average negative. For the years 2005 and 2011, which were years in between solar maximum and minimum, fit residuals were close to zero. However, for years with higher F10.7 values the tendency of increasing fit residuals is less distinct. Ogawa et al. (2014) find a non-linear relationship between upper-atmospheric temperatures and solar activity using EISCAT UHF (ultra-high frequency) radar ob-

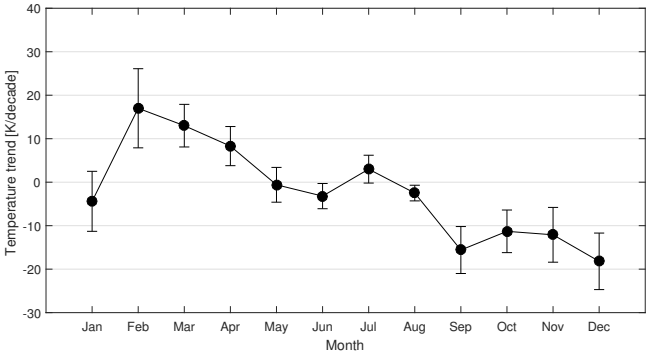

Figure 8. Monthly temperature trends at 90 km altitude over Tromsø. Standard deviations are given as error bars.

servations from 200 to 450 km altitude over Tromsø, even though it must be noted that the altitude range they look at differs from ours.

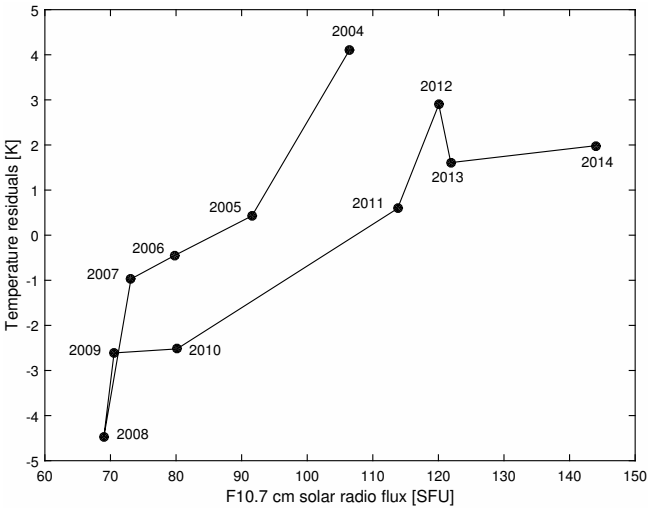

Figure 9. Yearly values of F10.7 cm solar radio flux plotted against yearly averaged temperature fit residuals. Year 2003 is left out of the figure due to the data coverage (only data for November and December).

5 Discussion

Statistically significant periodic components found in the temperature data are annual (A) and semi-annual (A/2) oscillations, and 121- (A/3), 91- (A/4), 69- (A/5), 52- (A/7), 46- (A/8), 32- and 9-day oscillations. Temperature change from 2003 to 2014 is $-2.2\,\mathrm{K} \pm 1.0\,\mathrm{K\ decade}^{-1}$, and MJJ and NDJ trends are $-0.3\,\mathrm{K} \pm 3.1$ and $-11.6\,\mathrm{K} \pm 4.1\,\mathrm{K\ decade}^{-1}$, respectively. Explanations for the periodic variability will be proposed in Sect. 5.1. In Sect. 5.2, physical explanations for the temperature change will be explored, and our results will be compared with other reports on mesospheric trends at high and midlatitudes. Trends will be discussed in terms of the method used for deriving temperatures in Sect. 5.3.

5.1 Mechanisms for the observed variability and harmonics

The A, A/2, A/3, A/4, A/5, A/7 and A/8 components are also found for OH* temperatures over other mid- and high-latitude sites (e.g. Espy and Stegman, 2002; Bittner et al., 2000; French and Burns, 2004). In addition to these components, A/6 and A/9 sub-annual harmonics, as well as other shorter-period components, have been identified in other datasets (e.g. Bittner et al., 2000; French and Burns, 2004).

Espy and Stegman (2002) attribute the asymmetry with the broad winter maximum and the narrow summer minimum to the A/2 harmonic, and the temperature enhancements during the equinoxes to the A/3 and A/4 harmonics.

French and Burns (2004) identify the visible variations of the 52-day (A/7) component in their data from Davis, Antarctica, and find this component's phase to be "locked" to the day of year, indicating a seasonal dependence. Espy and Stegman (2002) only find this component as a result of LS analysis of their superposed-epoch data, also indicating that the phase is locked to the day of year. French and Burns (2002) and Bittner et al. (2000) find in general strong differences from year to year in the significant oscillations observed. We have not carried out analysis of the year-to-year variation in oscillations observed, but considering, e.g. the uneven occurrences of SSWs (sudden stratospheric warnings), we have no reason to conclude otherwise regarding our data.

The $\sim$9-day oscillation we find in our data can most likely be designated to travelling planetary waves, which have typical periods of 1–3 weeks, with 8–10 days as a prominent period (Salby, 1981a, b).

The $\sim$615 day periodic component (not statistically significant) may at first glance seem to be somehow related to the quasi-biennial oscillation (QBO), which is a system where zonal winds in the lower equatorial stratosphere alternate between westward (easterly) and eastward (westerly) with a mean period of 28–29 months. Also other studies find a $\sim$2 year periodic component in their temperature data, attributed to a QBO effect (Espy and Stegman, 2002; Bittner et al., 2000; French and Burns, 2004 – the two latter give statistically inconclusive results). However, our $\sim$615 day component is quite far from the mean period of the QBO. That, in addition to it not being significant, makes it difficult to interpret.

The higher temperature variability during winter compared with summer, visible in Fig. 7, is also found in other datasets at mid- and high latitudes (e.g. Espy and Stegman, 2002; Bittner et al., 2000). This feature and the observations of local temperature enhancement around day 200 as well as the reduction of the strong, negative seasonal gradient just after the spring equinox can be explained by the state of the

background wind system in the middle atmosphere and the corresponding propagation of planetary and gravity waves. Enhanced GW and PW flux and momentum into the mesosphere lead to enhanced turbulent diffusion, which can result in increased temperatures. PWs can only propagate westward and against the zonal flow, so easterly winds in the middle atmosphere during summer are blocking vertical propagation of long-period PWs into the MLT region. In contrast, during winter stratospheric zonal winds are westerly, favouring PW propagation. The presence of upward-propagating PWs during winter is therefore an explanation for the higher variability during this season.

GWs can propagate both eastward and westward, but only against the zonal flow, implying the presence of eastward-propagating GWs during summer and westward-propagating GWs during winter. The extratropical meso- and stratospheric zonal winds are very weak and change direction during the equinoxes, resulting in a damping of both westward- and eastward-propagating GWs during these periods (Hoffmann et al., 2010). Enhanced PW activity is observed at the same time (Stray et al., 2014). Temperature enhancements after the spring equinox are related to the final breakdown of the polar vortex or the last stratospheric warming event (Shepherd et al., 2002). Several studies have observed a "springtime tongue" of westward flow between 85 and 100 km, occurring approximately from day 95 to 120, reflecting the final warming (e.g. Hoffmann et al., 2010; Manson et al., 2002). The final warming is characterised by forced planetary Rossby waves that exert a strong westward wave drag from the stratosphere up to 100 km.

Enhanced PW activity has also been observed during midsummer, due to interhemispheric propagation of PWs into the summer mesopause (Stray et al., 2014; Hibbins et al., 2009). Also, enhanced short-period GW activity has been observed during summer (Hoffmann et al., 2010). Increased temperatures during midsummer may thus be a result of the combined effect of upward-propagating GWs and interhemispheric propagation of PWs.

Several studies have identified large temperature amplitude perturbations during the autumn equinox in particular (Taylor et al., 2001; Liu et al., 2001). The same signature is hard to find in our data. Hoffmann et al. (2010) find latitudinal differences in the amplitude of the semidiurnal meridional tide during the autumn equinox, observing stronger tidal amplitudes at Juliusruh (55° N, 13° E) compared with Andenes (69° N, 16° E). Manson et al. (2009) also find longitudinal differences in tides at high latitudes. Reasons for not observing increased temperatures around the autumn equinox are not clear, and further investigations are needed in order to make conclusions.

The local temperature minimum in early winter is also seen in other temperature data from mid- and high latitudes (e.g. French and Burns, 2004; Holmen et al., 2013; Shepherd et al., 2004). French and Burns (2004) find a decrease in large-scale wave activity during midwinter which they associate with the observed temperature minimum, but identify this as a Southern Hemisphere phenomenon. Shepherd et al. (2004) attribute the decrease in temperature to early winter warming of the stratosphere, characterised by the growth of upward-propagating PWs from the troposphere which decelerate/reverses the eastward stratospheric jet, resulting in adiabatic heating of the stratosphere and adiabatic cooling of the mesosphere. However, Shepherd et al. used temperature data from 1991 to 1999, which is prior to the start of our temperature record, and timings of SSWs are different from year to year. We investigated the timing and occurrence of SSW events during the last decade using NASA reanalysis temperatures and zonal winds provided through the Modern-Era Retrospective analysis for Research and Applications (MERRA) project (NASA, 2016). Most SSWs occurring between 2003 and 2014 start in the beginning of January or mid-January. One exception is the major warming in 2003–2004, in which zonal winds started to decelerate in mid-December. There are signs of a minor warming in the transition between November and December 2012, but there is not enough evidence to conclude that the local minimum of NTMR temperatures starting in early November is associated with early winter warming of the stratosphere. It is more likely that the pronounced variability in temperatures we see in January and February (days $\sim$0–50) in Fig. 7 is a manifestation of the SSW effect.

5.2 Physical explanations for cooling and comparison with other studies

Other studies on long-term mesospheric temperature trends from mid and high latitudes yield mostly negative or near-zero trends. Few studies cover the same time period as ours, and few are from locations close to Tromsø. Hall et al. (2012) report a negative trend of $-4\,\mathrm{K} \pm 2\,\mathrm{K\,decade^{-1}}$ for temperatures derived from the meteor radar over Longyearbyen, Svalbard (78° N, 16° E) at 90 km height over the time period 2001 to 2011, while Holmen et al. (2014) find a near-zero trend for OH* airglow temperatures at $\sim$87 km height over Longyearbyen over the longer time period 1983 to 2013. Offermann et al. (2010) report a trend of $-2.3\,\mathrm{K} \pm 0.6\,\mathrm{K\,decade^{-1}}$ for $\sim$87 km height using OH* airglow measurements from Wuppertal (51° N, 7° E). It must be noted that the peak altitude of the OH* airglow layer can vary and thus affect the comparability of OH* airglow temperature trends and meteor radar temperature trends. Winick et al. (2009) report that the OH* airglow layer can range from 75 to $>$ 90 km, while the newer study by von Savigny (2015) indicates that the layer height at high latitudes is remarkably constant from 2003 to 2011. Beig (2011) report that most recent studies on mesopause region temperature trends show weak negative trends, which is in line with our results.

According to the formulation by Weatherhead et al. (1998), our time series is not long enough for significant trend detection. We need another $\sim$6 years of data before a

trend of magnitude $-2.2\,\mathrm{K} \pm 1.0\,\mathrm{K\,decade}^{-1}$ is significant. Response to solar variability has not been taken into account due to the length of the temperature record. Our slightly negative overall trend must therefore be considered tentative. The summer trend requires many more years of data before it can be considered significant, because is a near-zero trend. However, the winter trend can be considered detectable and also significantly different from zero, following the criteria from Weatherhead et al. (1998) and Tiao et al. (1990).

Our results indicate a cooling at 90 km altitude over Tromsø in winter. A general cooling of the middle atmosphere will cause a contraction of the atmospheric column, hence a lowering of upper-mesospheric pressure surfaces. The pressure model used as input to Eq. (2) is only seasonally dependent, so a possible trend in pressure at 90 km must be addressed. By looking at Eq. (2), it is evident that if pressure decreases, temperature will decrease even more. Incorporating a decreasing trend in the pressure model will then serve to further strengthen the negative temperature trend we observe.

It has been proposed that GWs may be a major cause of negative temperature trends in the mesosphere and thermosphere (Beig, 2011; Oliver et al., 2013). GWs effectively transport chemical species and heat in the region, and increased GW drag leads to a net effect of cooling above the turbopause (Yigit and Medvedev, 2009). GWs are shown to heat the atmosphere below about 110 km altitude, while they cool the atmosphere at higher altitudes by inducing a downward heat flux (Walterscheid, 1981). However, there are large regional differences regarding trends in GW activity. Hoffmann et al. (2011) find an increasing GW activity in the mesosphere in summer for selected locations, but Jacobi (2014) finds larger GW amplitudes during solar maximum and relates this to a stronger mesospheric jet during solar maximum, both for winter and summer. Since we have not conducted any gravity wave trend assessment in this study, we cannot conclude that GW activity is responsible for the negative temperature trend, but we cannot rule out its role either.

The stronger cooling trend for winter is also consistent with model studies. Schmidt et al. (2006) and Fomichev et al. (2007) show, using the HAMMONIA and CMAM models, respectively, that a doubling of the CO_2 concentration will lead to a general cooling of the middle atmosphere, but that the high-latitude summer mesopause will experience insignificant change or even slight warming. They propose that this is the result of both radiative and dynamical effects. In summer, the CO_2 radiative forcing is positive due to heat exchange between the cold polar mesopause and the warmer, underlying layers. Also, CO_2 doubling alters the mesospheric residual circulation. This change is caused by a warming in the tropical troposphere and cooling in the extratropical tropopause, leading to a stronger equator-to-pole temperature gradient and hence stronger midlatitude tropospheric westerlies. This causes the westerly gravity wave drag to weaken, resulting in decreased adiabatic cooling from a slower ascent of the upper-mesospheric circulation. However, it must be noted that our strong, negative NDJ trend may differ from a trend estimated for meteorological winter months.

5.3 Suitability of a meteor radar for estimation of neutral temperatures at 90 km height

As explained in Sect. 2, neutral air temperatures derived from meteor trail echoes depend on pressure, p, the zero-field reduced mobility of the ions in the trail, K_0, and ambipolar diffusion coefficients, D_a. K_0 will depend on the ion composition in the meteor trail, as well as the chemical composition of the atmosphere. The chemical composition of the atmosphere is assumed to not change significantly with season (Hocking, 2004). Unfortunately, the exact content of a meteor trail is unknown. Usually, a value for K_0 between 1.9×10^{-4} and $2.9 \times 10^{-4}\,\mathrm{m^2\,s^{-1}\,V^{-1}}$ is chosen, depending on what ion one assumes to be the main ion of the trail (Hocking et al., 1997). Even though we in this study have chosen a constant value for K_0 of $2.4 \times 10^{-4}\,\mathrm{m^2\,s^{-1}\,V^{-1}}$, some variability in K_0 is expected. According to Hocking (2004), variability can occur due to fragmentation of the incoming meteoroid, anisotropy in the diffusion rate, plasma instabilities and variations in the composition of the meteor trail. Using computer simulations, they report a typical variability in K_0 from meteor to meteor of 27 % and that the variability is most dominant at higher temperatures. Based on this, we cannot rule out sources of error due to the choice of K_0 as a constant, but since we have no possibility to analyse the composition of all meteor trails detected by the radar, we have no other choice than to choose a constant value for K_0.

How well ambipolar diffusion coefficients obtained for 90 km altitude are suited for calculating neutral temperatures has previously been widely discussed, e.g. by Hall et al. (2012) for the trend analysis of Svalbard meteor radar data, but will be shortly repeated here. For calculations of temperatures using meteor radar, ambipolar diffusion alone is assumed to determine the decay of the underdense echoes. Diffusivities are expected to increase exponentially with height through the region from which meteor echoes are obtained (Ballinger et al., 2008; Chilson et al., 1996). Hall et al. (2005) find that this is only the case between ~ 85 and ~ 95 km altitude, using diffusion coefficients delivered by NTMR from 2004. They find diffusivities less than expected above ~ 95 km and diffusivities higher than expected below ~ 85 km. Ballinger et al. (2008) obtain a similar result using meteor observations over northern Sweden. It has been proposed that processes other than ambipolar diffusion influence meteor decay times. If this is the case it may have consequences for the estimation of temperatures, and therefore it is important to investigate this further.

Departures of the anticipated exponential increase with height of molecular diffusion above ∼ 95 km in previous studies are attributed to the gradient-drift Farley–Buneman instability. The Farley–Buneman instability occurs where the trail density gradient and electric field are largest. Due to frequent collisions with neutral particles, electrons are magnetised while ions are left unmagnetised, causing electrons and ions to differ in velocity. Electrons then create an electric field perpendicular to the meteor trail, leading to anomalous fading times that can be an order of magnitude higher than those expected from ambipolar diffusion. The minimum altitude at which this occurs depends on the trail altitude, density gradient and latitude, and at high latitudes this altitude is ∼ 95 km. Therefore, using ambipolar diffusion rates to calculate trail altitudes above this minimum altitude may lead to errors of several kilometres, since the diffusion coefficients derived from the measurements are underestimated (Ballinger et al., 2008; Dyrud et al., 2001; Kovalev et al., 2008).

Reasons for the higher-than-expected diffusivities below ∼ 85 km are not completely understood, according to theory. Hall (2002) proposes that neutral turbulence may be responsible for overestimates of molecular diffusivity in the region ∼ 70–85 km, but this hypothesis is rejected by Hall et al. (2005) due to a lacking correlation between neutral air turbulent intensity and diffusion coefficients delivered by the NTMR radar. Other mechanisms for overestimates of molecular diffusivity include incorrect determination of echo altitude and fading times due to limitations of the radar (Hall et al., 2005).

Since the peak echo occurrence height is 90 km and this is also the height at which a minimum of disturbing effects occur, 90 km height is therefore considered the optimal height for temperature measurements using meteor radar. Ballinger et al. (2008) report that meteor radars in general deliver reliable daily temperature estimates near the mesopause using the method outlined in this study, but emphasise that one should exercise caution when assuming that observed meteor echo fading times are primarily governed by ambipolar diffusion. They propose, after Havnes and Sigernes (2005), that electron–ion recombination can impact meteor echo decay times. This can especially affect the weaker echoes, hence this effect can lead to an underestimation of temperatures.

Determination of temperatures from meteor radar echo times is a non-trivial task, mainly because the calculation of ambipolar diffusion coefficients depends on the ambient atmospheric pressure. By using radar echo decay times to calculate ambipolar diffusion coefficients from Eq. (1), we can get an estimate for T^2/p from Eq. (2). Input of pressure values into the equation will thus provide atmospheric temperatures. However, measurements of pressure are rare and difficult to achieve at 90 km height, and often one has to rely on model values. Traditionally, pressure values at 90 km have been calculated using the ideal gas law, taking total mass density from atmospheric models, e.g. the Mass Spectrometer and Incoherent Scatter Radar (MSIS) models, where the newest version is NRLMSISE-00. It is hard to verify the pressure values derived from the models because of lack of measurements to compare the model to; hence using the pressure values may result in uncertainties of estimated atmospheric temperatures. In this study, we obtained pressure values from measurements of mass densities obtained from falling spheres combined with sodium lidar from Andøya (69° N, 15.5° E) (Lübken, 1999; Lübken and von Zahn, 1991). All measurements have been combined to give a yearly climatology, that is, one pressure value for each day of the year. Since Andøya is located in close proximity to Tromsø (approximately 120 km), the pressure values are considered appropriate for our calculations of neutral temperatures. One disadvantage with using pressure values obtained from the falling sphere measurements is that no day-to-day variations are taken into account, only the average climatology.

6 Conclusions

A number of long-period oscillations ranging from ∼ 9 days to a year were found in the NTMR temperature data. Temperature variability observed may, to a large extent, be explained by the large-scale circulation of the middle atmosphere and the corresponding activity in waves propagating from below. Higher temperature variability in winter is due to the presence of upward-propagating PWs during this season, in contrast to summer, when easterly winds in the middle atmosphere are blocking vertical propagation of long-period PWs into the MLT region. The variability is particularly high in January and February, which are periods where SSW events occur frequently. In addition to the general maximum of temperatures in winter and minimum in summer, our data show a local temperature enhancement around day 210, a local minimum in early winter and reduction of the strong, negative seasonal gradient after the spring equinox. The reduction of the strong, negative seasonal gradient after the spring equinox is related to the final breakdown of the polar vortex (Shepherd et al., 2002), while the increase during summer is most likely associated with a combined effect of upward-propagating GWs and interhemispheric propagation of PWs (Stray et al., 2014; Hoffmann et al., 2010). No evident reason can be found for the local temperature minimum in early winter or the fact that we do not see enhanced temperatures during the autumn equinox, as identified by others (e.g. Taylor et al., 2001; Liu et al., 2001).

The trend for NTMR temperatures at 90 km height over Tromsø was found to be $-2.2\,\mathrm{K} \pm 1.0\,\mathrm{K\,decade^{-1}}$. Summer (May, June, July) and winter (November, December, January) trends are $-0.3\,\mathrm{K} \pm 3.1$ and $-11.6\,\mathrm{K} \pm 4.1\,\mathrm{K\,decade^{-1}}$, respectively. Following the criterion from Weatherhead et al. (1998), the temperature record is only long enough for the NDJ trend to be con-

sidered detectable. Response to solar variability was not incorporated in the trend, due to the time series being shorter than the corresponding solar cycle. However, when looking at the progression from high solar flux to solar minimum and back to solar maximum we see, to some extent, that there is a conjunction between low solar flux values and negative temperature fit residuals and vice versa.

A weak overall cooling trend is in line with other recent studies on mesopause region temperature trends. A cooling of the middle atmosphere will cause a lowering of upper-mesospheric pressure surfaces. By implementing a negative trend in pressure at 90 km into the equation that we use for estimating temperatures, the negative temperature trend is enhanced, which reinforces our finding of a cooling trend. The most accepted theory behind a cooling of the middle atmosphere is increased greenhouse gas emissions, which may lead to a change in dynamics. Our results yield a more negative trend in winter compared with summer, which may be explained by radiative and dynamical effects. In summer, a larger heat exchange takes place from atmospheric layers below the cold, polar mesopause. Weakening of gravity wave drag leads to weakening of the mesospheric residual circulation, which counteracts cooling. These effects occur due to increased CO_2 concentrations in the atmosphere, according to model studies.

7 Data availability

Meteor echo fading times from the NTMR radar used to calculate ambipolar diffusion coefficients and neutral temperatures are available upon request from Chris Hall at Tromsø Geophysical Observatory (chris.hall@uit.no). The Aura MLS temperature data are publicly available from the NASA Jet Propulsion Laboratory at http://mls.jpl.nasa.gov/index-eos-mls.php.

Acknowledgements. The research for this article was financially supported by The Research Council of Norway through contract 223252/F50 (CoE). NTMR operation was supported by Research Project KP-9 of National Institute of Polar Research. The authors are grateful to the NASA EOS Aura MLS team for providing free access to the MLS temperature data, and to Frank Mulligan at Maynooth University, Ireland, for providing downloaded data specific for Tromsø. In addition, the authors wish to express their appreciation to the referees of this paper.

Edited by: G. Stiller

References

Akmaev, R. A. and Fomichev, V. I.: Cooling of the mesosphere and lower thermosphere due to doubling of CO_2, Ann. Geophys., 16, 1501–1512, doi:10.1007/s00585-998-1501-z, 1998.

Akmaev, R. A. and Fomichev, V. I.: A model estimate of cooling in the mesosphere and lower thermosphere due to the CO_2 increase over the last 3–4 decades, Geophys. Res. Lett., 27, 2113–2116, doi:10.1029/1999GL011333, 2000.

Ballinger, A. P., Chilson, P. B., Palmer, R. D., and Mitchell, N. J.: On the validity of the ambipolar diffusion assumption in the polar mesopause region, Ann. Geophys., 26, 3439–3443, doi:10.5194/angeo-26-3439-2008, 2008.

Beig, G.: Long-term trends in the temperature of the mesosphere/lower thermosphere region: 1. Anthropogenic influences, J. Geophys. Res., 116, A00H11, doi:10.1029/2011JA016646, 2011.

Bittner, M., Offermann, D., and Graef, H. H.: Mesopause temperature variability above a midlatitude station in Europe, J. Geophys. Res., 105, 2045–2058, doi:10.1029/1999JD900307, 2000.

Cervera, M. A. and Reid, I. M.: Comparison of atmospheric parameters derived from meteor observations with CIRA, Radio Sci., 35, 833–843, doi:10.1029/1999RS002226, 2000.

Chilson, P. B., Czechowsky, P., and Schmidt, G.: A comparison of ambipolar diffusion coefficients in meteor trains using VHF radar and UV lidar, Geophys. Res. Lett., 23, 2745–2748, doi:10.1029/96gl02577, 1996.

Dyrland, M. E., Hall, C. M., Mulligan, F. J., Tsutsumi, M., and Sigernes, F.: Improved estimates for neutral air temperatures at 90 km and 78° N using satellite and meteor radar data, Radio Sci., 45, RS4006, doi:10.1029/2009rs004344, 2010.

Dyrud, L. P., Oppenheim, M. M., and vom Endt, A. F.: The anomalous diffusion of meteor trails, Geophys. Res. Lett., 28, 2775–2778, doi:10.1029/2000GL012749, 2001.

Espy, P. J. and Stegman, J.: Trends and variability of mesospheric temperature at high-latitudes, Phys. Chem. Earth., 27, 543–553, doi:10.1016/S1474-7065(02)00036-0, 2002.

Fomichev, V. I., Jonsson, A. I., de Grandpré, J., Beagley, S. R., McLandress, C., Semeniuk, K., and Shepherd, T. G.: Response of the middle atmosphere to CO_2 doubling: Results from the Canadian Middle Atmosphere Model, J. Climate, 20, 1121–1144, doi:10.1175/JCLI4030.1, 2007.

French, W. J. R. and Burns, G. B.: The influence of large-scale oscillations on long-term trend assessment in hydroxyl temperatures over Davis, Antarctica, J. Atmos. Sol.-Terr. Phys., 66, 493–506, doi:10.1016/j.jastp.2004.01.027, 2004.

French, W. J. R. and Klekociuk, A. R.: Long-term trends in Antarctic winter hydroxyl temperatures, J. Geophys. Res., 116, D00P09, doi:10.1029/2011JD015731, 2011.

French, W. J. R. and Mulligan, F. J.: Stability of temperatures from TIMED/SABER v1.07 (2002–2009) and Aura/MLS v2.2 (2004–2009) compared with OH(6–2) temperatures observed at Davis Station, Antarctica, Atmos. Chem. Phys., 10, 11439–11446, doi:10.5194/acp-10-11439-2010, 2010.

García-Comas, M., Funke, B., Gardini, A., López-Puertas, M., Jurado-Navarro, A., von Clarmann, T., Stiller, G., Kiefer, M., Boone, C. D., Leblanc, T., Marshall, B. T., Schwartz, M. J., and Sheese, P. E.: MIPAS temperature from the stratosphere to the lower thermosphere: Comparison of vM21 with ACE-FTS, MLS, OSIRIS, SABER, SOFIE and lidar measurements, At-

mos. Meas. Tech., 7, 3633–3651, doi:10.5194/amt-7-3633-2014, 2014.

Hall, C. M.: On the influence of neutral turbulence on ambipolar diffusivities deduced from meteor trail expansion, Ann. Geophys., 20, 1857–1862, doi:10.5194/angeo-20-1857-2002, 2002.

Hall, C. M., Aso, T., Tsutsumi, M., Nozawa, S., Manson, A. H., and Meek, C. E.: *Letter to the Editior* Testing the hypothesis of the influence of neutral turbulence on the deduction of ambipolar diffusivities from meteor trail expansion, Ann. Geophys., 23, 1071–1073, doi:10.5194/angeo-23-1071-2005, 2005.

Hall, C. M., Aso, T., Tsutsumi, M., Höffner, J., Sigernes, F., and Holdsworth, D. A.: Neutral air temperatures at 90 km and 70° N and 78° N, J. Geophys. Res., 11, D14105, doi:10.1029/2005JD006794, 2006.

Hall, C. M., Dyrland, M. E., Tsutsumi, M., and Mulligan, F. J.: Temperature trends at 90 km over Svalbard, Norway (78° N 16° E), seen in one decade of meteor radar observations, J. Geophys. Res.-Atmos., 117, D08104, doi:10.1029/2011JD017028, 2012.

Havnes, O. and Sigernes, F.: On the influence of background dust on radar scattering from meteor trails, J. Atmos. Sol.-Terr. Phys., 67, 659–664, doi:10.1016/j.jastp.2004.12.009, 2005.

Hibbins, R. E., Jarvis, M. J., and K Ford, E. A.: Quasi-biennial oscillation influence on long-period planetary waves in the Antarctic upper mesosphere, J. Geophys. Res., 114, D09109, doi:10.1029/2008JD011174, 2009.

Hocking, W. K.: Temperatures using radar-meteor decay times, Geophys. Res. Lett., 26, 3297–3300, doi:10.1029/1999GL003618, 1999.

Hocking, W. K.: Radar meteor decay rate variability and atmospheric consequences, Ann. Geophys., 22, 3805–3814, doi:10.5194/angeo-22-3805-2004, 2004.

Hocking, W. K., Thayaparan, T., and Jones, J.: Meteor decay times and their use in determining a diagnostic mesospheric temperature-pressure parameter: methodology and one year of data, Geophys. Res. Lett., 24, 2977–2980, doi:10.1029/97gl03048, 1997.

Hoffmann, P., Becker, E., Singer, W., and Placke, M.: Seasonal variation of mesospheric waves at northern middle and high latitudes, J. Atmos. Sol.-Terr. Phys., 72, 1068–1079, doi:10.1016/j.jastp.2010.07.002, 2010.

Hoffmann, P., Rapp, M., Singer, W., and Keuer, D.: Trends of mesospheric gravity waves at northern middle latitudes during summer, J. Geophys. Res., 116, D00P08, doi:10.1029/2011JD015717, 2011.

Holdsworth, D. A., Morris, R. J., Murphy, D. J., Reid, I. M., Burns, G. B., and French, W. J. R.: Antarctic mesospheric temperature estimation using the Davis mesosphere-stratosphere-troposphere radar, J. Geophys. Res.-Atmos., 111, D05108, doi:10.1029/2005jd006589, 2006.

Holmen, S. E., Dyrland, M. E., and Sigernes, F.: Mesospheric temperatures derived from three decades of hydroxyl airglow measurements from Longyearbyen, Svalbard (78° N), Acta Geophys., 62, 302–315, doi:10.2478/s11600-013-0159-4, 2013.

Holmen, S. E., Dyrland, M. E., and Sigernes, F.: Long-term trends and the effect of solar cycle variations on mesospheric winter temperatures over Longyearbyen, Svalbard (78° N), J. Geophys. Res.-Atmos., 119, 6596–6608, doi:10.1002/2013jd021195, 2014.

Horne, J. H. and Baliunas, S. J.: A prescription for period analysis for unevenly sampled time series, Astrophys. J., 302, 757–763, doi:10.1086/164037, 1986.

Jacobi, C.: Long-term trends and decadal variability of upper mesosphere/lower thermosphere gravity waves at midlatitudes, J. Atmos. Sol.-Terr. Phys., 118, 90–95, doi:10.1016/j.jastp.2013.05.009, 2014.

Kovalev, D. V., Smirnov, A. P., and Dimant, Y. S.: Modeling of the Farley-Buneman instability in the E-region ionosphere: a new hybrid approach, Ann. Geophys., 26, 2853–2870, doi:10.5194/angeo-26-2853-2008, 2008.

Laštovicka, J., Akmaev, R. A., Beig, G., Bremer, J., Emmert, J. T., Jacobi, C., Jarvis, M. J., Nedoluha, G., Portnyagin, Yu. I., and Ulich, T.: Emerging pattern of global change in the upper atmosphere and ionosphere, Ann. Geophys., 26, 1255–1268, doi:10.5194/angeo-26-1255-2008, 2008.

Laštovička, J., Solomon, S. C., and Qian, L.: Trends in the neutral and ionized upper atmosphere, Space Sci. Rev., 168, 113–145, doi:10.1007/s11214-011-9799-3, 2012.

Liu, H.-L., Roble, R. G., Taylor, M. J., Pendleton Jr., W. R.: Mesospheric planetary waves at northern hemisphere fall equinox, Geophys. Res. Lett., 28, 1903–1906, doi:10.1029/2000GL012689, 2001.

Lübken, F.-J.: Thermal structure of the Arctic summer mesosphere, J. Geophys. Res.-Atmos., 104, 9135–9149, doi:10.1029/1999JD900076, 1999.

Lübken, F.-J. and von Zahn, U.: Thermal structure of the mesopause region at polar latitudes, J. Geophys. Res.-Atmos., 96, 20841–20857, doi:10.1029/91JD02018, 1991.

Lübken, F.-J., Berger, U., and Baumgarten, G.: Temperature trends in the midlatitude summer mesopause, J. Geophys. Res.-Atmos., 118, 13347–13360, doi:10.1002/2013JD020576, 2013.

Manabe, S. and Wetherald, R. T.: The effects of doubling the CO_2 concentration on the climate of a general circulation model, J. Atmos. Sci., 32, 3–15, doi:10.1175/1520-0469(1975)032<0003:TEODTC>2.0.CO;2, 1975.

Manson, A. H., Meek, C. E., Stegman, J., Espy, P. J., Roble, R. G., Hall, C. M., Hoffmann, P., and Jacobi, Ch.: Springtime transitions in mesopause airglow and dynamics: photometer and MF radar observations in the Scandinavian and Canadian sectors, J. Atmos. Sol.-Terr. Phys., 64, 1131–1146, doi:10.1016/S1364-6826(02)00064-0, 2002.

McKinley, D. W. R.: Meteor Science and Engineering, McGraw-Hill, New York, 1961.

NASA: Annual Meteorological Statistics, National Aeronautics Space Administration, available at: http://acdb-ext.gsfc.nasa.gov/Data_services/met/ann_data.html, last access: April 2016.

NASA Jet Propulsion Laboratory: EOS Microwave Limb Sounder, available at: http://mls.jpl.nasa.gov/index-eos-mls.php, last access: January 2015.

Niciejewski, R. J. and Killeen, T. L.: Annual and semi-annual temperature oscillations in the upper mesosphere, Geophys. Res. Lett., 22, 3243–3246, doi:10.1029/95GL02411, 1995.

Offermann, D., Hoffmann, P., Knieling, P., Koppmann, R., Oberheide, J., and Steinbrecht, W.: Long-term trends and solar cycle variations of mesospheric temperatures and dynamics, J. Geophys. Res., 115, D18127, doi:10.1029/2009JD013363, 2010.

Ogawa, Y., Motoba, T., Buchert, S. C., Häggström, I., and Nozawa, S.: Upper atmosphere cooling over the past 33 years, Geophys. Res. Lett., 41, 5629–5635, doi:10.1002/2014GL060591, 2014.

Oliver, W. L., Zhang, S.-R., and Goncharenko, L. P.: Is thermospheric global cooling caused by gravity waves?, J. Geophys. Res., 118, 3898–3908, doi:10.1002/jgra.50370, 2013.

Press, W. H. and Rybicki, G. B.: Fast algorithm for spectral analysis of unevenly sampled data, Astrophys. J. Part 1, 338, 277–280, doi:10.1086/167197, 1989.

Rees, D., Rishbeth, H., and Kaiser, T. R.: Winds and temperatures in the auroral zone and their relations to geomagnetic activity, Philos. T. R. Soc. A, 271, 563–575, doi:10.1098/rsta.1972.0024, 1972.

Roble, R. G. and Dickinson, R. E.: How will changes in carbon dioxide and methane modify the mean structure of the mesosphere and thermosphere?, Geophys. Res. Lett., 16, 1441–1444, doi:10.1029/GL016i012p01441, 1989.

Salby, M. L.: Rossby normal modes in nonuniform background configurations. Part I: Simple fields, J. Atmos. Sci., 38, 1803–1826, doi:10.1175/1520-0469(1981)038<1803:RNMINB>2.0.CO;2, 1981a.

Salby, M. L.: Rossby normal modes in nonuniform background configurations. Part II: Equinox and solstice conditions, J. Atmos. Sci., 38, 1827–1840, doi:10.1175/1520-0469(1981)038<1827:RNMINB>2.0.CO;2, 1981b.

Scargle, J. D.: Studies in astronomical time series analysis. II. Statistical aspects of spectral analysis of unevenly spaced data, Astrophys. J., 263, 835–853, doi:10.1086/160554, 1982.

Schmidt, H., Brasseur, G. P., Charron, M., Manzini, E., Giorgetta, M. A., and Diehl, T.: The HAMMONIA Chemistry Climate Model: Sensitivity of the mesopause region to the 11-year solar cycle and CO_2 doubling, J. Climate, 19, 3903–3931, doi:10.1175/JCLI3829.1, 2006.

Shepherd, M. G., Espy, P. J., She, C. Y., Hocking, W., Keckhut, P., Gavrilyeva, G., Shepherd, G. G., and Naujokat, B.: Springtime transition in upper mesospheric temperature in the northern hemisphere, J. Atmos. Sol.-Terr. Phys., 64, 1183–1199, doi:10.1016/S1364-6826(02)00068-8, 2002.

Shepherd, M. G., Rochon, Y. J., Offermann, D., Donner, M., and Espy, P. J.: Longitudinal variability of mesospheric temperatures during equinox at middle and high latitudes, J. Atmos. Sol.-Terr. Phys., 66, 463–479, doi:10.1016/j.jastp.2004.01.036, 2004.

Stray, N. H., de Wit, R. J., Espy, P. J., and Hibbins, R. E.: Observational evidence for temporary planetary wave forcing of the MLT during fall equinox, Geophys. Res. Lett., 41, 6281–6288, doi:10.1002/2014GL061119, 2014.

Taylor, M. J., Pendleton Jr., W. R., Liu, H.-L., She, C. Y., Gardner, L. C., Roble, R. G., and Vasoli, V.: Large amplitude pertubations in mesospheric OH Meinel and 87-km Na lidar temperatures around the autumnal equinox, Geophys. Res. Lett., 28, 1899–1902, doi:10.1029/2000GL012682, 2001.

Tiao, G. C., Reinsel, G. C., Xu, D., Pedrick, J. H., Zhu, X., Miller, A. J., DeLuisi, J. J., Mateer, C. L., and Wuebbles, D. J.: Effects of autocorrelation and temporal sampling schemes on estimates of trend and spatial correlation, J. Geophys. Res.-Atmos., 95, 20507–20517, doi:10.1029/JD095iD12p20507, 1990.

von Savigny, C.: Variability of OH(3-1) emission altitude from 2003 to 2011: Long-term stability and universality of the emission rate-altitude relationship, J. Atmos. Sol.-Terr. Phys., 127, 120–128, doi:10.1016/j.jastp.2015.02.001, 2015.

Walterscheid, R. L.: Dynamical cooling induced by dissipating internal gravity waves, Geophys. Res. Lett., 8, 1235–1238, doi:10.1029/GL008i012p01235, 1981.

Weatherhead, E. C., Reinsel, G. C., Tiao, G. C., Meng, X.-L., Choi, D., Cheang, W.-K., Keller, T., DeLuisi, J., Wuebbles, D. J., Kerr, J. B., Miller, A. J., Oltmans, S. J., and Frederick, J. E.: Factors affecting the detection of trends: Statistical considerations and applications to environmental data, J. Geophys. Res., 103, 17149–17161, doi:10.1029/98JD00995, 1998.

Winick, J. R., Wintersteiner, P. P., Picard, R. H., Esplin, D., Mlynczak, M. G., Russell III, J. M., and Gordley, L. L.: OH layer characteristics during unusual boreal winters of 2004 and 2006, J. Geophys. Res., 114, A02303, doi:10.1029/2008JA013688, 2009.

Yigit, E. and Medvedev, A. S.: Heating and cooling of the thermosphere by internal gravity waves, Geophys. Res. Lett., 36, L14807, doi:10.1029/2009GL038507, 2009.